BROADBAND AND RECONFIGURABLE FILTERING ANTENNAS FOR NEXT GENERATION MOBILE WIRELESS COMMUNICATIONS SYSTEMS

by

Joshua Wayne Shehan

A dissertation submitted to the faculty of
The University of North Carolina at Charlotte
in partial fulfillment of the requirements
for the degree of Doctor of Philosophy in
Electrical Engineering

Charlotte

2018

Approved by:

Dr. Ryan S. Adams

Dr. Thomas P. Weldon

Dr. Yogendra Kakad

Dr. Taghi Mostafavi

ABSTRACT

JOSHUA WAYNE SHEHAN. Broadband and Reconfigurable Filtering Antennas for Next Generation Mobile Wireless Communications Systems. (Under the direction of DR. RYAN S. ADAMS)

Mobile wireless communications systems, particularly at the base station level, are ever evolving to provide more data with better coverage resulting in continuously evolving antenna technology. From first generation (1G) mobile networks deployed using simple vertically polarized omnidirectional antennas to future fifth generation (5G) networks utilizing advanced dual polarized multibeam antenna solutions, mobile base station antennas have seen rapid development in the last 40 years. Today's fourth generation (4G) base station antenna systems commonly use multiband, dual polarized antennas where optimal performance is desired in difficult operating environments. Common operating bands for current 4G base station antennas are 698-960 MHz and 1695-2690 MHz where antenna elements covering both bands are usually integrated into a single package. This can make it difficult to achieve desired pattern performance and impedance matching. Furthermore, 600 MHz, 3.5 GHz, and 5 GHz spectrum has been released for mobile base station antennas creating wider bandwidths and more bands in the same radome or collocated under different radomes.

Future 5G antenna systems will operate to millimeter wave frequencies (>30 GHz) and deliver data rates much higher than those of today's mobile networks. Due to the small antenna size for millimeter wave frequencies, many antenna elements can be integrated into a relatively small package enabling high gain, multibeam solutions which will be required to deliver the data rates promised by 5G. Millimeter wave technology is new to the base station antenna industry, and a significant amount of research and development is underway to understand the possibilities and difficulties of millimeter wave use in the mobile wireless realm.

Antennas for mobile wireless applications will be forced to integrate 4G and 5G technology into the same package for some installations. As a result, the base station may be forced to cover frequencies as low as 600 MHz while simultaneously covering frequencies as high as 30 GHz or more. Network densification will also be important in the development of 4G and 5G base station antennas. This involves placing many antennas in areas of high data traffic creating a need for low profile antennas with precise pattern control to minimize sector overlap. Unfortunately, the addition of new spectrum coupled with network densification creates a need for filters to manage interference.

Filtering is also an essential part of wireless systems to block unwanted signals that can cause system degradation. Filters can be bulky, expensive, and difficult to implement. Integrating the filter directly into the antenna has tremendous advantages in terms of size, cost, and the ability to control the filter impact on the system. The addition of new spectrum for advanced 4G and 5G systems creates a need for filtering antennas to reject unwanted signals that can degrade the overall system.

This dissertation presents the design and analysis of filtering antenna systems to meet the demands of 4G and 5G mobile wireless applications. New and innovative antennas incorporating broadband and narrowband filters are presented to manage interference for tomorrow's mobile wireless systems.

ACKNOWLEDGEMENTS

First, I would like to praise God for this experience. This has been an incredibly difficult journey, but through the good times and the bad, I have grown as an engineer, as a researcher, and as a person.

I cannot express enough gratitude to the individuals and organizations who have supported me throughout this journey. Having spent time in industry at Harris Corporation and at Amphenol Antenna Solutions, I must acknowledge the support of both organizations indirectly and directly. I wish to thank Amphenol Antenna Solutions for supporting a large portion of the work presented in this dissertation, and I would like to acknowledge the support and contributions of my colleagues at Amphenol. A special thanks to Carl Gersch for assistance in 3D printing and a willingness to always provide an extra hand to collect test data.

I would also like to thank my former colleagues at Harris Corporation for their technical mentorship and guidance in the antenna field. Specifically, I would like to thank Dr. Sean Ortiz of Harris Corporation for valuable technical discussions. Sean made a suggestion early in my PhD work that helped to steer the course for the remainder of my studies.

I wish to thank my advisor, Dr. Ryan Adams, for his guidance over the years, both technical and non-technical. His mentorship will have a lasting impact on my career. Thanks to my committee members, Dr. Thomas Weldon, Dr. Yogendra Kakad, and Dr. Taghi Mostafavi for your support. Also a special thanks to Dr. Weldon for guidance and funding support very early in my graduate studies.

I wish to thank my family for their love and support along the way, but I specifically want to thank my wife, Brittany. This degree would not have been possible without her patience, love, and encouragement. I would also like to recognize the love and support of my two wonderful children, Levi and Sadie.

TABLE OF CONTENTS

LIST OF FIGURES

LIST OF TABLES

CHAPTER 1: INTRODUCTION

1.1 Background and Motivation

Mobile wireless systems have revolutionized personal communications over the past few decades. From the first analog systems to today's 4G LTE (Long Term Evolution) networks, the mobile wireless market has seen rapid development enabled by advances in key technology areas such as signal processing and battery technology. However, at the heart of the system, the base station antenna (BSA), is a key component that provides the link between the network and the user.

Although there were commercial mobile networks and trials deployed throughout the 1970s, first generation mobile networks (1G) were officially deployed in the late 1970s and early 1980s. These networks were analog, voice only systems that primarily used low gain omnidirectional antennas to blanket a coverage area. These networks were low capacity, but the antennas could be placed approximately 10λ apart for spatial diversity for capacity enhancement. Second generation (2G) was deployed in the 1990s and introduced digital technology enabling text messaging and low speed data up to approximately 300 kbps. The base station antenna systems for 2G networks also included directional antenna arrays with control of the vertical and horizontal half power beamwidths. This enabled cell sectorization for enhanced network capacity. Third generation (3G) mobile networks were deployed in the early 2000s and enabled much faster data speeds with a maximum of 2 Mbps, though higher data rates are available for today's 3G systems. Third generation networks saw the introduction of dual polarized and multiband antennas. Dual polarization enabled another layer of diversity (polarization diversity) over spatial diversity for further capacity enhancements. Multiband antennas also enabled the antennas to be combined into a single radome reducing space needed on the tower. Remote electrical tilt was also introduced in the late 1990s/early 2000s enabling the radiation pattern to be controlled remotely. Commercial multiple-input multiple-output (MIMO) was also introduced as a practical approach for increasing system capacity [1–5].

Fourth generation (4G) is considered current generation where deployments began in the late 2000s and early 2010s. Fourth generation requirements set by the International Telecommunications Union (ITU) enable a theoretical maximum data rate of 1.5 Gbps. Furthermore, the need to deliver higher capacity and better coverage for ubiquitous wireless connectivity drives the need for small cell and distributed antenna system (DAS) development [6, 7]. In small cell and DAS deployments, antennas are installed among the user population and designed to be as inconspicuous as possible. In many cases, optimal antenna performance is desired in sub-optimal operating environments creating unique challenges from a design standpoint.

Fifth generation (5G) research and development is well underway as standards and applications are currently being developed. Fifth generation promises to deliver multi-gigabit per second data rates with improved coverage over today's best 4G networks. Researchers in academia and industry are also investigating frequencies from 3 GHz to millimeter wave ($>$ 30 GHz) for various applications creating many exciting opportunities for the base station antenna engineer [3, 8].

As mobile networks provide more services with each new generation, the requirements on the base station antenna become increasingly more complex. Some of the factors taken into account in base station antenna design are pattern shape, bandwidth, isolation between antenna ports, and visual appeal. The base station antennas of tomorrow must deliver optimal performance even in sub-optimal environments and must be inconspicuous to the average user. Furthermore, the addition of new spectrum and the push toward densification put antennas of various bands in close proximity. In some cases, antennas covering multiple bands may be housed in a single radome, but in other cases separate radomes may house antennas of disparate frequency bands as illustrated in Fig. 1.1. Unfortunately, antennas may couple and cause interference problems even when housed in separate radomes as shown in Fig. 1.2. In these instances, interference may occur, and filtering may be necessary to maintain optimal system performance. Unintended spurious signals may also become more problematic with densification and the addition of new spectrum, and out-of-band suppression filters may be required to limit or block spurious radiation.

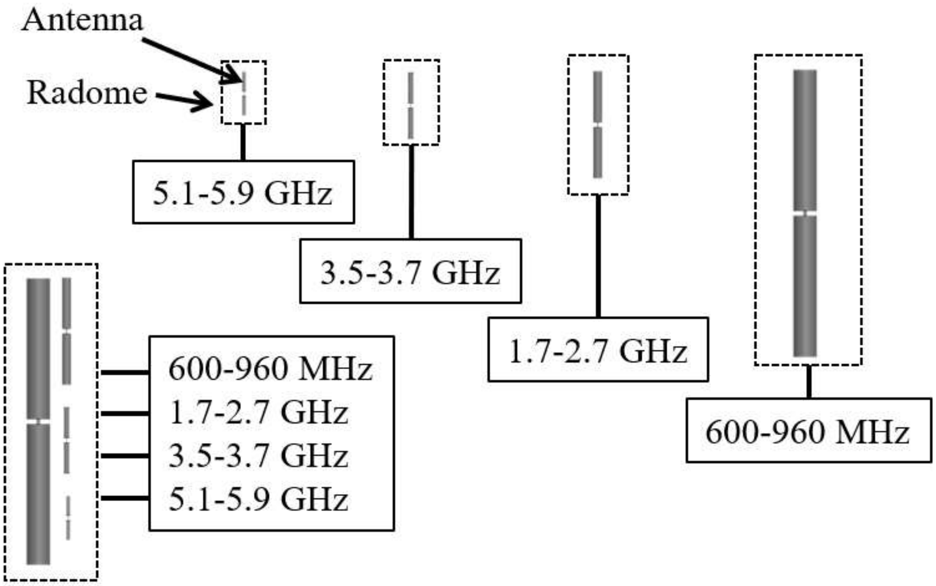

Figure 1.1: Illustration of ideal antenna environments where all antennas operate in their own radome away from antennas from other bands and typical realized environment where antennas of multiple bands are incorporated under the same radome or in close proximity.

Another challenge for base station antenna developers is passive intermodulation (PIM) [9–12]. PIM occurs when two or more frequencies mix in a passive system and generate additional frequencies. This is caused by non-linearities in the system that generate unwanted frequencies determined by

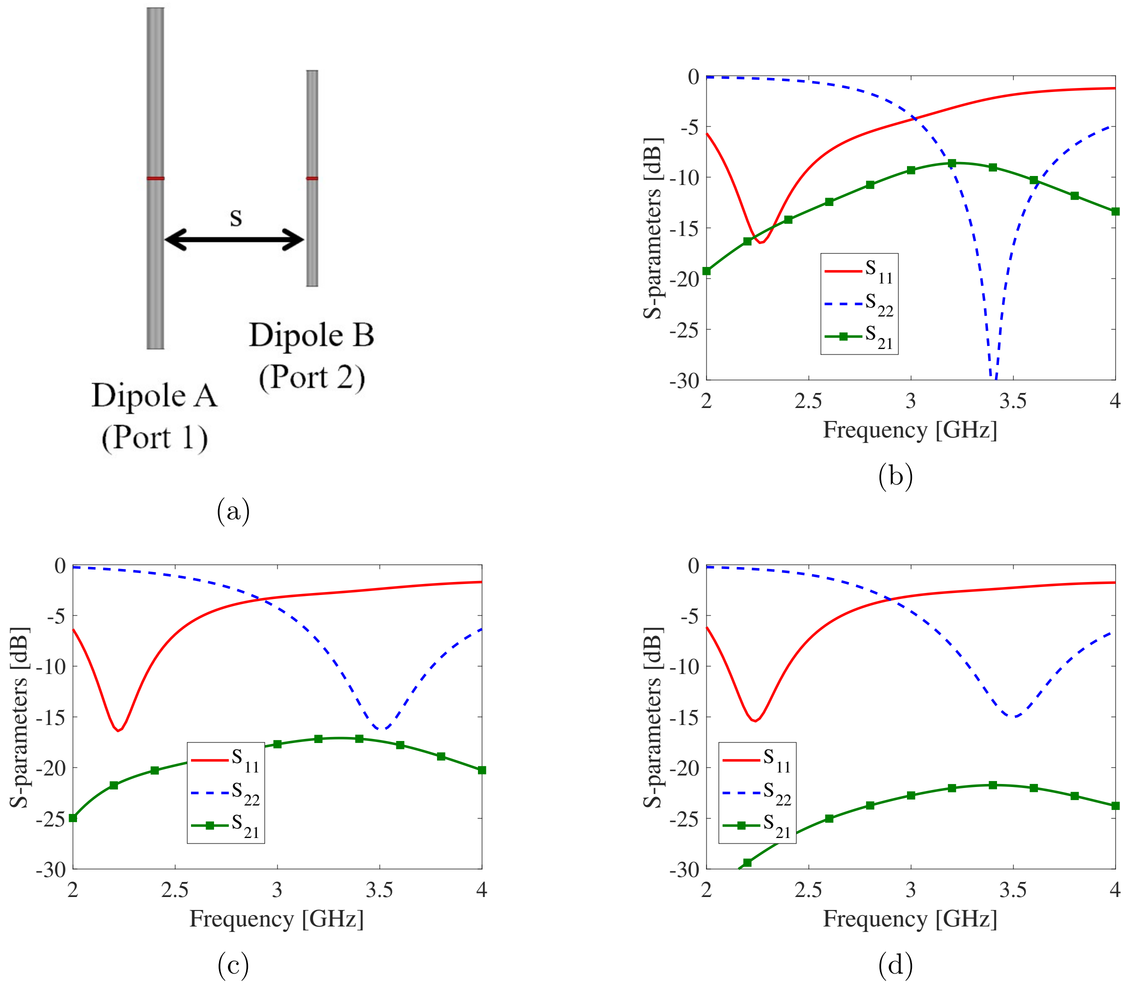

(a)

(b)

(c)

(d)

Figure 1.2: Return loss (S_{11}, S_{22}) and isolation (S_{21}) between a 2.25 GHz dipole and a 3.5 GHz dipole (a) at separation distances, s of 10 mm (b), 50 mm (c), and 100 mm (d).

$$f_{PIM} = \pm m f_1 \pm n f_2 \quad m = 1, 2, 3, \ldots \quad n = 1, 2, 3, \ldots \tag{1.1}$$

where f_{PIM} is the intermodulation frequency, and the order of the intermodulation product is determined by $m+n$. For example, third order ($m+n = 3$) intermodulation frequencies for two signals f_1=2600 MHz and f_2=3400 MHz are generated at 1800 MHz, 4200 MHz, 8600 MHz, 9400 MHz. If the primary system is a mobile base station operating in the 1695-2690 MHz range and picking up interference at 3400 MHz, the intermodulation product at 1800 MHz could be problematic and degrade system performance. However, if the 3400 MHz signal can be filtered out of the system, the 1800 MHz intermodulation frequency would not be present.

Depending on the original intended frequencies, the frequencies due to intermodulation may fall within the base station antenna's receive band which can lead to degraded system performance such as reduced data rates and dropped calls. PIM is generally more problematic at higher power levels, but it can lead to problems with low power systems as well. One way to potentially mitigate PIM is to eliminate the frequencies that are mixing to generate the modulated signals, and if the filtering can be accomplished at the antenna, the unwanted signals will interact with less of the system theoretically reducing the chance of PIM issues.

Clearly, filters are a necessity for base station antenna systems , but the addition of filters adds cost and complexity to the system. Filters generally are not cheap, they can be bulky, and they add components in line with the antenna as shown in the system diagram of Fig. 1.3. Filtering may be accomplished at the radio, but in some cases, it may be necessary or beneficial to filter closer to the radiating element. Therefore, filtering antennas are highly desirable. Integrating filters directly into the antennas provides a compact solution that reduces system cost and complexity as illustrated in Fig. 1.4. The increasingly demanding requirements for base station antennas, the addition of new frequency bands, and the push for network densification makes filtering antennas a unique field of extraordinary challenges with many opportunities for creativity and innovation.

1.2 Objectives and Outline

The objective of this dissertation is to introduce base station antenna solutions to meet the demands of today's advanced and tomorrow's wireless networks. Multiband antennas are introduced covering multiple mobile services and generations. This dissertation also presents antenna solutions that exploit the filtering characteristics of metamaterial structures for antennas with integrated filtering solutions. By integrat-

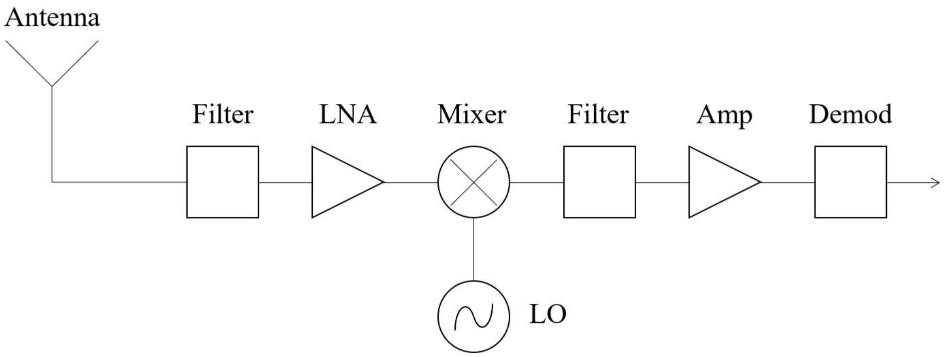

Figure 1.3: Typical RF receiver.

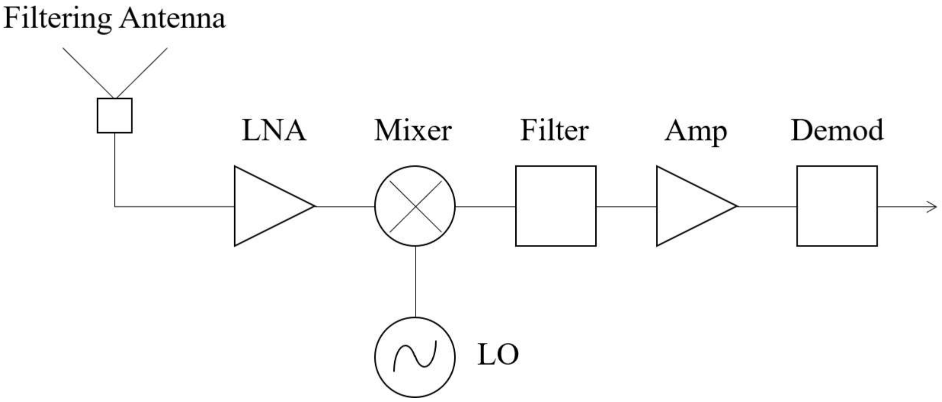

Figure 1.4: Condensed RF receiver.

ing filtering structures into antennas, compact solutions are achieved that eliminate interference issues that can degrade the performance of multiband systems. Lens solutions for next generation base station antennas are also addressed.

This dissertation presents the design and analysis of filtering antenna systems to meet the demands of 4G and 5G mobile base stations. Chapter 2 provides an overview of current generation and next generation base station antenna technology. The general requirements and design approach for current generation base station antennas are discussed. The direction and research trends for next generation base station antenna technology are also discussed. The need for advanced antenna solutions that incorporate filtering is demonstrated.

Chapter 3 provides background on the topics covered in this dissertation. The topics include multiband base station antennas, metamaterials for antenna applications, and filtering antennas utilizing metamaterial structures. The technological advancements introduced in this dissertation broadly fit into these categories.

Chapter 4 presents a horn antenna with a reconfigurable notch filter for base station applications. The filter is composed of coupled metamaterial structures designed by the Lagrangian formulation for metamaterials. In this work, the Lagrangian formulation is applied for the first time as a method for microwave filter design. It is shown that this approach is an effective way to design coupled resonator filters based on metamaterial inclusions in waveguide structures.

Chapter 5 presents a wide beam antenna with integrated filtering. The antenna operates from 1.7-2.7 GHz corresponding to traditional 4G frequencies, and provides broadband filtering from approximately 3-6 GHz. Frequency bands in the range of 3-6 GHz have been realeased for 4G LTE and are being investigated for 5G leading to the development and deployment of antennas covering these bands either in close proximity to or in the same radome/enclosure as antennas covering the more traditional 1.7-2.7 GHz 2G/3G/4G frequencies. In some cases, it may be practical to utilize a single broadband antenna to cover frequencies from 1.7-6 GHz, but in other cases, the need to control patterns makes this impossible. Additionally, spurious signals generated by the radio may radiate and cause interference to nearby antennas and systems, but the filtering approach presented herein provides a mitigation procedure to keep spurious signals from radiating unintentionally.

Chapter 6 presents a dual band 4G/5G antenna where three dual polarized linear arrays of 5G antennas are integrated into the structure of a vertically polarized 4G antenna. The 5G antenna in this chapter operates from 27.5-28.35 GHz, and the 4G antenna operates from 1.7-2.7 GHz. This antenna design addresses the transition from 4G to 5G where a single node can provide coverage for both mobile generations. The 4G antenna is a sleeve monopole antenna similar to the antenna presented in Chapter 5, and the 5G antenna is a series fed patch array incorporated into the sleeve of the 4G antenna. Integration of the antennas in the manner presented in this chapter enables the addition 5G capability essentially without adding volume to a 4G antenna. The sleeve monopole also includes a filter to eliminate any unwated radiation in the 5G frequency band. Path loss is comparitively very high in the 5G band for this antenna, and the system needs to be as sensitive as possible to ensure optimal network performance. Any unintended radiation from the 4G antenna could degrade 5G system performance. The patch array also includes a band pass filter to enhance selectivity of the antenna and ease filtering requirements in the radio or RF front end.

Chapter 7 discusses the conclusion of this dissertation and future work. The dissertation introduces novel filtering antennas to meet the demands of today's and tomorrow's mobile networks, but this dissertation also presents a solid foundation for the exploration of new filtering antenna approaches and direct extensions of the work presented herein to advance the field of filtering antennas.

CHAPTER 2: CURRENT AND FUTURE BASE STATION ANTENNA TECHNOLOGY

2.1 Introduction

This section provides a brief overview of current and future base station antenna technology. In terms of mobile generations, current state of the art is considered fourth generation (4G) where today's base station antennas are generally multiband covering frequencies in the range of $\sim$698-960 MHz for low band and $\sim$1695-2690 MHz for high band. In this dissertation, these bands will be referred to as current generation low band and current generation high band. However, other frequencies may be included for applications such as Wi-Fi and WiMAX. Antenna arrays are common to offer enhanced control over the radiation patterns, but they are not required in every system. Due to spectrum saturation and the need for ever increasing amounts of data supplied by wireless carriers, fifth generation (5G) systems are actively being investigated and developed. These systems are investigating the use of new technologies, such as massive MIMO, and the use of much higher frequencies up to and including millimeter wave. This chapter provides a brief introduction to current generation and future generation base station antenna technology.

2.2 Current Generation Base Station Antennas

In this dissertation, current generation refers to base station antennas designed primarily to meet the requirements of today's fourth generation (4G) mobile network, although, the base station antennas discussed here are generally backward compatible and also work with previous generation mobile technology. Current generation base station antennas typically cover mobile frequencies from approximately 698-960

MHz to 1695-2690 MHz where it is common for antennas covering both bands to be integrated into a single package [13]. These frequencies correspond to various wireless services such as AWS, PCS, GSM, UMTS, LTE, HSPA, Wi-Fi and WiMAX. In some cases, a single broadband antenna can be used to cover both operating bands and cover multiple wireless services. However, separate antennas are used to cover the individual bands in other cases, especially for applications where antenna arrays are used to provide some type of beamforming. Note that current generation base station antennas may provide coverage for bands outside of the common 698-960 MHz and 1695-2690 MHz such as Wi-Fi and LTE bands in the 3-6 GHz range.

One of the challenges with the addition of new spectrum is interference management. With many antennas of various frequency bands operating in close proximity and the need to maintain receiver sensitivity for optimal network performance, filtering antennas will become a necessity. As previously stated, one of the challenges with higher frequencies is the path loss associated that is directly proportional to frequency, and a noisy transmitter that produces spurious signals can lead to interference and other network problems that degrade system performance. Furthermore, mobile network providers may operate in bands that are near other services or unlicensed where interference can be problematic for the overall system. Filtering antennas will be a key component of next generation mobile base stations.

The use of linear arrays are a common approach where multiple radiating elements are arranged in the elevation plane to provide narrow elevation beamwidths. Furthermore, the relative amplitude and phase between the elements of the array can also be controlled to steer the beam, apply a sidelobe taper, or place nulls in the radiation pattern [14]. Historically, base station antennas were physically tilted on a tower to control the main beam location, but current generation antennas typically include means for electronically steering the main beam. This can be accomplished through the use of beamforming networks or mechanically steered phase shifters controlled with remote electrical tilt (RET) technology [1, 2].

Current generation base station antennas commonly incorporate diversity gain through the use of multiple antennas either separated by space or polarization [15–18]. Spatial diversity is achieved by separating two copolarized antennas by some distance, usually 10λ where λ is the free space wavelength of the carrier frequency. Polarization diversity is achieved through the use of two orthogonally polarized antennas where the antennas are typically linearly polarized with slant $\pm 45^\circ$ polarizations or vertical/horizontal (V/H) polarizations. Diversity in mobile communications basically exploits multipath propagation between the antennas separated by space or polarization to enhance system performance. Utilizing one or both of these diversity techniques, multiple-input multiple-output (MIMO) solutions have emerged as technology has enabled mobile phones to become smaller and incorporate multiple antennas [19–22]. MIMO enables significant capacity gains and has become an important aspect of wireless networks. Figure 2.1 shows an illustrative example of a dual slant ($\pm 45^\circ$) polarized base station antenna array that would be practical for today's base stations, and Figure 2.2 shows an illustrative example of spatially separated co-polarized antennas that may be used for diversity gain or MIMO.

Although 4G is being deployed all over the world, the need for more data forces the continued development and innovation for 4G solutions. From investigation of new frequency bands to unique ways of delivering optimal capacity in dense user environments, the requirements for 4G base station antennas continue to evolve. Depending on the geographical coverage area required by the base station, the antenna generally falls into one of two broad categories: directional or omnidirectional.

2.2.1 Directional Antennas

Directional base station antennas similar to that shown in Fig. 2.3 are designed to provide sectorial coverage with a specific beamwidth in azimuth and elevation [15–18, 23–25]. These antennas are common for traditional cell, sometimes referred

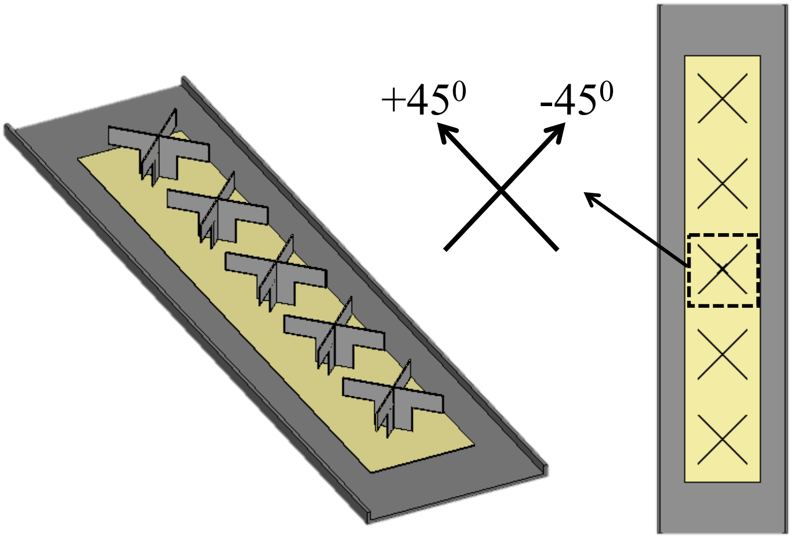

Figure 2.1: Dual slant (±45°) polarized base station antenna array.

to as macrocell, approaches where the antennas are placed on towers in the center of the cell. The size and shape of each cell is determined by the gain and half power beamwidth (HPBW) of the base station antennas covering the cell. Small cell and DAS coverage areas are relatively small compared to macrocell approaches [7]. Macrocells typically cover a radius of 0.5-5 km where small cells generally cover an area with a radius of 2 km or less. DAS coverage areas can be quite large depending on the number of antennas distributed, but these solutions are more appropriate for small area, high capacity areas like stadiums and office buildings. As a result of the intended coverage areas, small cell and DAS antennas generally exhibit lower gain than macrocell antennas. Three and six sector approaches are common for today's mobile base stations covering macrocells and some small cells. The three sector solution divides the cell into three sectors where the base station antenna covering each cell sector typically exhibits an azimuth HPBW of 65°, 85°, or 90°. The six sector solution divides the cell into six sectors where the base staiton antenna covering each cell sector typically exhibits an azimuth HPBW of 33° or 45°.

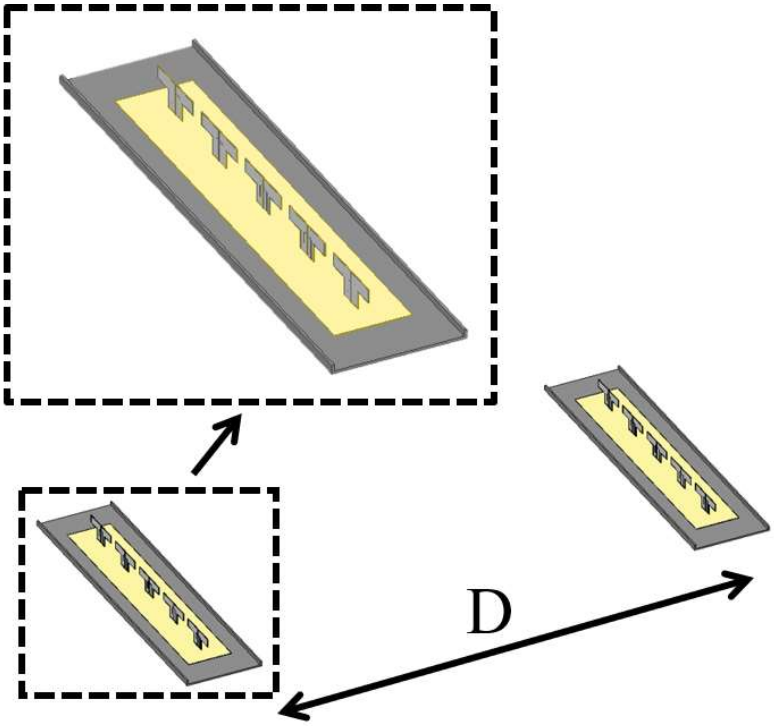

Figure 2.2: Two linearly polarized antennas separated by a distance D for spatial diversity.

2.2.2 Omnidirectional Antennas

Omnidirectional base station antennas are designed to provide an omnidirectional radiation pattern in one plane (typically azimuth) [26–34]. The growing need for network coverage in highly populated environments has driven the need for network densification and small cell deployments [6, 7]. In these deployments, omnidirectional or pseudo-omnidirectional antenna approaches are a practical solution as the lower gain of the antenna reduces the effective cell size so many antennas can be deployed without significant cell overlap. Omnidirectional antennas offer less capacity than a sectorized base station approach, but this is appropriate for densification and DAS solutions where many antennas are deployed with a limited cell size to cover places

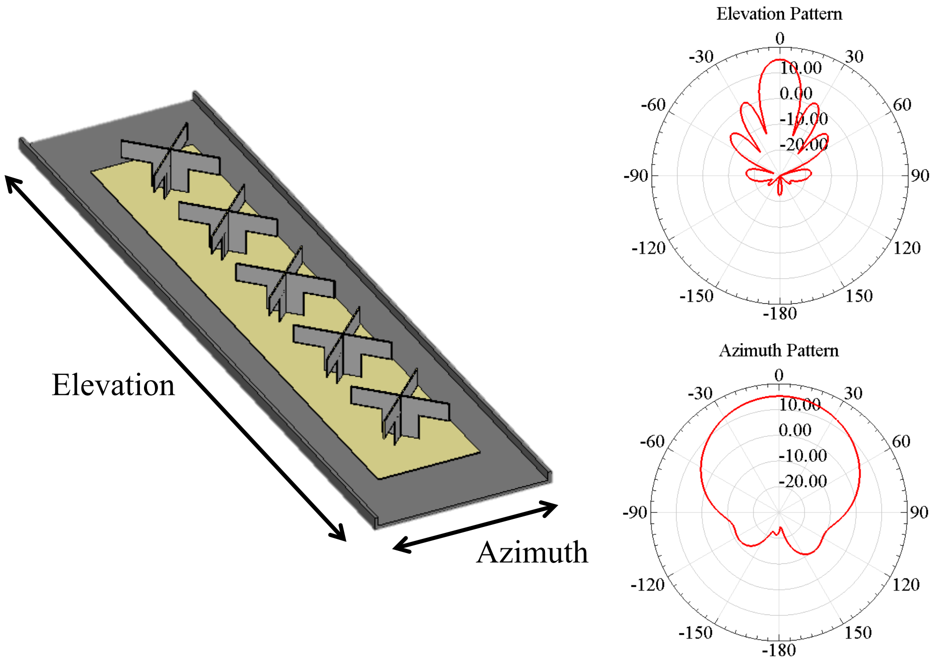

Figure 2.3: Dual slant (±45°) polarized directional base station antenna array with 65° azimuth beamwidth

such as office buildings or stadiums. The number of cells deployed is used to overcome the capacity limitations of the omnidirectional antennas used in each cell. Note that omnidirectional antennas can also be deployed with dual polarization to provide diversity as in the directional approach. An example of a linearly polarized 5-element array of biconical dipole antennas is shown in Fig. 2.4 for demonstration.

2.3 Next Generation Base Station Antennas

Next generation refers to base station antenna technology designed to work with future fifth generation (5G) mobile networks. Fifth generation wireless networks promise to deliver multi-gigabit per second data rates with improved coverage over current generation solutions. There are also numerous applications considered for 5G outside of mobile broadband such as mobile health systems, infrastructure monitoring, and self-driving cars, all of which may be broadly classified as internet of things applications [7,8,35,36]. As a result of tremendous potential and 5G system requirements, large amounts of spectrum are under consideration from less than 1 GHz to

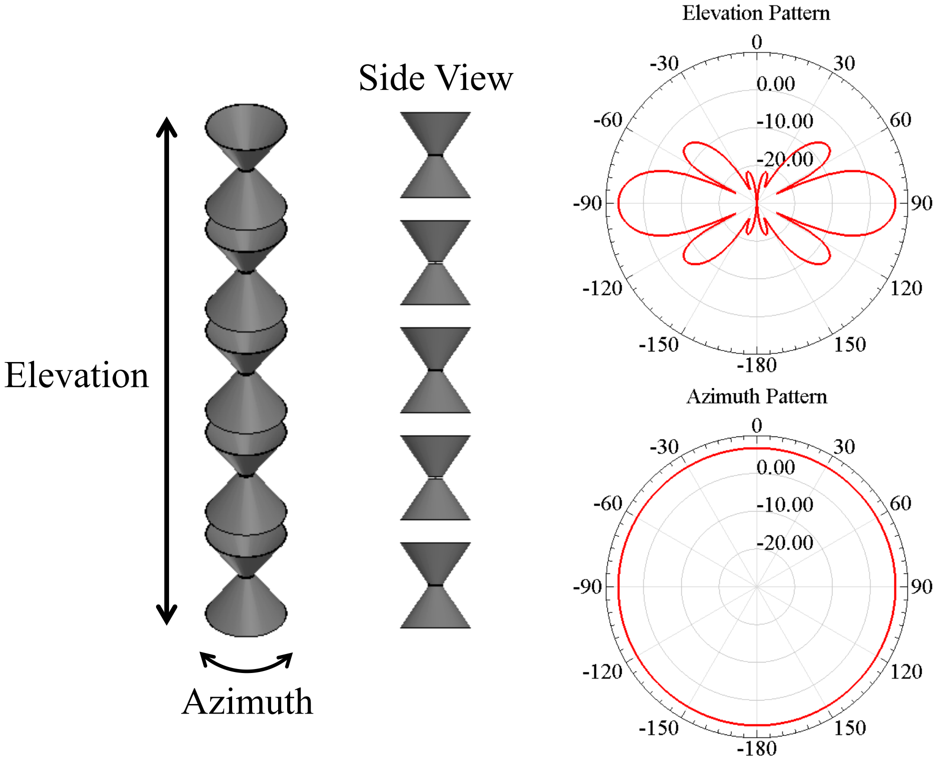

Figure 2.4: Linearly polarized omnidirectional base station antenna array

millimeter wave frequencies in addition to the bands already used for current generation antenna systems. Particularly heavy focus is being placed on systems operating from 3 GHz to millimeter wave frequencies [3, 8].

Millimeter wave frequencies offer the potential for high data rate, low latency communications beyond that of today's wireless networks. From Shannon's theorem, the theoretical maximum data rate of a communication system is given by [37]

$$C = Blog_2\left(1 + \frac{S}{N}\right) \tag{2.1}$$

where C is the channel capacity, or maximum achievable data rate, in bits per second, B is the channel bandwidth, S is the received power in the channel bandwidth in Watts (W), N is noise power in the channel bandwidth in W, and the ratio, $^{S}/_{N}$, is the signal-to-noise ratio. From Eqn. (2.1), the channel capacity can be increased by increasing bandwidth, or increasing the signal-to-noise ratio. The current spectrum licensed for mobile communications has become very crowded so there is not much to be gained in the way of bandwidth and service providers are forced to look elsewhere.

In the millimeter wave regime, vast amounts of licensed and unlicensed spectrum are available compared to frequency bands allocated for previous mobile generations. Furthermore, a smaller percentage bandwidth can lead to more overall bandwidth for the communications system with higher operating frequencies. For example, many LTE systems operate in the 1695-2690 MHz range where there is approximately 1 GHz of bandwidth available to be distributed among all the carriers operating in that range. This corresponds to a fractional bandwidth of 45%. One of the proposed frequency bands for 5G studies in the United States is the 27.5-29.5 GHz band [38]. This only corresponds to a 7% fractional bandwidth, but there are 2 GHz of total bandwidth to be shared among the operators in that band. Assuming similar signal to noise ratios can be achieved, this corresponds to a 2X increase in maximum achievable data rate over the 1695-2690 MHz LTE bands.

The use of millimeter wave spectrum also presents unique challenges for the antenna engineer. Fabrication and reliable testing at these frequencies is much more difficult than for today's base station antennas, but the design of the radiating structure is generally less difficult with smaller percentage bandwidths. The size of the radiating structure also decreases with higher frequencies, and more antennas can be implemented in a smaller footprint as shown in Fig. 2.5. This opens the door for lens and massive MIMO solutions incorporating many antenna elements that may not be practical at lower frequencies due to size limitations. Low-loss waveguide and horn antennas will also become practical for 5G systems as frequencies increase and system efficiencies must be optimized. The required radiation patterns for 5G base station antennas will be largely application specific. For example, self driving vehicles will likely require a high gain, pencil beam that tracks the vehicle in order to maintain continuous communication, but dense small cell deployments in an urban environment may benefit from wider beamwidth that makes use of multipath reflections off of buildings and other structures, especially if MIMO is to be used in the system.

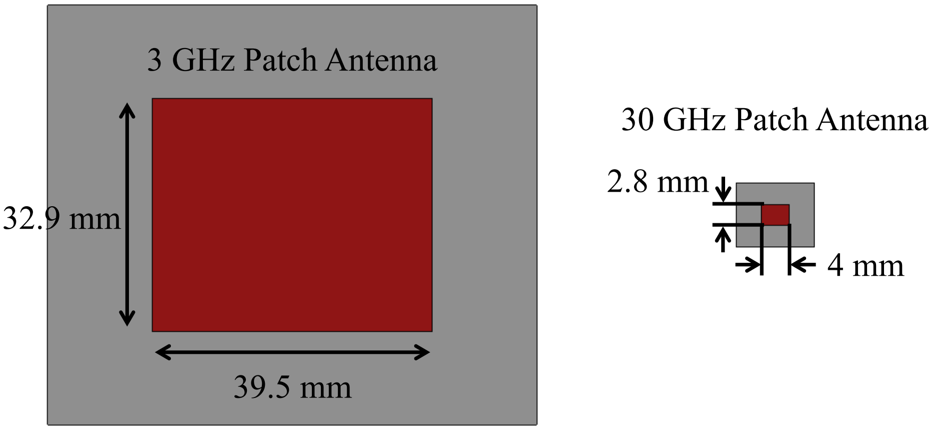

Figure 2.5: Size comparison for a 3 GHz patch antenna on 1.57 mm Duroid ($\epsilon_r \sim 2.2$, tan$\delta \sim 0.0009$) and a 30 GHz patch antenna on 0.762 mm Duroid.

One of the challenges to the use of higher frequencies for next generation mobile networks is the corresponding increase in path loss with increasing frequency. The path loss in free space can be determined from [39]

$$FSPL = \left(\frac{4\pi df}{c_0}\right) \tag{2.2}$$

where d is distance from the source, f is frequency, and c_0 is the speed of light in a vacuum. Clearly, increasing frequency corresponds to increased path loss. While it has been shown that path loss is not prohibitive for mmWave 5G networks, it will require densification to provide the coverage and capacity as promised [3,40–42]. With zoning restrictions and the inability to place antennas anywhere service providers choose, 5G base station antennas will inevitably be integrated into structures that also provide coverage for technology of previous mobile generations. This means that the base station antennas may have to support frequencies as low as approximately 600 MHz and as high as 70 GHz creating many challenging and exciting opportunities for the base station antenna engineer.

One of the challenges with the addition of new spectrum is interference management. With many antennas of various frequency bands operating in close proximity and the need to maintain receiver sensitivity for optimal network performance, filtering antennas will become a necessity. As previously stated, one of the challenges with higher frequencies is the path loss associated that is directly proportional to frequency, and a noisy transmitter that produces spurious signals can lead to interference and other network problems that degrade system performance. Furthermore, mobile network providers may operate in bands that are near other services or unlicensed where interference can be problematic for the overall system. Filtering antennas will be a key component of next generation mobile base stations.

The densification approach for capacity enhancement also creates a need for antennas with unique pattern performance that may not have been required for base station antennas of previous generations. This is particularly true in the urban environment. For example, consider an antenna mounted along a city street designed to provide coverage up and down the street. In this case, a bidirectional antenna that radiates up and down the street is desirable. Bidirectional antennas have received attention in recent years, especially for communication in tunnels and mines as well as along urban streets [43–46]. Similar principles apply for 5G network enhancement along city streets. Another example of an antenna requiring a unique radiation pattern due to densification is the antenna mounted to the side of a building. In this case, the antenna may require a 180° beamwidth so that the antenna provides coverage for users outside of the building but does not interfere with an in-building antenna system. Extending this concept a bit, the antenna mounted on a street corner might requrie a 270° beamwidth for the same reasons described above. This is not a trivial problem to solve, and the antenna may require some set of reflectors and directors or some form of an array to generate the desired patterns. From filtering antennas to pattern shaping, there is no shortage of challenges to design antennas that meet the demands of tomorrow's mobile networks.

2.4 Summary

This chapter gave an overview of state of the art in current generation (4G) base station antenna technology and a short discussion on next generation (5G) base station antenna technology. Although 4G deployments are in progress all over the world, there are always needs to improve coverage and capacity driving the need for innovative antenna solutions. The next generation of wireless technology is still very much in the research and development phase where standards are still being developed. As service providers look to millimeter wave frequencies to provide 5G solutions, base station antenna developers are forced to invest heavily in research and development as a new regime in RF/antenna technology is explored

CHAPTER 3: METAMATERIALS AND FILTERING ANTENNAS

3.1 Introduction

This chapter provides a background on metamaterials, filters, and filtering antennas. In recent years, many filtering antennas have been realized using metamaterial based structures, but this is not always the case. This chapter examines filtering antennas with and without metamaterial structures. The chapter begins with a general metamaterial discussion followed by a discussion on filters with a focus on the filtering properties of metamaterials. Metamaterials research has grown since the late 1990s and early 2000s due to the ability to control electromagnetic fields in unique ways [47–52]. Metamaterials have been used on many accounts to achieve negative effective permeability or permittivity. This chapter shows that these effects can be used to achieve interesting devices that exhibit filtering response based on negative effective permeability or permittivity.

The need for filtering antennas has grown over the years due to spectrum crowding and the desire to pack more antennas into smaller spaces particularly for base station applications. Furthermore, densification for 5G network enhancements also increases the potential for harmful coupling and interference in antenna systems. This chapter presents background material on current state of the art in filtering antennas. In some cases, filtering antennas are based on metamaterial structures, but this is not a requirement and is not always the case. The antennas preented in this dissertation primarily utilize metamaterial structures to achieve filtering, but a thorough discussion of all types of filtering antennas is presented here. This chapter presents the foundation of the research presented in this dissertation.

3.2 Metamaterials and Filters

Metamaterials have emerged in the last fifteen to twenty years as part of a revolutionary field in electromagnetics where engineered materials and structures have been developed to manipulate electromagnetic waves in ways that were once considered impossible. This section provides a general discussion on metamaterial concepts and a focused discussion on the application of metamaterial techniques to achieve filtering antenna structures. We begin with a general discussion of filter concepts followed by discussions of metamaterials, their application in filters, and a discussion on filtering antennas.

3.2.1 Filter Basics

Filters are essential components of wireless communications systems providing a means for passing desired freqency bands and rejecting unwanted frequency bands. The ideal response for the four basic filter types are shown in Fig. 3.1 [53, 54]. Note that these responses are ideal, and the sharp roll-of shown in the plots at the cutoff frequencies is not generally realizable. The filter response of real filters generally follows a butterworth, chebyshev, elliptic, etc. type of response as shown in Fig. 3.2. At frequencies below approximately 1 GHz, filters can sometimes be realized using lumped element components, i.e. inductors and capacitors. Unfortunately, this is not generally the case at frequencies higher than 1 GHz, and distributed or transmission line filters may be required.

Butterworth and Chebyshev filters are two of the more commonly used filter types for microwave applications where numerous textbooks and countelss publications are dedicated to these filter designs. As a design example, consider a four-element Butterworth low pass filter (LPF) designed according to [53, 54]. We start with the four-element filter circuit shown in Fig. 3.3a.

The filter is designed for a cutoff frequency of 3 GHz giving the prototype values

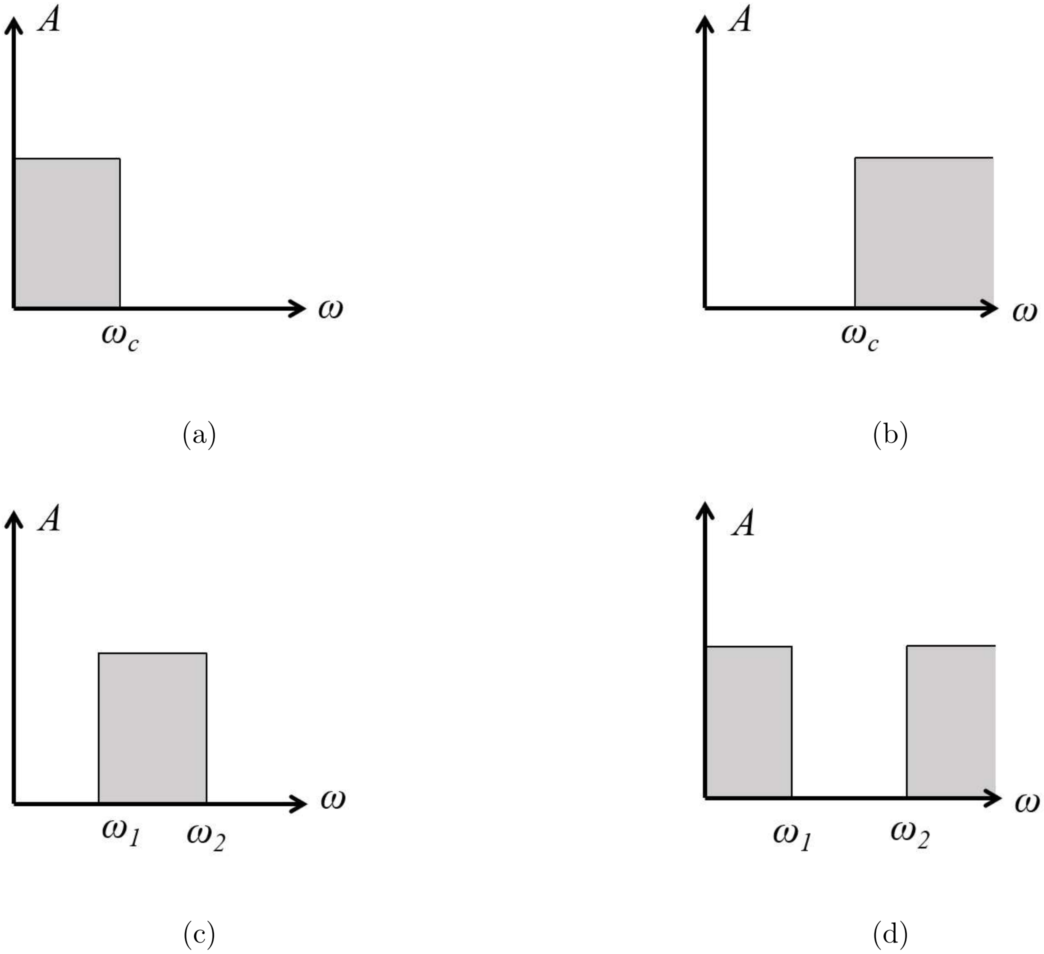

Figure 3.1: Frequency response for the ideal low-pass filter (a), high-pass filter (b), band-pass filter (c), and band stop filter (d).

according to the tables in [53, 54] as $g_0 = 1$, $g_1 = 0.7654$, $g_2 = 1.8478$, $g_3 = 1.8478$, $g_4 = 0.7654$, and $g_5 = 1$. The filter is designed for a cutoff frequency of 3 GHz giving the inductor, L, and capacitor, C, values to achieve the desired filter response as

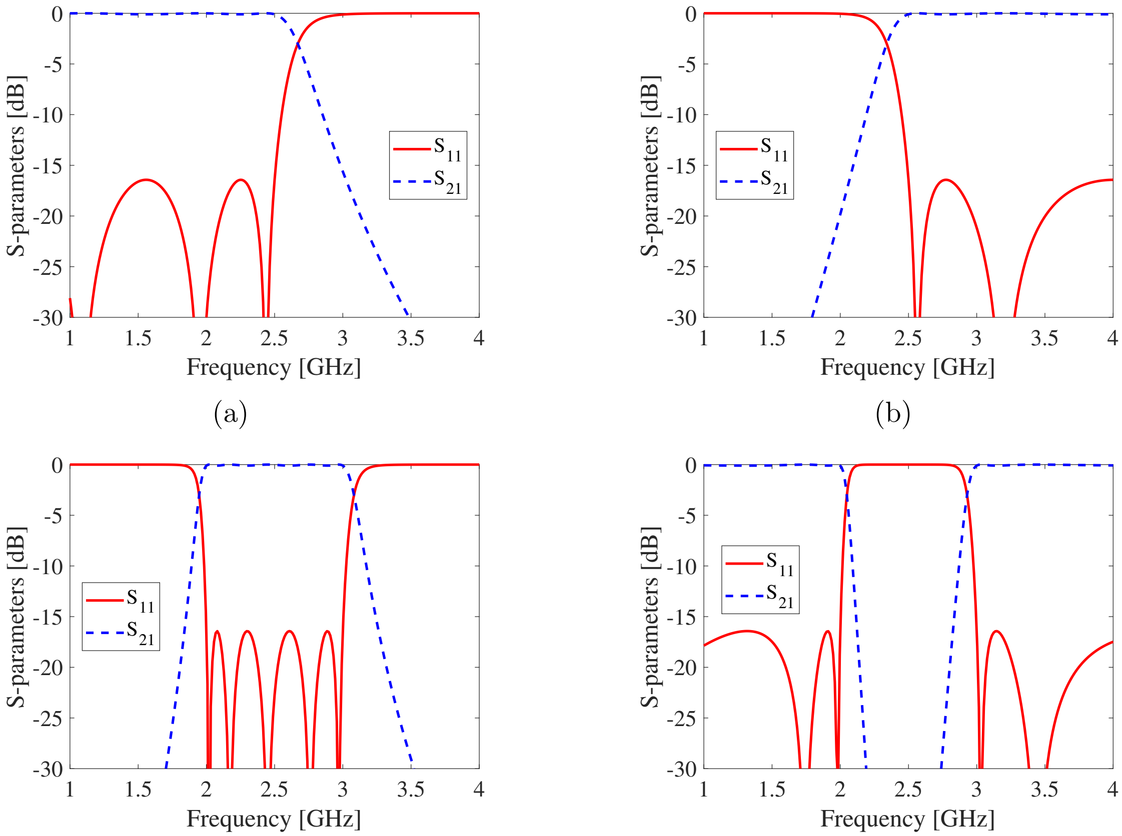

(a) (b)

(c) (d)

Figure 3.2: Frequency response for a 7-element Chebyshev low-pass filter (a), a 7-element Chebyshev high-pass filter (b), a 5-element Chebyshev band-pass filter (c), and a 5-element Chebyshev band-reject filter (d).

$$C_1 = \frac{g_1}{R_0\omega_c} = 0.812\ pF \tag{3.1}$$

$$L_2 = \frac{R_0 g_2}{\omega_c} = 4.901\ nH \tag{3.2}$$

$$C_3 = \frac{g_3}{R_0\omega_c} = 1.961\ pF \tag{3.3}$$

$$L_4 = \frac{R_0 g_4}{\omega_c} = 2.03\ nH \tag{3.4}$$

where ω_c is the cutoff frequency of the prototype LPF, and R_0 is the system impedance. The filter resposne is shown in Fig. 3.3b. The cutoff frequency is shown to be f_c, and the insertion loss rolls off to 20 dB around 5.3 GHz. Note that the required roll-off determines the order and type of filter used. The charts in [53, 54] can be used to determine the filter order based on the desired roll-off.

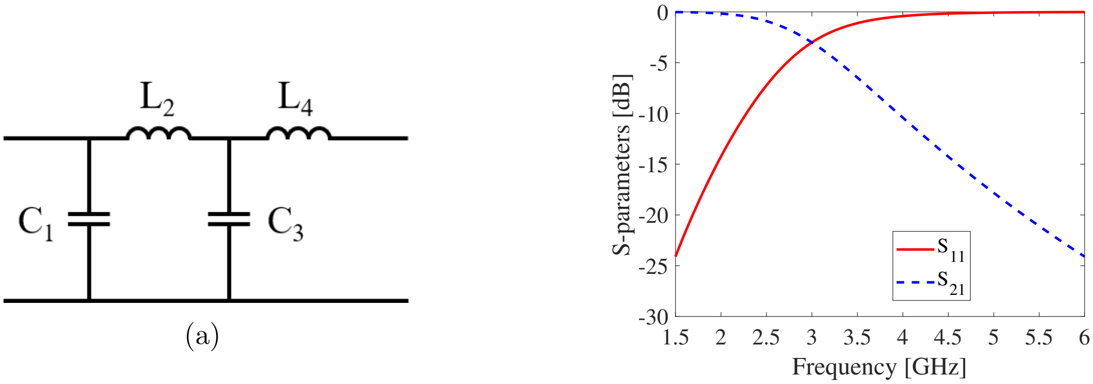

(a)

(b)

Figure 3.3: A 4-element Butterworth LPF (a) and its frequency response (b).

The prototype LPF is generally used as the starting point in filter design, but it can be easily converted to a high-pass, bandpass, bandstop filter by using transformations presented in [53, 54]. This process essentially involves frequency transformations and transformations of the inductors and capacitors of the LPF. The high pass filter requires changing capacitors for inductors and vice versa where bandpass and band stop filters require series and parallel combinations of inductors and capacitors.

3.2.2 Metamaterial Concepts

On a macroscopic level, the interaction between a material and electromagnetic energy can be characterized by the material's electric permittivity, ϵ, and magnetic permeability, μ. The relationships between these quantities and the electric and magnetic fields, **E** and **H**, can be found from Maxwell's equations [55]

$$\nabla \times \mathbf{E} = \mathbf{J}_m - j\omega\mu\mathbf{H} \tag{3.5}$$

$$\nabla \times \mathbf{H} = \mathbf{J}_e + j\omega\epsilon\mathbf{E} \tag{3.6}$$

$$\nabla \cdot \epsilon\mathbf{E} = q_e \tag{3.7}$$

$$\nabla \cdot \mu\mathbf{H} = q_m \tag{3.8}$$

where **E** and **H** are the electric and magnetic field vectors, respectively, $\mathbf{J}_e$ is the electric current, $\mathbf{J}_m$ is a fictitious magnetic current density, q_e is the electric charge, and q_m is a fictitious magnetic charge.

The permittivity and permeability can also be written as

$$\epsilon = \epsilon_0\epsilon_r = \epsilon_r \cdot 8.854 * 10^{-12} \left[\frac{Farads}{meter}\right] \tag{3.9}$$

$$\mu = \mu_0\mu_r = \mu_r \cdot 4\pi * 10^{-7} \left[\frac{Henries}{meter}\right] \tag{3.10}$$

where ϵ_0 is the permittivity in a vacuum, and μ_0 is the permeability in a vacuum. From Eqns. 3.9 and 3.10, the relative permittivity, or dielectric constant, ϵ_r, and relative permeability, μ_r, act as scaling factors to determine the level of interaction between a material and the incident fields relative to that of a vacuum. Note that these terms generally vary with frequency and temperature, and they can become rather complicated depending on the material. For example, tensor materials exhibit properties that vary depending on the direction of the excitation field. No matter the complexity of the material, ϵ_r and μ_r are generally positive and greater than 1 in naturally occurring passive materials [48, 56].

Formulations for what has become the field of metamaterials were first published in 1968 by Veselago where he studied the theoretical behavior of wave propagation in double negative media where both the relative permittivity, ϵ_r, and relative permeability, μ_r, were < 0 [57]. Veselago showed that in the presence of dispersion, negative ϵ and μ does not violate conservation of energy, and he also discussed interesting phenomena such as backward wave propagation and negative refraction. This work did not receive significant attention until the 1990s when Pendry proposed a passive unit cell capable of negative effective permeability [47]. Interest in the field grew, and in 2001, Smith et. al. published results demonstrating simultaneous $-\epsilon_r$ and $-\mu_r$ catapulting the field of metamaterials [49]. Since that time, many scholarly papers and books have been published on the subject, but the premise is generally engineering control of the effective material ϵ_r and/or μ_r [50–52, 58, 59].

Metamaterials are generally fabricated as metallic inclusions embedded in some host dielectric material as shown in Fig. 3.4 where the metallic inclusions are commonly resonant in order to provide negative effective ϵ_r or μ_r. Resonance is generally required in passive metamaterials so that the unit cell generates an $\mathbf{E}$ or $\mathbf{H}$ field that opposes the incident field emulating a negative effective ϵ_r or μ_r. One of the interesting features of metamaterials with negative parameters is that double negative metamaterials support wave propagation, but single negative metamaterials do not [48]. Single negative metamaterials are materials where only ϵ_r or μ_r is negative but not both simultaneously. Figures 3.5 and 3.6 show two common single negative metamaterial structures and their electromagnetic responses.

The split ring resonator (SRR) in Fig. 3.5a predominantly interacts with the incident magnetic field to produce $-\mu_r$. The electric disk resonator (EDR) in Fig. 3.6a predominantly interacts with the incident electric field to produce $-\epsilon_r$ [60]. To obtain S-parameters, the structures are modeled inside of a parallel plate waveguide section as discussed in [59]. Notice the high reflection coefficient in Figs. 3.5b and 3.6b where the unit cells exhibit $-\epsilon_r$ or $-\mu_r$ where no energy propagates. This suggests the utility of these structures for microwave filtering applications.

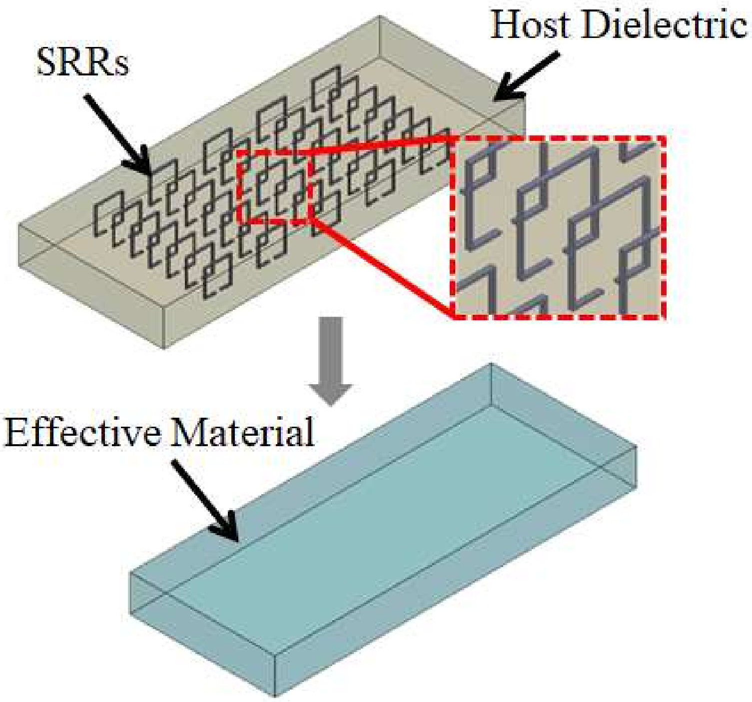

Figure 3.4: Effective material concept for SRRs embedded in a host dielectric material.

3.2.3 Metamaterial Filtering

The basis of filter design lies in the frequency selective response of a particular structure or circuit. The last section demonstrated the frequency selectivity of the SRR and the EDR indicating the potential of these structures for filtering applications. These are only two of a large number of structures that have been used for metamaterial designs and metamaterial based filters, but they serve as good examples to illustrate metamaterial filtering concepts. Metamaterials have become a focus for filter design only partially due to their frequency selective nature. Another appeal of metamaterials is their small size where the resonant elements are commonly only a fraction of a wavelength in overall size. This leads to fairly easy integration of these elements into transmission line and antenna structures, and in some cases, it allows

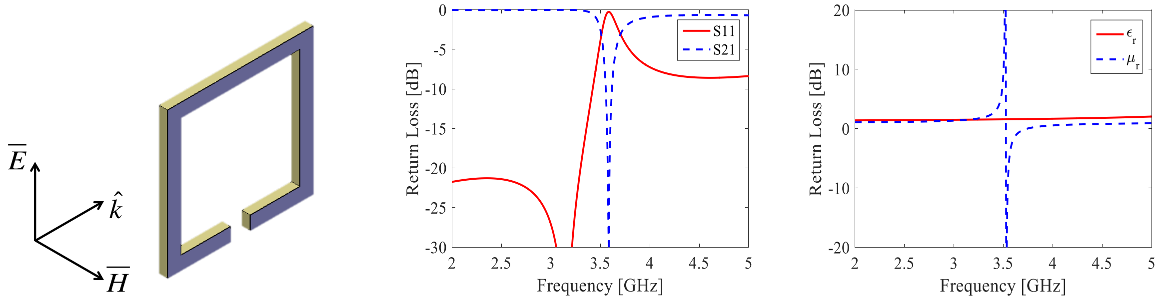

(a) (b) (c)

Figure 3.5: Split ring resonator with fields orientation (a), S-parameters (b), and extracted material parameters (c).

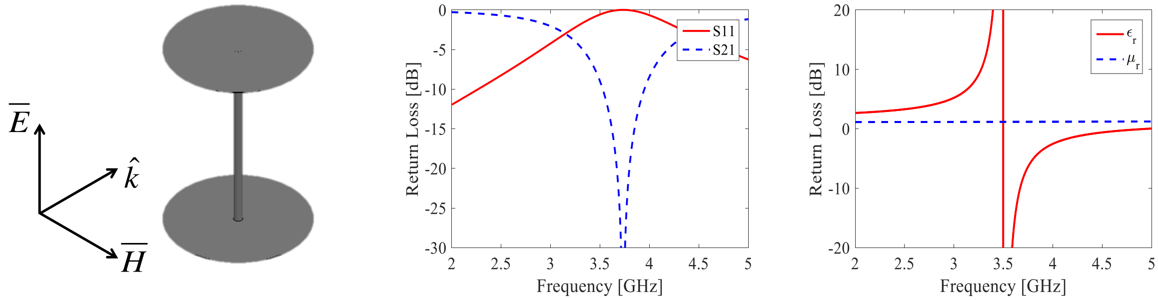

(a) (b) (c)

Figure 3.6: Electric disk resonator with fields orientation (a), S-parameters (b), and extracted material parameters (c).

for equivalent circuit modeling to assist in the design process.

The use of metamaterial structures in guided wave filtering applications involves proper alignment of the resonator with respect to the electric or magnetic fields in order to excite a particular resonant mode or set of resonant modes within the structure. Metamaterial filters have been applied to a variety of guided wave strcutures to realize low pass, high pass, band pass and band stop filters [61–68]. As an example of a parasitic waveguide filter, the SRR in Fig. 3.7 is aligned parallel to the electric field an transverse to the magnetic field. This is to ensure that the incident magnetic field passes through the SRR inducing an opposing magnetic field in the SRR leading to the response shown in Fig. 3.7b.

Printed circuit metamaterial filters have been widely investigated where the reso-

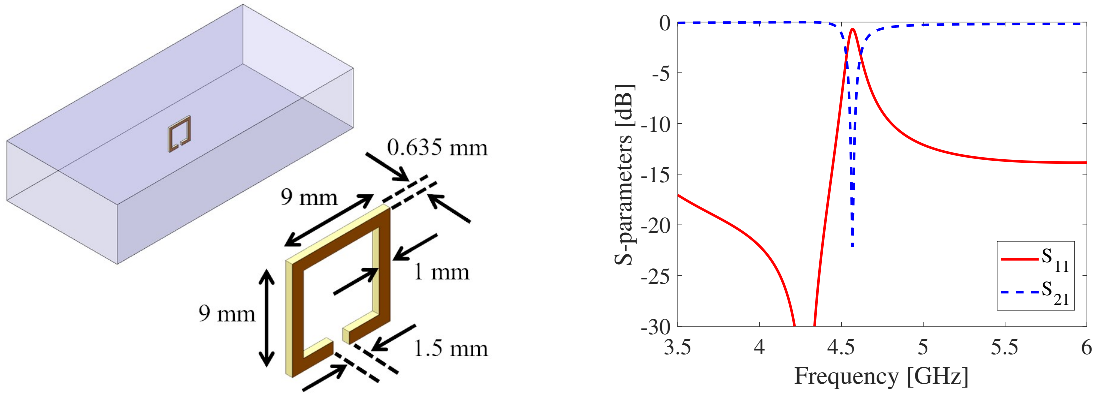

(a) (b)

Figure 3.7: A single SRR in WR-187 waveguide (a) and its frequency response (b).

nant structures can be parasitic or directly incorporated into a transmission line or ground. As an example of a parasitic printed circuit filter, a capacitively loaded strip is coupled to a microstrip trace to provide a narrow stop band at approximately 4.5 GHz in Fig. 3.8.

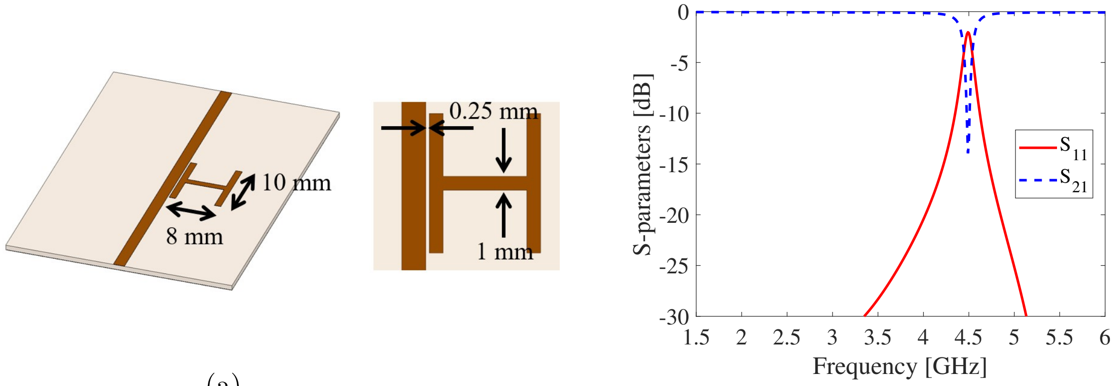

(a) (b)

Figure 3.8: A parasitic CLS filter coupled to a microstrip line (a) and its frequency response (b). The board material is 0.508-mm Rogers RO4003.

Defected ground and defected trace microstrip filters are also common for band stop applications where complimentary structures are etched or milled into the ground or signal traces. An example of a defected ground structure (DGS) filter is shown in Fig. 3.9 where SRRs are etched into the ground plane below a microstrip trace to realize a broad stop band [69].

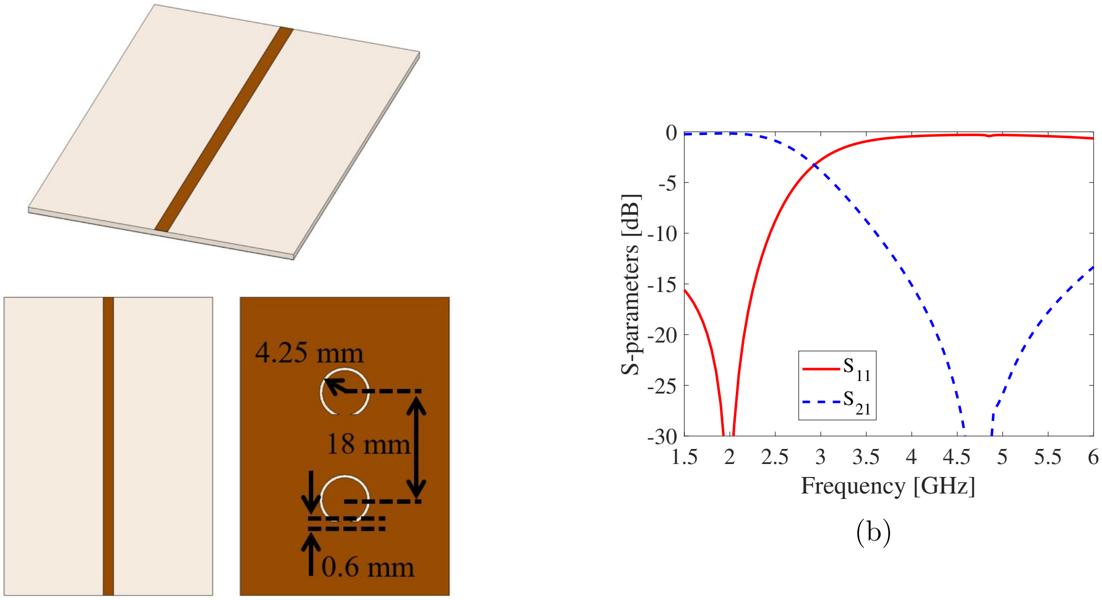

(a)

(b)

Figure 3.9: A DGS band stop filter (a) and its frequency response (b). The board material is 0.508-mm Rogers RO4003.

The reflective nature of metamaterial structures make them more widely used for band stop applications, but metamaterials have also been applied successfully in band pass applications. A band pass filter is shown in Fig. 3.10 where two coupled SRRs are integrated into a microstrip trace to realize a passband near 2.3 GHz [70].

There has also been significant interest in equivalent circuit modeling for metamaterial structures where RLC models have been generated for various metamaterial structures with varying levels of accuracy and complexity. Although not always necessary, equivalent circuit models can aid the design of metamaterial-based filters especially when higher order filtering is desired.

3.3 Filtering Antennas

The introduction of wideband and multiband systems for base stations has led to a need for filtering to separate bands or limit interference and coupling. In some cases, wideband antenna elements are used, and the signal is passed through a multiplexer

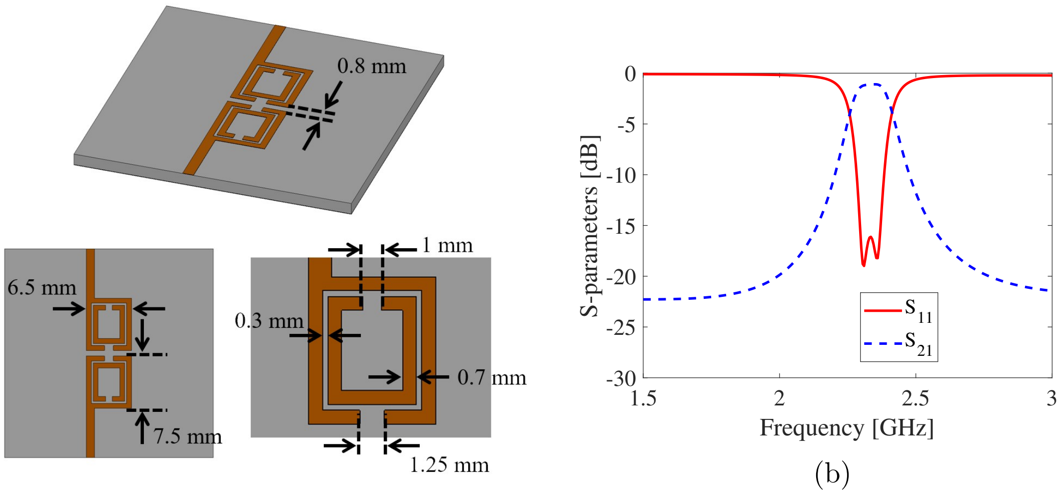

(a)

(b)

Figure 3.10: A microstrip band pass filter based on coupled SRRs (a) and its frequency response (b). The board material is 1.27-mm Rogers RT/duroid 6010.

to separate the bands of interest and provide an antenna port for each band. In other cases, it may be more practical to use separate antenna elements for each band, especially if beamforming is required. This eliminates the need for a diplexer or triplexer, but there remains a potential for interband interference which can degrade receiver sensitivity and overall system performance [71]. Additionally, network densification and spectrum saturation create a need for filtering to minimize noise in communications systems. Carrier frequencies between providers are generally very close, and network densification will continue to put base station antennas for different operators in closer proximity. The ability to easily filter any unwanted signals at the base station will become paramount to deliver increasing data rates and coverage.

Advanced 4G and 5G systems have introduced new spectrum that has not previously been used for mobile wireless communications. Bands in the 3-6 GHz range are currently being integrated into base station antenna designs that used to only provide coverage up to ∼2.7 GHz. There is also considerable interest in spectrum at higher frequencies such as the 15 GHz and the 28 GHz bands, and industry and academia have invested heavily in the development of antenna technology at these bands. These developments enable significant enhancements for mobile wireless services, but they also create a need for band stop and low pass filters to suppress possible harmonics generated by antennas operating at lower frequencies. These harmonics could cause system degradation, and with the relative antenna sizes of the lower band antennas, they can exhibit considerable gain at the higher frequencies that could be destructive for these advanced mobile services. Harmonics can be significantly problematic, but they are not the only concern. Coupling between these systems can cause low isolation between antenna ports, difficulties with pattern control, and PIM issues as mentioned earlier enhancing the need for interference management filters.

Antennas with integrated filters offer a compact solution and eliminate the need for separate filter components which can add loss and size to the system. Due to their small size, reflective nature, and frequency-selective response, single negative metamaterial structures present an elegant approach to antennas with integrated filters particularly in instances where stop bands are required for interference management. Though their use specifically in base station antenna systems has been limited, resonant metamaterial structures have been applied in a variety of filtering antenna applications using printed circuit and waveguide technologies [52, 61, 63–68, 72]. Filtering antennas typically utilize low pass, bandpass, or bandstop filters to achieve the desired antenna/filter performance. The antenna generally exhibits performance similar to a high pass filter where the antenna does not operate below a lowest order resonant frequency. However, there could be instances where high pass filters integrated into antennas are desirable for coupling mitigation between two antennas with different operating bands. The focus of this dissertation is primarily on antennas with integrated band stop filters for interference management.

There are two basic approaches for integrated antenna/filter design. The first approach is integration of the filter into the feed portion of the antenna (Filter-in-Feed or FiF), and the second is integration of the filter directly into the radiating structure (Filter-in-Antenna or FiA). The FiF approach is generally easier and offers the most flexibility in the filter design where the FiA approach is generally more difficult but offers the most compact solution. These techniques are described in detail in the following sections.

3.3.1 Filter Integrated Into Feed

The most straightforward method for the realization of filtering antennas is integration of the filter into the feed portion of the antenna. This will be referenced as the filter-in-feed (FiF) aproach for this dissertation. The FiF approach has been widely implemented for various antenna types and is common in microstrip-fed and waveguide antennas due to the ease of implementation. Band stop FiF approaches are illustrated in [69, 73–83] to eliminate in-band interference or suppress harmonics. Specifically, the authors of [69, 73, 75] implement metamaterial based approaches to achieve filtering.

Bandpass FiF approaches are illustrated in [84–97]. One design method for the bandpass FiF approach is to use a wideband antenna and let the filter set the operating band of the filter/antenna combination. In another design method, the filter may behave similar to a matching circuit into the antenna. In this case, the antenna loads the filter, and this load is partially used to set the operating band of the filter/antenna combination. Additionally, the antenna may be treated as the n-th resonator in an n-th order filter. In any case, the loading effects between the filter and antenna must be considered.

It is also desirable to have the ability to tune or reconfigure the filter for various frequencies. Interfering signals may have different frequencies depending on the mounting location and environment. Furthermore, the interfering singals may change frequencies so an antenna mounted in a particular environment may need to have the ability to change its filtering response based on how the interference changes in the environment. This is most commonly realized with varactors or some form of a switch where a control voltage can be changed to modify the feed characteristics and tune the resonant frequency or frequencies of the filter. For instance, PIN diodes are used to select between two RF paths where each path has a distinct filtering response in [98, 99]. Varactors are used in [100] to control resonant frequencies by adjusting a control voltage to modify the capacitance of the varactor.

As an example of a FiF antenna, a microstrip patch antenna is integrated with a broadband band stop filter in Fig. 3.11 using the approach presented in [69]. Like many antennas, the patch antenna exhibits higher order resonant modes where energy can be radiated by the antenna unintentionally creating interference for other wireless systems. The first 3 higher order modes for the patch antenna without a filter occur at 3.9 GHz, 4.6 GHz, and 4.85 GHz as shown in Figs. 3.11b and 3.11c. These modes fall in bands that are used by mobile wireless systems as well as other wireless systems, and interference can occur in these bands. The defected ground band stop filter integrated into the patch antenna feed line provides a rejection better than 1.05 dB from 2.45-6 GHz effectively eliminating these higher order modes. The peak gain for the antenna with and without the filter is plotted in Fig. 3.11c where the benefit of the filter is clear. At the higher order resonances, the peak gain is reduced by approximately 19.5 dB, 18.8, dB, and 12.8 dB. Note that some retuning is required for the antenna with the addition of the filter, but this only requires minor modifcation in the length of the patch.

3.3.2 Filter Integrated Into Radiating Structure

An alternative filtering antenna configuration is integration of the filter directly into the radiating element. This approach will be referenced as the filter-in-radiator (FiR) approach for this dissertation. The FiR approach is typically more difficult to implement, but integration of the filter into the radiating structure provides a more compact solution that is more desirable in many applications. One difficulty with this approach is that the physical size of the filter is often limited by the size of the

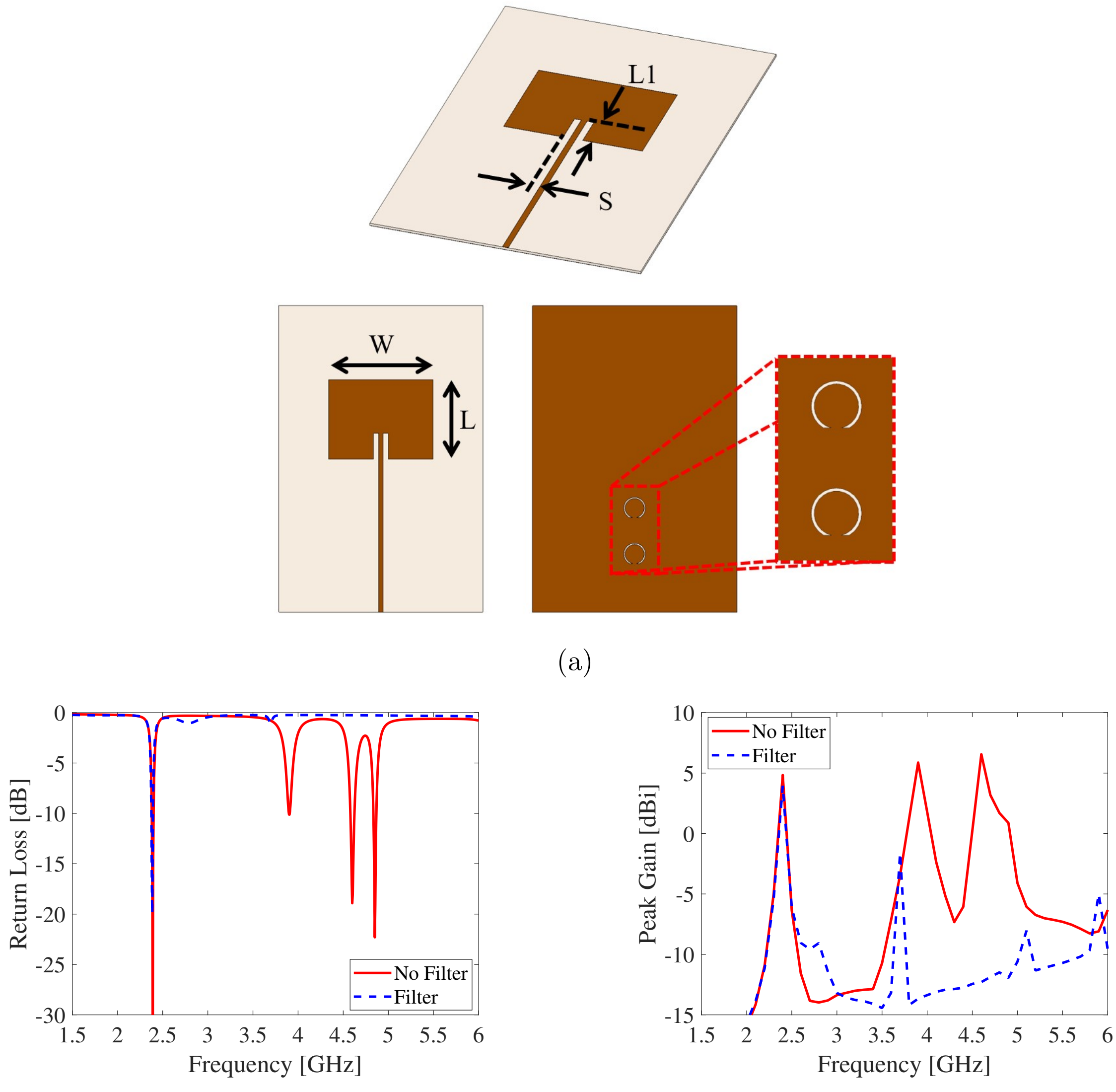

(a)

(b)

(c)

Figure 3.11: Patch antenna with two-element DGS filter integrated into the feed line (a) along with the return loss for the antenna with and without the filter (b) and gain with and without the filter (c).

antenna. As a result, it can be difficult to realize higher order filters. Additionally, this approach generally requires co-design of the filter and antenna since the two are integrated into the same structure.

The FiA approach is most common for wideband antennas that incorporate notch filters to block specific bands [101–108]. Ultrawideband (UWB) antenna systems operating from ∼3-11 GHz have received attention in recent years and are commonly used in medical applications. Unfortunately, there are a number of licensed and unlicensed frequency bands that fall within this band that could be problematic for UWB systems, and notch filtering is required to minimize interference. In a similar concept to handle interference mitigation, the authors of [65, 66] present the horn antenna with integrated notch filters based on metamaterial structures. Band stop FiA approaches are presented in [109–113] for harmonic suppression.

One interesting FiA approach is to make the filter also function as the radiating structure [114–118]. This technique exploits the frequency selective nature of antennas to realize bandpass antenna/filter combinations. The challenges with this approach are commonly bandwidth and pattern control. In order to achieve higher order filtering with reasonably high quality values (Q-values) and sharp roll off over a sizeable bandwidth, multiple filter elements are required. This can result in a travelling wave type of antenna where a highly directive radiation beam is formed, but the problem is that the direction of the main beam moves over frequency. As a result, the antenna provides different coverage areas vs. frequency, and this can be problematic for base station applications.

As an example of an FiA antenna, a broadband antenna with an integrated notch filter is shown in Fig. 3.12. The antenna forms a radiation pattern similar to a dipole as the ground plane of the feed structure also radiates. The filter is a complementary SRR etched into the upper radiator just beyond the feed point.

3.4 Summary

This chapter presented background on filters, metamaterials, and filtering antennas. Filters are fundamental in many communications systems, and wireless communication is not possible without antennas. Combining the filter and antenna to the greatest extent possible provides compact solutions. This also requries co-design between the filter and antenna, but this also makes for a robust filter/antenna system with optimal matching and system efficiency. Spectrum crowding and the growing

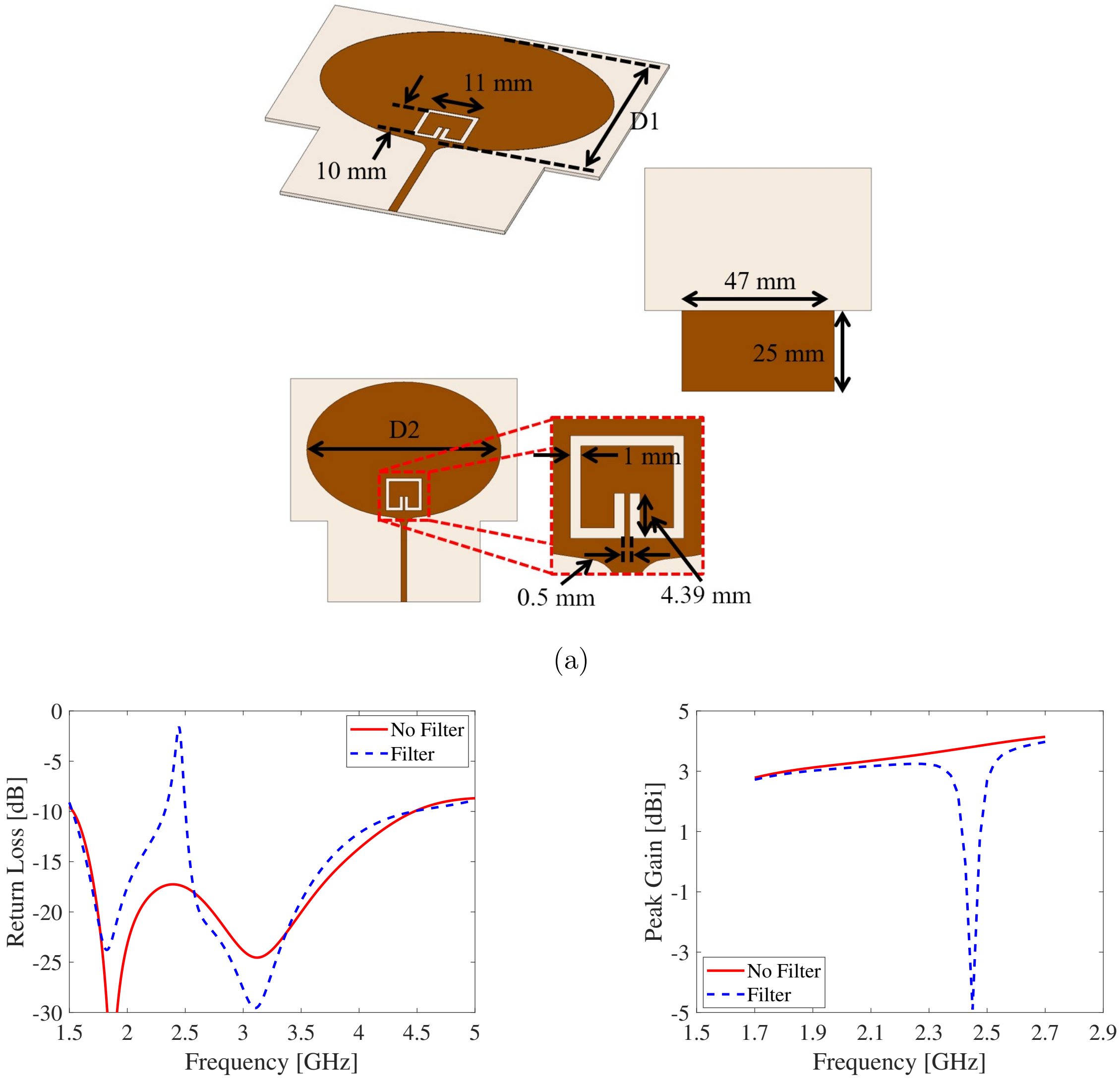

(a)

(b)

(c)

Figure 3.12: Broadband antenna with SRR filter integrated into the radiating structure (a) along with the return loss for the antenna with and without the filter (b) and gain with and without the filter from 1.7-2.7 GHz (c).

presence of multiband base station antenna systems requries unique filtering techniques, and integration into the antenna is an attractive solution. The information presented thus far serves as the technical basis for the antennas presented in this dissertation.

CHAPTER 4: HORN ANTENNA WITH GUIDED WAVE COUPLED RESONATOR FILTER FOR NEXT GENERATION BASE STATIONS

4.1 Introduction

This chapter presents the design and analysis of a horn antenna with integrated filter for advanced 4G and 5G mobile networks. The horn antenna is a promising candidate for high capacity systems where high gain, low loss, broadband performance can be achieved [119]. There is also interest in frequency bands from 3 GHz to millimeter wave frequencies (>30 GHz) where the size of horn antennas and waveguide feeds are not prohibitively large as they are at the lower frequencies of today's mobile networks. However, with unlicensed bands, the need for many carriers to broadcast in closely spaced bands, and network densification, filtering will be a requirement to reduce noise and out-of-band interference.

The horn antenna includes a notch filter integrated into the feed section for an FiF antenna where the filter is composed of two coupled split ring resonators (SRRs) designed by the Lagrangian formulation for metamaterials [120, 121]. It is shown that, depending on their orientation, coupled resonators can give a high degree of tunability based on manipulation of the electric and magnetic coupling parameters. As a result, the response of the filter can be tuned over wide bandwidths without a redesign of the fundamental resonant structures that make up the filter. Waveguide based filters have been presented in the literature [63–66], but none of these present a detailed method for reconfiguring or tuning the filter for a different center frequency without a redesign of the unit cell.

A WR-187 waveguide horn antenna with a recommended operating range from ∼3.95-5.85 GHz is investigated with two distinct notch filter configurations. Gap-coupled and broadside-coupled split ring resonators are considered where the relative spacing between the rings is varied to tune the resonant frequency. It is shown that broadside coupling offers tremendous advantages over gap coupling in terms of tunability. Simulations of broadside-coupled rings indicate tunability from ∼4-5.6 GHz with ∼52-144 MHz of instantaneous bandwidth. The coupling parameters are also used to investigate the rejection of the broadside-coupled filter over the tuning range. Numerical simulations of the radiation patterns confirm that the filtering element exhibits minimal impact to the antenna outside of the operating band of the filter. As a result, the filtering element can be placed close to the throat of the antenna for a compact solution. The horn antenna with three fixed broadside-coupled filters is fabricated and measured for gain and return loss; measured results confirm simulations and the design approach.

4.2 Lagrangian Formalism and Application to Guiding Structures

The most important design parameter for a notch filter of any type is the location of the resonant frequency. In metamaterial approaches, determination of the resonant frequency can be particularly challenging when coupling effects are considered. The Lagrangian formulation for metamaterials is used on several accounts to investigate the effects of coupling between structures forming bulk metamaterials [122–125]. For electrically small resonators in guiding structures, the quasi-static assumption is applied here for the response of the resonator at its lowest order mode, and the resonant dynamics of the structure are well approximated as a driven harmonic oscillator. The Lagrangian is applied under this assumption where the shifted resonant frequency is determined based on the coupling coefficients calculated from the self and mutual energies. This is similar to coupled mode theory [126] where the Lagrangian formulation acts as a means for easily calculating the coupling parameters and backing out the resonant frequencies.

Resonant frequencies for two closely spaced metamaterial structures such as the two split ring resonators in Fig. 4.1a are derived from the Lagrangian formulation as the result of two driven harmonic oscillators. The driving functions are dependent on the electric and magnetic coupling parameters, β and α respectively. A general form for the resonant frequencies of two resonators in the presence of coupling can be written as [122]

$$f_1 = \sqrt{\frac{f_{0_1}^2 Q_1 + \beta_{12} D f_{0_1} f_{0_2} Q_2}{Q_1 + \alpha_{12} D Q_2}} \tag{4.1}$$

and

$$f_2 = \sqrt{\frac{f_{0_2}^2 Q_2 + (f_{0_1} f_{0_2}/D)\, \beta_{21} Q_1}{Q_2 + (1/D)\, \alpha_{21} Q_1}} \tag{4.2}$$

where f_1 is the shifted resonant frequency of resonator 1, and f_2 is the shifted resonant frequency of resonator 2. The term f_{0_1} is the resonant frequency of resonator 1 in the absence of coupling, and f_{0_2} is the resonant frequency of resonator 2 in the absence of coupling. The coupling parameters, α, β, and D are found from the self and mutual energies as

$$\alpha_{12} = \frac{W_{m,12}}{\sqrt{W_{m,11} W_{m,22}}} \tag{4.3}$$

$$\beta_{12} = \frac{W_{e,12}}{\sqrt{W_{e,11} W_{e,22}}} \tag{4.4}$$

$$D = \sqrt{\frac{W_{m,22}}{W_{m,11}}} \tag{4.5}$$

where W_e denotes the electric energy and W_m denotes the magnetic energy. It should also be pointed out that the term Q in Eqns. (4.1) and (4.2) is the time dependent charge. This term serves as the generalized coordinate by which the Lagrangian is defined for metamaterial structures. The charge is assumed to be $Q \sim |Q|e^{j\omega t}$. The details for the generalized Lagrangian development are given in Appendix A.

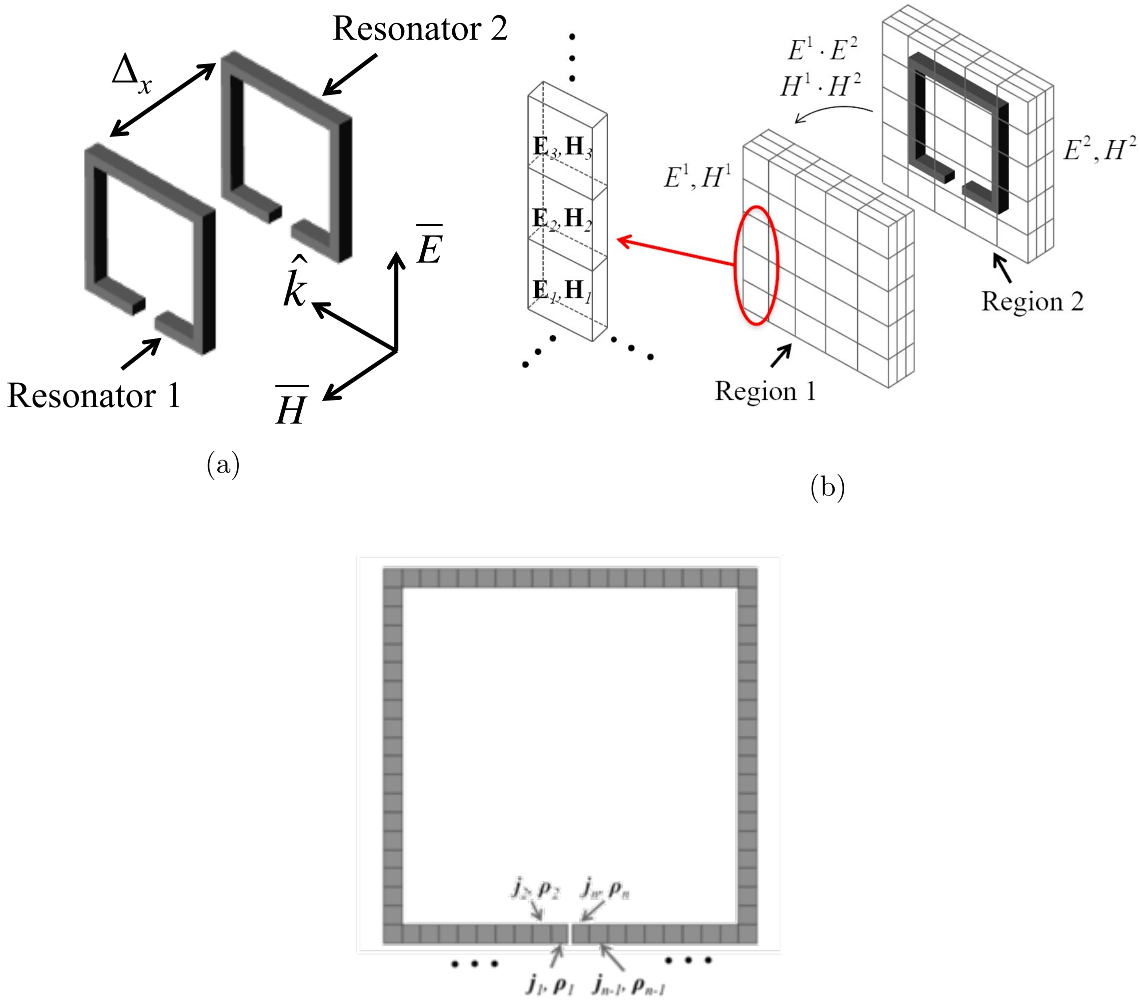

(a)

(b)

(c)

Figure 4.1: Two coupled split ring resonators (a) showing the alignment of the excitaiton field along with the direction of propagaiton. An illustration for the discretization enclosing a split ring resonator and coupled region (b) is also shown along with the discretization of a split ring resonator (c).

The self and mutual energies are calculated from the **E** and **H** fields along with the current and charge distributions obtained from full wave electromagnetic analysis. In some cases, image theory may be used to compute the coupling parameters in a waveguide based only on the current and charge distributions. Unfortunately, it is not always possible to successfully apply image theory, and inaccurate predictions of the resonant frequency may result. By using field terms, all electromagnetic interactions are considered, so accurate results are achieved in the presence of the guiding structure. This work marks the first time that a fields approach has been applied to determine the Lagrangian coupling coefficients. The electric and magnetic energies in terms of fields are written as

$$W_e = \frac{1}{2}\left[\int_v \epsilon \mathbf{E} \cdot \mathbf{E} dv' + \epsilon \oint_s V \mathbf{E} \cdot \hat{a}_n ds'\right] \tag{4.6}$$

$$W_m = \frac{1}{2}\left[\int_v \mu \mathbf{H} \cdot \mathbf{H} dv' - \oint_s (\mathbf{A} \times \mathbf{H}) \cdot \hat{a}_n ds'\right] \tag{4.7}$$

where the integration is taken over the area enclosing each resonant structure, and V and $\mathbf{A}$ are the electric scalar potential and the magnetic vector potential respectively. Note that in some cases, the terms containing V and $\mathbf{A}$ may be left out of Equations 4.6 and 4.7 as these terms fall off rather rapidly with distance from the source. For completeness, these terms remain in the equations.

To apply the Lagrangian formulation using the fields analysis discussed herein, the medium enclosing the resonant structure and the location where the second, coupled resonator would be placed are discretized into small segments indicated in Figure 4.1. The resonant structure can also be discretized into small segments to compute the surface charge and current on the structure. The necessary data is then calculated for each volume or surface and extracted for post processing. The energy equations become summations of Equations (4.6) & (4.7) and are written as

$$W_{e,pq} = \sum_{k_v=1}^{K_v} \frac{1}{2}\left[\int_v \epsilon \mathbf{E}_{k_v}^p \cdot \mathbf{E}_{k_v}^q dv'\right] + \sum_{c=1}^{C}\sum_{k_s=1}^{K_s} \frac{1}{2}\left[\epsilon \oint_s V_c^p \mathbf{E}_{k_s}^q \cdot \hat{a}_n ds'\right] \tag{4.8}$$

$$W_{m,pq} = \sum_{k_v=1}^{K_v} \frac{1}{2}\left[\int_v \mu \mathbf{H}_{k_v}^p \cdot \mathbf{H}_{k_v}^q dv'\right] - \sum_{c=1}^{C}\sum_{k_s=1}^{K} \frac{1}{2}\left[\oint_s \left(\mathbf{A}_c^p \times \mathbf{H}_{k_s}^q\right) \cdot \hat{a}_n ds'\right] \tag{4.9}$$

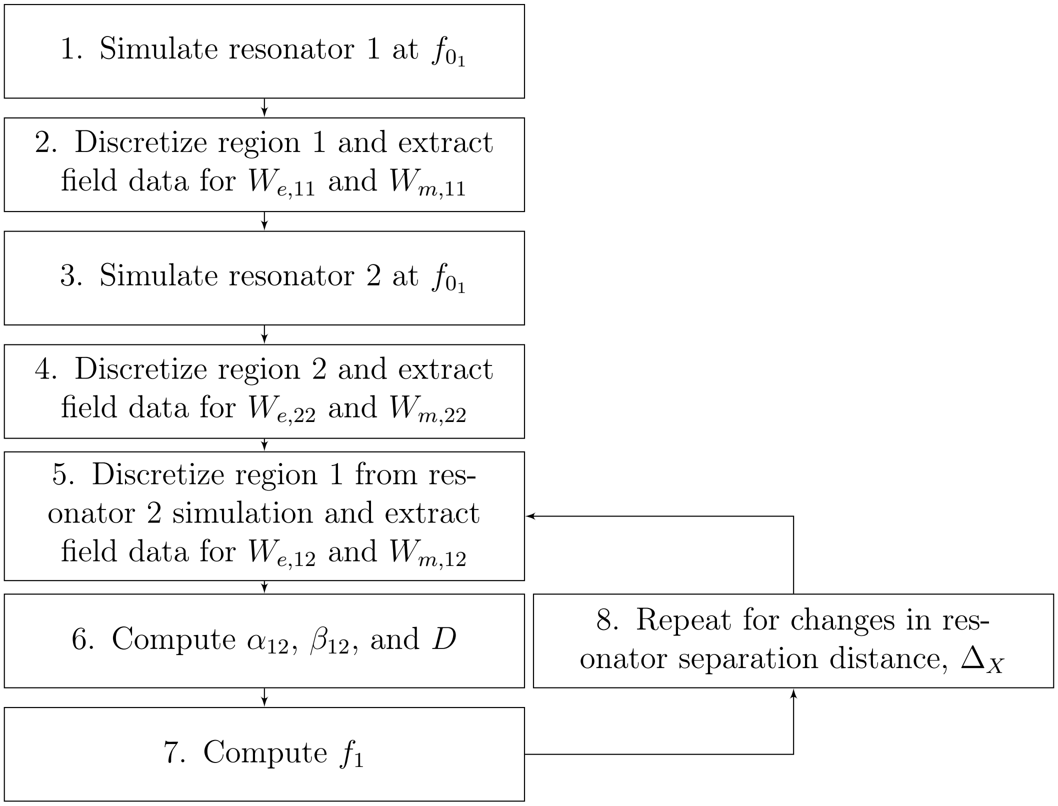

Figure 4.2: Flow chart illustrating the process to calculate resonant frequencies for coupled metamaterial structures using the Lagrangian method.

where the superscripts p and q indicate the fields generated by the corresponding resonator. The self energy is computed when $p = q$, and the mutual energy is computed when $p \neq q$. The subscripts, k_s and k_v, correspond to the respective discretized surface or volume element for the region surrounding the source or coupled structure. The subscript, c, corresponds to the respective discretized segment of the resonator.

It is clear from Equations (4.1)-(4.5) that manipulation of α and β, or more specifically the mutual energies, can be used to tune the resonant frequency. One way to do this is by varying the distance, Δ_X, between the resonant structures. The flow chart in Figure 4.2 illustrates the process for determining the resonant frequencies for two coupled resonators with variations in Δ_X. The following list further clarifies the simulation and analysis procedure outlined in Figure 4.2:

1. Simulate resonator 1 at f_{0_1} - resonator 1 is simulated in the operating environment

at its resonant frequency without including resonator 2. The data generated by this simulation is all that is needed to calculate the self energies $W_{e,11}$ and $W_{m,11}$.

2. Discretize region 1 and extract field data for $W_{e,11}$ and $W_{m,11}$ - the region within the guiding structure that encloses resonator 1 and the resonator are discretized, and necessary data is extracted for Equations 4.8 and 4.9.

3. Simulate resonator 2 at f_{0_1} - resonator 2 is simulated in the operating environment at the resonant frequency of resonator 1. Resonator 1 is not included in this simulation. The simulation is performed at f_{0_1} because we need to know the amount of coupling (electric and magnetic energy) between resonators 1 and 2 at the frequency f_{0_1}. The coupling at f_{0_1} determines the impact to the resonant frequency f_{0_1}. However, keep in mind that for the Lagrangian approach to apply, the resonator must be very close to resonance.

4. Discretize region 2 and extract field data for $W_{e,22}$ and $W_{m,22}$ - the region enclosing resonator 2 and the resonator are discretized, and the necessary data is extracted for energy computations. The data generated by this simulation is all that is necessary to calculate the self energies $W_{e,22}$ and $W_{m,22}$. Note that the volumetric discretization enclosing resonator 2 is performed to the same level as that for resonator 1, i.e. the same number of data points are used at the same relative positions. On the other hand, the discretizations of the two resonators may vary if the resonators vary in geometry.

5. Discretize region 1 and extract field data for $W_{e,12}$ and $W_{m,12}$ - in the full wave model for resonator 2, the region where resonator 1 would be placed relative to resonator 2 is discretized. The field data generated by resonator 2 in the region that would enclose resonator 1 for the coupled scenario is extracted to compute the mutual energies. This data along with the data extracted in step 2 is used to compute the mutual energies.

6. Compute α_{12}, β_{12}, D - use the extracted field data to compute the energies and the resulting coupling parameters.
7. Compute the shifted resonant frequency f_1 - using the coupling parameters, compute the shift on f_{0_1} as a result of coupling.
8. Repeat steps 5-7 for changes in resonator separation distance, Δ_X - repeat these steps as needed for various resonator spacings. Note that no more full wave analysis is required following the simulations of steps 1 and 3, only field extraction which is a post processing step.

For this investigation, the resonant structures are simulated using the finite element solver in HFSS to obtain the appropriate field data. MATLAB routines are used to perform the post processing and calculate the coupling parameters. Extraction of the field data requires a bit of scripting, but once the field data is extracted, the coupling terms and resonant frequency for a single value of Δ_X are computed in less than one second on a 2.6 GHz Intel Core i7 processor with 8 GB of RAM. It is evident from Figure 4.2 that the Lagrangian design method is an iterative process to find the appropriate spacing for a desired resonant frequency. However, the speed with which each iteration can be performed enables rapid convergence of a solution. Furthermore, this approach can be used as a rapid design tool to investigate the tunability or sensitivity of a particular set of resonators.

4.3 Filter Antenna Design

In this section, a coupled resonator notch filter for operation in the WR-187 waveguide band intended for future wireless base stations is presented. The WR-187 waveguide recommended operating range corresponds to 4G LTE bands 46 and 47 as well as frequencies under consideration for 5G. The dimensioned HFSS model for the horn antenna including the split ring resonator is shown in Figure 4.3. The horn antenna is designed according to [39] for approximately 15 dBi of gain at a center frequency of 4.9 GHz. The split ring resonator is designed for a resonant frequency near 5.74 GHz in the absence of coupling. Split rings are selected as the filtering elements due in part to the simplicity in design and fabrication. These resonators also give very controllable filtering that exhibits little interaction with the incident field outside of the dominant mode resonance location. This generally results in a very clean notch response with good performance outside of the notch band.

Two coupled split rings are considered in two distinct orientations, broadside-coupled and gap-coupled, as shown in Figure 4.4b. The rings are configured with their axes aligned so that there is no shifting between rings in the direction of propagation. The rings are varied by the amount, Δ_X, only in the direction transverse to propagation. The distance Δ_X is swept over a range of values initially to investigate tunability between the two configurations. In this case, the resonators are identical so $f_{0_1} = f_{0_2}$, $W_{m,11} = W_{m,22}$, $W_{e,11} = W_{e,22}$, and $Q_1 = Q_2$. The coupling parameters reduce to

$$\alpha = \frac{W_{m,12}}{W_{m,11}} \tag{4.10}$$

$$\beta = \frac{W_{e,12}}{W_{e,11}} \tag{4.11}$$

$$D = 1 \tag{4.12}$$

and the system of resonators exhibits a resonant frequency given by

$$f_r = f_0\sqrt{\frac{1+\beta}{1+\alpha}} \tag{4.13}$$

where f_r is the operating frequency of the coupled resonator notch filter. This solution is known as the symmetric coupling mode. As shown in [122] the other solution that satisfies the equations of motion for the system of identical resonators is the anti-symmetric mode where $Q_1 = -Q_2$. This solution is the result of resonance splitting and occurs when the current and charge are 180° out of phase between the two rings. This mode is generally only present when the rings are shifted relative to one another in the direction of propagation. As opposed to the approach in [120], the rings are allowed to shift only transverse to propagation, and the anti-symmetric mode is avoided altogether. This minimizes the possibility of unwanted resonances outside of the intended operating band of the filter.

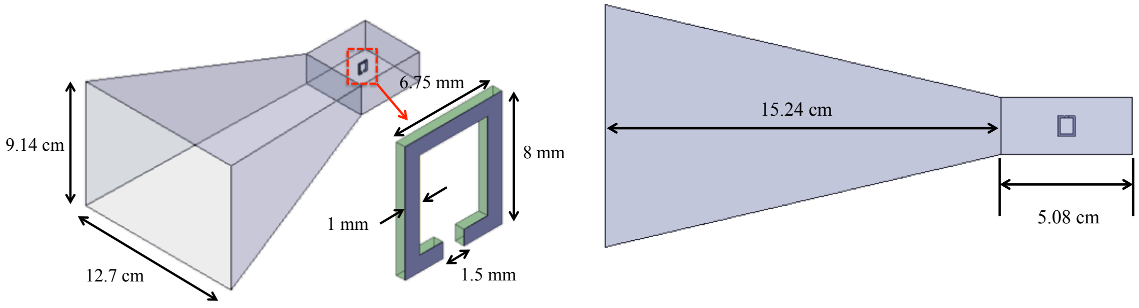

(a)

(b)

Figure 4.3: Horn antenna with SRR integrated into the feed portion. The isometric view (a) illustrates the horn and split ring dimensions and the side view (b) shows the length of the horn and the feed section. The split ring resonator was modeled on (1/32)" FR-4 with 1/2 oz. copper cladding. Note that the dielectric is modeled with a thickness of 0.7 mm to account for milling.

To determine the coupled resonant frequencies, individual rings are simulated in the feed section of the antenna in Figure 4.3, and the necessary data is extracted for post processing. It is found that a rectangular grid spanning 25.5 mm in x with 15 points, 15 mm in y with 31 points, and 15.25 mm in z with 14 points provides accurate solutions for the separation distances studied. The grid is also shifted by 0.25 mm in y so that none of the grid points fall directly in line with the metal of the SRR. Furthermore, simulation of the rings in the feed section only provides good enough accuracy for this study simplifying the design procedure. Following the numerical analysis, the coupling parameters in Equations (4.10) and (4.11) are calculated as described in the previous section, and the resonant frequencies are determined according to Equation (4.13). Note that the potential terms are not included for this analysis. The Lagrangian predicted resonant frequencies are plotted in Figure 4.4a over the range of Δ_X. The coupled rings in each configuration are also simulated in HFSS for comparison. Predicted resonant frequencies correlate very well with simulated data for distance variations in both split ring orientations. This illustrates the accuracy of the Lagrangian solution. It is also apparent from Figure 4.4 that broadside-coupled rings offer much more tuning bandwidth than gap-coupled rings.

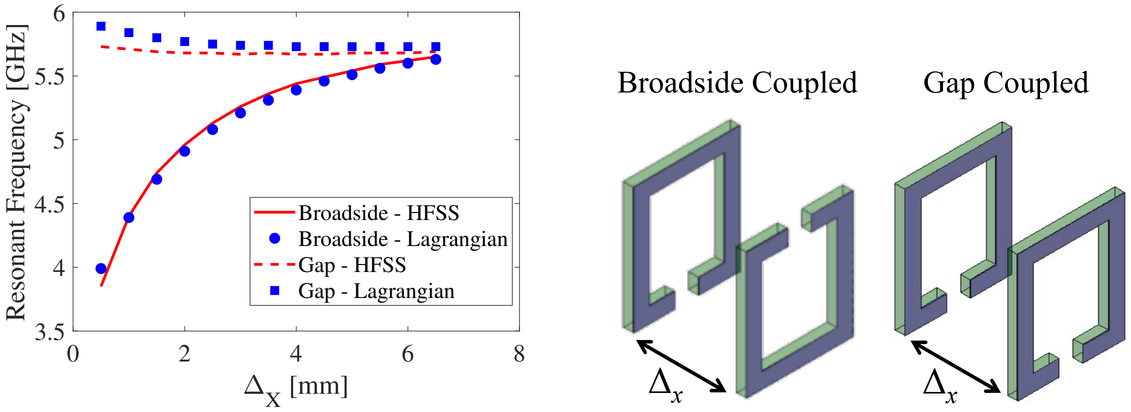

(a) (b)

Figure 4.4: Predicted and simulated resonant frequencies for broadside-coupled rings and gap-coupled rings with various spacing, Δ_x, (a) and illustration for broadside-coupled and gap-coupled split ring orientations (b).

The antenna performance is specifically investigated in HFSS for the rings in each configuration with separation distances, Δ_X, of 0.6 mm, 1.25 mm and 6.5 mm. These values for Δ_X give resonant frequencies near 4 GHz, 4.6 GHz, and 5.6 GHz for the broadside-coupled rings based on the Lagrangian anlaysis. Note that the 1.25mm spacing in [121] is erroneously labeled as 1.4mm, and the analysis in that paper assumes a dielectric thickness of 0.6 mm. Based on measurements of fabricated samples, the dielectric thickness appears to be closer to 0.7 mm which is the dielectric thickness used for the analysis in this dissertation. The simulated return loss and boresight gain data for the gap-coupled rings is shown in Figure 4.5 where the predicted resonant frequencies are confirmed. Even with significant variation in the distance between the rings, there is very little variation in the resonant frequency. The gap-coupled filter with rings spaced 0.6 mm, 1.25 mm, and 6.5 mm gives notch frequencies at 5.73 GHz, 5.7 GHz, and 5.67 GHz. The bandwidth for the three filter spacings varies from approximately 112-145 MHz determined by where the boresight gain is reduced by 3 dBi.

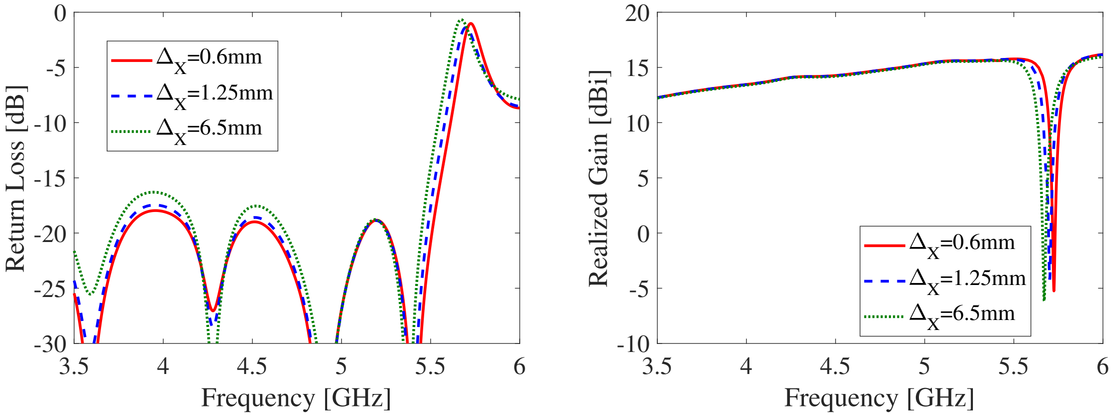

(a)

(b)

Figure 4.5: Simulated return loss (a) and normalized gain (b) for the horn antenna with three fixed filters of gap-coupled split rings with Δ_x set to 0.6 mm, 1.25 mm, and 6.5 mm.

Broadside-coupled rings, on the other hand, exhibit considerable tunability as indicated by the return loss and gain shown in Figure 4.6. The broadside-coupled filter with rings spaced 0.6 mm, 1.25 mm, and 6.5 mm exhibits notch frequencies at 3.98 GHz, 4.58 GHz, and 5.63 GHz which correlate with predicted resonances. The bandwidth for the three filter spacings varies from approximately 52 MHz at the lowest operating frequency to approximately 144 MHz at the highest operating frequency. Due to the significant tunability of the broadside-coupled rings compared to the gap-coupled rings, broadside coupling is the obvious choice for reconfigurable notch filter

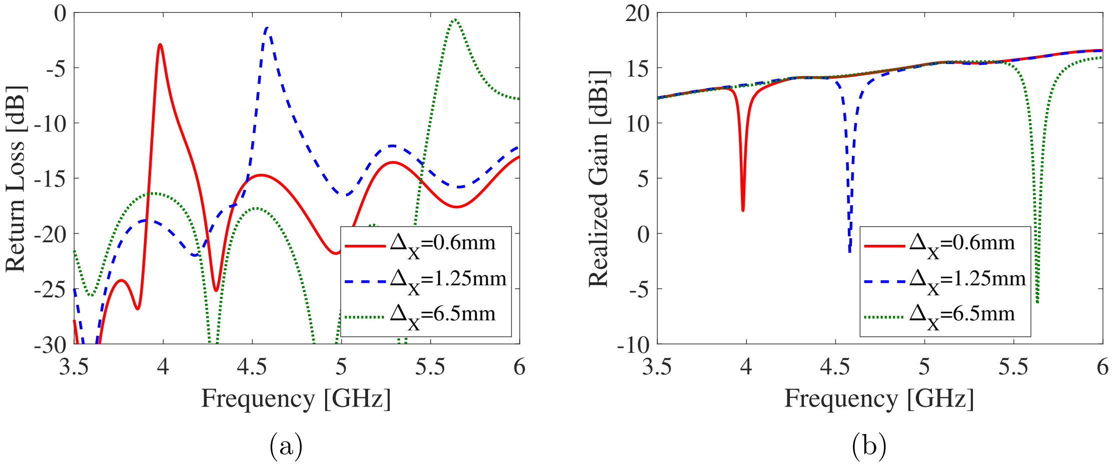

(a) (b)

Figure 4.6: Simulated return loss (a) and normalized gain (b) for the horn antenna with three fixed filters of broadside-coupled split rings with Δ_x set to 0.6 mm, 1.25 mm, and 6.5 mm.

solutions. A gap-coupled approach would only complicate the fabrication process while offering little tuning advantage.

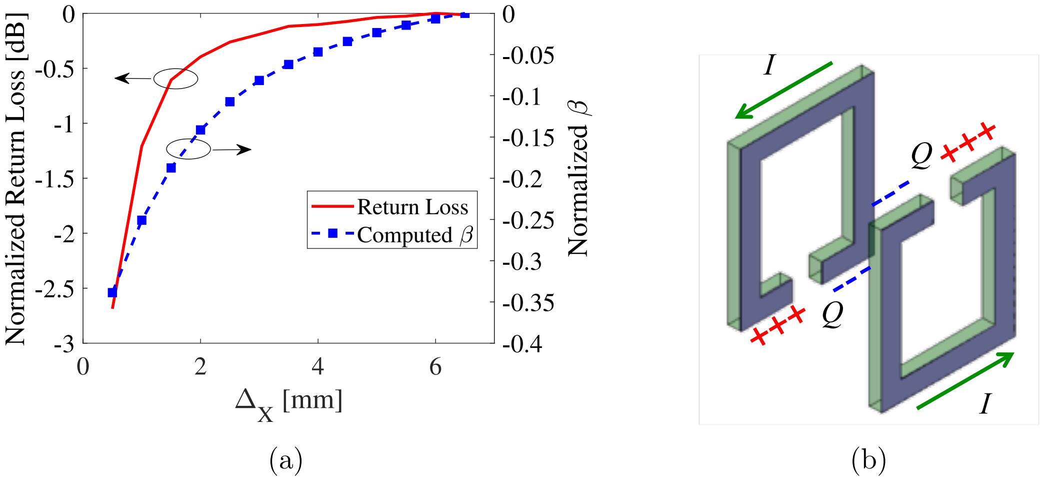

(a) (b)

Figure 4.7: Plot of normalized electrical coupling parameter, β, vs separation distance and simulated return loss in dB vs separation distance for broadside-coupled rings (a) and illustration of current and charge at resonance for broadside-coupled split rings (b).

Tremendous tuning range is achieved with the broadside-coupled configuration, but we also observe a reduction in the amount of rejection by the filter at lower frequencies. This is due to the nature of the coupling required for large shifts in the resonant frequency. The physical explanation for the large tuning range in broadside-coupled split rings can be found by looking at the charge and current distrubtions. The gaps are oriented on opposite sides of the rings, and the current flow on the two rings is in the same direction. Therefore, the electric potentials in the gaps of the two rings are oriented in opposite directions as illustrated in Figure 4.7. What results is an odd-mode type of response where the electric fields between the two rings partially cancel reducing the scattered electric field and allowing some energy to pass through the filter. This effect can also be observed through investigation of the electrical coupling parameter, β, from Equation (4.13). Figure 4.7a shows a plot of the normalized return loss along with the calculated value for β. The negative value for β comes as a result of the charge distributions outlined in Figure 4.7b, and the magnitude of β reveals the amount of electrical coupling between the resonators. The higher the magnitude of β, the more electrical coupling there is between the resonators. Although the magnitude of beta is relatively high for closely spaced resonators, there is destructive interference that allows some energy through the filter. We find that this trend in β corresponds very well to the trend in return loss over the values of Δ_X. Fortunately, even with the reduction in reflection for closely spaced resonators, we still observe more than 11 dB of filtering in the center of the notch band at 3.98 GHz.

The far field patterns for the broadside-coupled rings are also investigated numerically to ensure minimal perturbation outside of the operating frequency of the notch filter. It is found that the patterns are impacted insignificantly outside of the operating band of the filter as indicated by the patterns in Figure 4.8 and the gain in Figure 4.6b. As a result, the filtering element can be placed very close to the throat of the horn antenna for an integrated, compact solution. However, it should be noted that shifting the resonators closer to the throat of the antenna can cause slight shifts in the resonant frequency, and this should be accounted for in the design. Along the same lines, shifting the rings transverse to propagation can also cause shifts in the

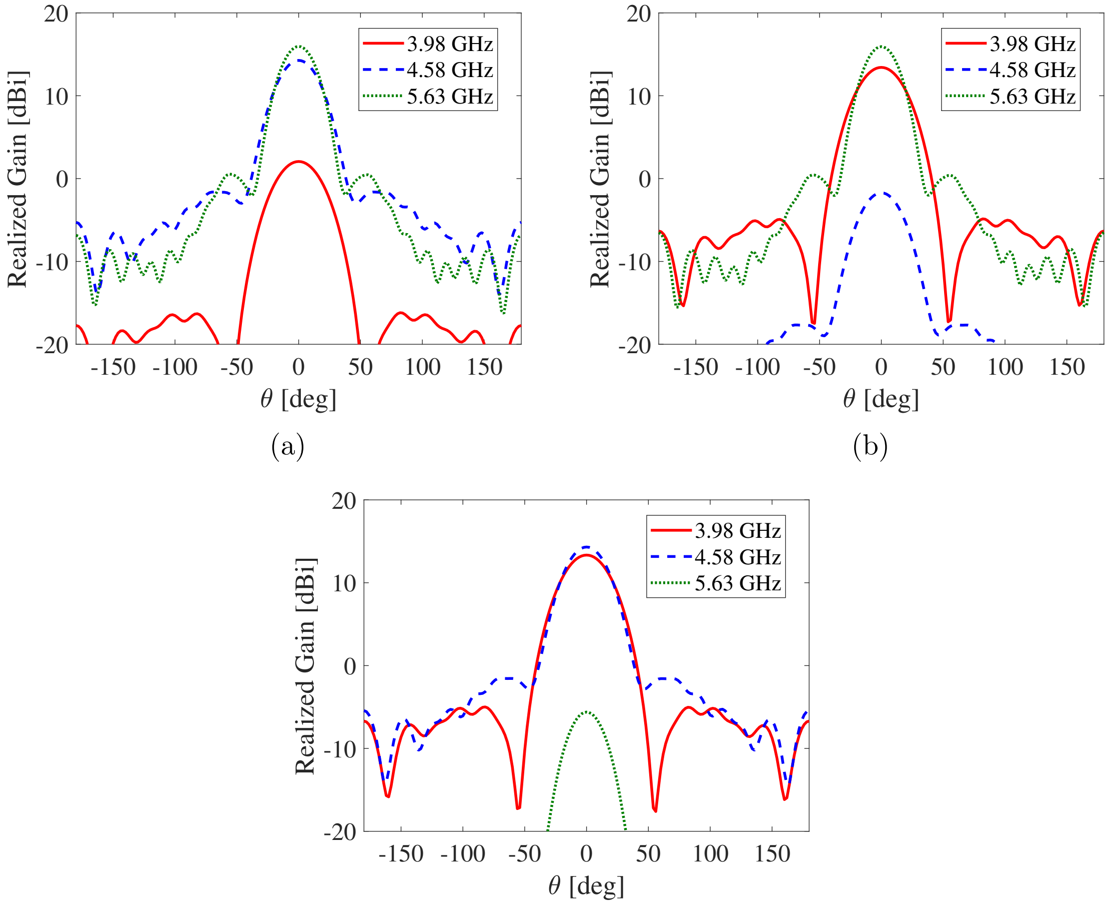

(a)

(b)

(c)

Figure 4.8: Simulated pattern data for the horn antenna integrated with the broadside-coupled ring notch filter. Patterns were plotted at 3.98 GHz, 4.58 GHz, and 5.63 GHz for the three different filtering configurations with $\Delta_x = 0.6$ mm (a), $\Delta_x = 1.25$ mm (b), and $\Delta_x = 6.5$ mm (c).

resonant frequency that should be considered. Placement of the rings off-center in the waveguide along the direction of the **H**-field can further cause less rejection by the filter as the rings are shifted out of the region of the strongest **E**-fields. Movement of the rings out into the throat of the horn also results in less rejection by the filter; however, this could be overcome by redesigning the rings to occupy more physical space inside the throat of the horn.

4.4 Results and Discussion

A proof-of-concept 4G/5G horn antenna with wide tuning range is fabricated with fixed inserts of broadside-coupled split ring resonators to confirm the design approach. The mechanical structure for the horn antenna is 3D printed out of ABS plastic using a Makerbot tabletop 3D printer with design dimensions corresponding to those in Figure 4.3. The inner portions of the antenna are lined with copper foil, and the antenna is bolted together to make electrical contact. The fabricated structure is pictured in Figure 4.9.

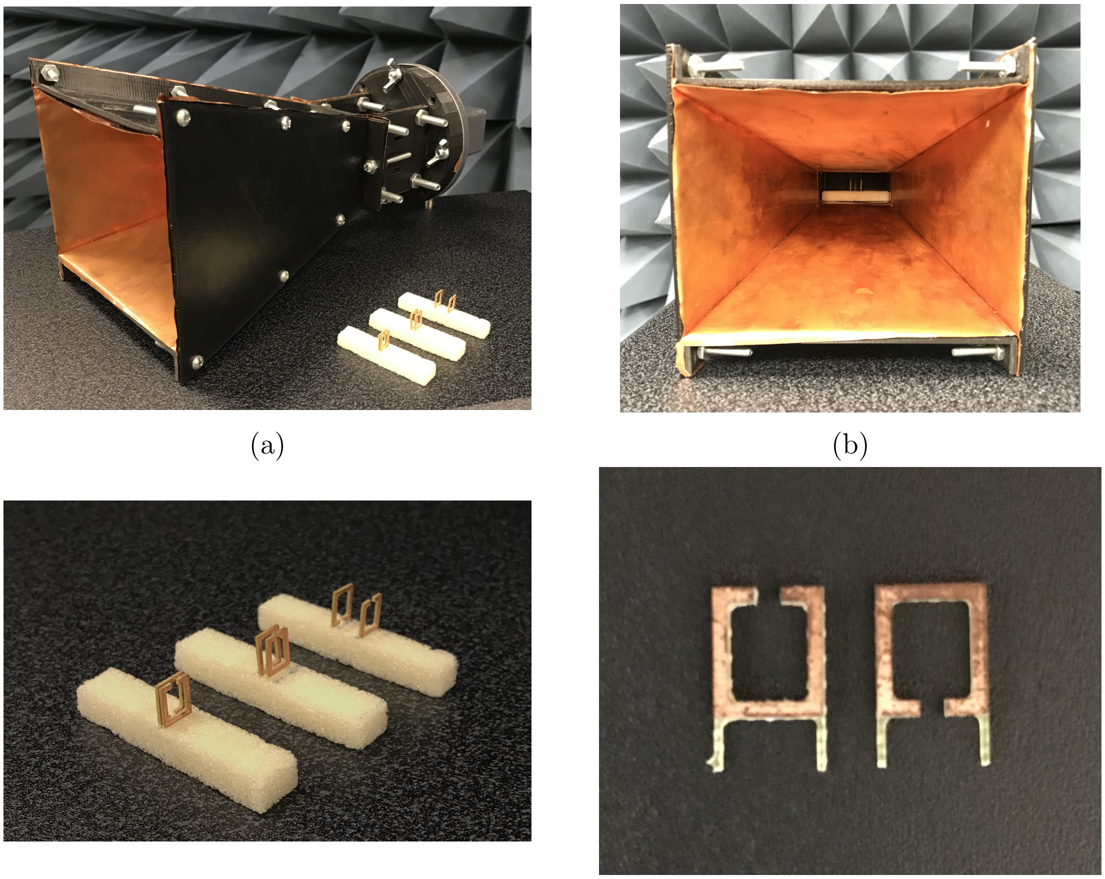

(a) (b)

(c) (d)

Figure 4.9: Isometric view of fabricated horn antenna with coupled resonator filters (a), front view of horn antenna with filter inserted into feed (b), three pairs of SRRs (c), and fabricated split ring resonators (d).

The split rings are milled out of single-sided (1/32)" FR-4 pcb board with 1/2 oz. copper cladding. The rings are milled with dimensions corresponding to those in Figure 4.3a with FR-4 supports left on either side of the ring as shown in Figure 4.9d. The supports are used to position the rings in expanded polystyrene foam as shown in Figure 4.9a where digital calipers are used to help set the appropriate spacing for each pair of resonators. As discussed in the previous section, the rings are spaced at approximately 0.6 mm, 1.25 mm, and 6.5 mm to generate notch bands near 4 GHz, 4.6 GHz, and 5.6 GHz respectively. The FR-4 supports used to position the SRRs does have a small loading effect on the rings which pulls the resonance to slightly lower frequencies.

The return loss and power transmission are measured for the horn antenna with the three filter inserts, and the results are plotted in Figure 4.10 along with the simulated results for comparison. The return loss and power transmission are measured using an Agilent E5071B vector network anlayzer. For the power transmission measurement, a Satimo SH800 standard gain horn is used as a receive antenna for an S_{21} measurement where the transmitted power is extracted. The measured return loss and power transmission agree well with simulated data confirming the design approach and illustrating the wide tuning bandwidth for broadside-coupled split rings. It is found that the horn antenna does not operate quite as low in frequency as indicated by simulations, but this is likely due to small tolerances in the 3D printed structures resulting in a slightly undersized waveguide with a slightly higher cutoff frequency for the dominant TE_{10} mode. Forunately, there is no distinct impact to the filtering as the result of a slightly undersized waveguide. There are very minor shifts in the operating frequencies and 3 dB bandwidths of the three measured filters compared to simulation. The simulated and measured data is compared in Table 4.1. The slight shifts in the resonant frequencies and bandwidths are the result of fabrication and positioning tolerances between the rings. For a production solution, the rings would be precisely positioned using a low loss dielectric foam to ensure repeatability. We also observe less gain reduction for the measured filter in the notch bands compared to simulated results. This could be partly due to slightly less rejection by the fabricated filter as a result of the rings being positioned slightly off-center in the waveguide. Nonetheless, effective filtering is demonstrated, and the design approach is confirmed.

Table 4.1: Simulated vs. measured resonant frequency and bandwidth for three broadside-coupled filter configurations.

	Simulated		**Measured**	
$\boldsymbol{\Delta_X}$	$\boldsymbol{f_r}$	**Bandwidth**	$\boldsymbol{f_r}$	**Bandwidth**
0.6 mm	3.98 GHz	52 MHz	3.99 GHz	44 MHz
1.25 mm	4.58 GHz	81 MHz	4.54 GHz	94 MHz
6.5 mm	5.63 GHz	144 MHz	5.66 GHz	169 MHz

4.5 Conclusion

In this chapter, the Lagrangian formulation for metamaterials is presented as a fast and accurate design approach for guided wave notch filters. Using this approach, many filtering configurations can be investigated in a matter of seconds where full-wave analysis could be computationally intensive and time consuming. The formulation is presented using a fields approach making it suitable for the design of a broad class of guided wave filters based on coupled metamaterials. A 4G/5G horn antenna with integrated notch filter is presented where the filter could be reconfigured to operate over a very wide bandwidth. It is shown that broadside-coupled rings offer much more tunability than gap-coupled rings. The rejection of the filter over the tuning range is also addressed by investigation of the coupled filter electrical response.

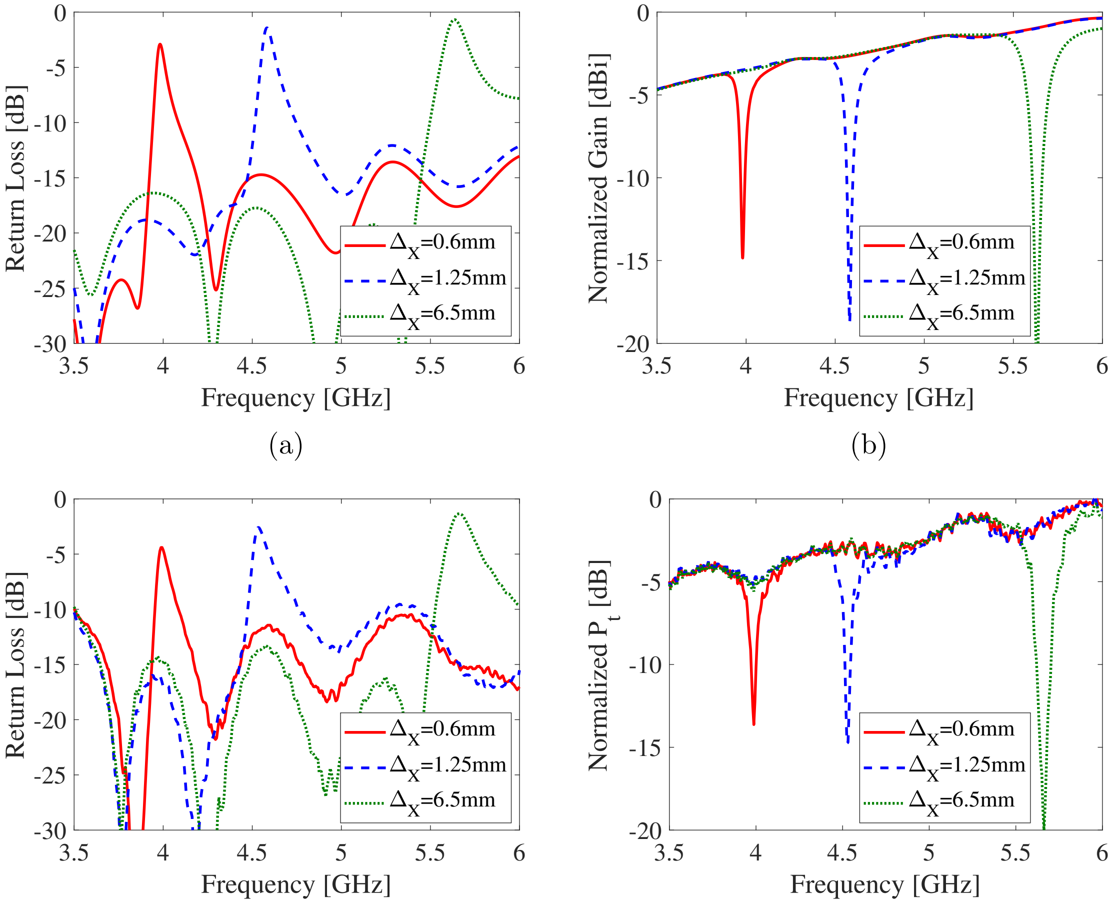

(a) (b)

(c) (d)

Figure 4.10: Simulated and measured return loss (a) and (c) along with simulated normalized gain (b) and measured transmitted power (P_t) (d) for the horn antenna with three fixed filters of broadside-coupled rings with Δ_x set to roughly 0.6 mm, 1.25 mm, and 6.5 mm.

CHAPTER 5: WIDE-BEAM ANTENNA WITH MODULAR RADIATOR FOR BASE STATION APPLICATIONS

5.1 Introduction

One of the greatest challenges facing today's wireless carriers is providing the desired network coverage and capacity in urban environments where the traditional cell approach does not work. The predominant trend to address this challenge is the deployment of distrubuted antenna system (DAS) and small cell antennas where a large number of relatively low-gain antennas are deployed throughout the operating environment [6]. However, it can be difficult to find mounting locations where the antennas integrate unobtrusively into the architecture of the environment. The aesthetics of the antenna are important, and there are zoning restrictions that limit antenna mounting options. Depending on the antenna location and desired coverage area, small cell antennas may also have unique pattern requirements. For example, an antenna mounted to the side of a building requires wide-beam radiation patterns up to 180° for users outside of the building, but the antenna should not radiate into the building. Radiation into the building may create interference between the outdoor base station antenna and an indoor wireless system.

Wide beam antennas are of interest for various applications. Numerous circularly polarized wide-beam antennas have been presented primarily for satellite communication systems [127–132]. Additionally, several wide-beam elements have been proposed for phased array applications where wide beamwidth at the element level enables wide scan capability on the array [133–135]. Other antennas have been presented for wide-beam coverage that are not necessarily tailored to a specific application. Specifically, the authors in [136] present a wide-beam antenna consisting of a monpole attached to a wedge-shaped reflector, a wide-beam dielectric resonator antenna with a high dielectric material is proposed in [137], and the authors of [138] present a wide-beam antenna for large platforms illustrating the antenna mounted to a vehicle.

Increased spectrum availability and usage also creates the potential for base station interference. Fourth generation (4G) Long-Term Evolution (LTE) and the emergence of fifth generation (5G) have introduced bands in the 3.5 GHz and 5-6 GHz range for base station antennas. This enables enhanced data services for mobile users, but this also creates challenges for interference management. Prior to the addition of 3.5 GHz and 5-6 GHz, base station antennas commonly covered frequencies from approximately 690-960 MHz and 1.7-2.7 GHz. Antenna elements and arrays are commonly limited to individual bands for pattern control. Therefore, separate antennas are commonly used to cover disparate frequency bands, and it is desirable to include filtering to limit coupling and interference.

Filtering antennas dedicated to harmonic rejection and mitigation of unwanted radiation higher in frequency than the desired operating band are of interest for interference management. A number of slot antennas are presented where the coupling mechanisms or the slot characteristics provide harmonic rejection [78, 111, 113, 139–141]. Defected ground structures (DGS) are also shown to be an effective technique for eliminating harmonic suppression and are particularly useful for microstrip fed antennas where the DGS can be integrated into the feed line relatively easily [69, 110, 142, 143]. Parasitically coupled antennas are presented in [77, 81] where the characteristics of the coupling structures act as filters to provide harmonic rejection. In two similar approaches, the authors of [77] present a proximity coupled patch antenna with an mushroom electromagnetic bandgap (EBG) structure in the feedline, and the authors of [75] present a capacitively coupled planar inverted-F antenna (PIFA) with split ring resonators (SRRs) etched into the coupling trace. Both antennas operate in the 2.4 GHz range and provide harmonic suppression of at least the 2nd and 3rd harmonics.

This chapter presents a reconfigurable broadband, wide-beam antenna (patent pending) designed to cover a maximum frequency band of approximately 1.7-2.7 GHz for 3G/4G/LTE coverage with an azimuth half-power beamwidth (az-HPBW) between ∼142°-180°. The antenna is comprised of a sleeve monopole, a grounded reflector, and a parasitic director where the main radiator of the sleeve monopole is designed in a modular fashion allowing the antenna to be reconfigured depending on the spectrum requirements of the antenna. Where the broadband antenna can be used for multiple wireless carriers serving as a neutral host, a second main radiator is presented that is optimized for operation from only 1.9-2.4 GHz. This design is useful where spectrum is limited such as instances where a single wireless carrier may be operating over a limited bandwidth. A third main radiator is designed to include a broadband harmonic rejection filter to block potential interference from the 3.5 and 5 GHz bands. The design approach for the filter along with simulated and measured data for various configurations of the wide-beam antenna are presented. Simulated and measured return loss and patterns are also presented for each antenna configuration.

5.2 Wide-Beam Antenna with Modular Main Radiator

5.2.1 Broadband Antenna - Configuration A

The wide-beam antenna presented in this paper is composed of a sleeve monopole, a parasitic director, and a grounded reflector as shown in Fig. 5.1. Three configurations of the antenna are presented in this paper. The broadband configuration (configuration A) is presented first. The foundation of the antenna is the sleeve monopole which has received attention in recent years as a wideband, omnidirectional antenna [cite12]. The sleeve monopole is generally composed of a sleeve, a main radiator, and a ground plane which is realized as a printed circuit board (PCB) in this case. A loading disk PCB is also soldered to the brass main radiator for impedance matching at the lower end of the operating band. The loading disk and the ground PCB are made of 0.762 mm Isola 680 (ϵ_r=3.38, tanδ=0.0035), and the copper cladding includes an immersion tin finish that is assumed to give a total metal thickness of ~0.06 mm. The ground PCB also includes four plated through holes acting as vias to connect solder pads on the top layer to ground on the bottom layer. The brass sleeve is soldered to these pads to provide a ground connection for the sleeve. The antenna is fed through an RG-405 coaxial cable where the outer conductor of the cable is soldered to the bottom side of the ground PCB, and the center pin is fed through a non-plated through hole and soldered to a 5.45-mm diameter feed pad on the top side of the ground PCB. A 10-mm long brass m3 threaded rod is also soldered to the feed pad. This threaded rod enables modularity in the main radiator so that the main radiator may be changed to provide antenna tuning and/or filtering as will be demonstrated later in this paper.

The reflector is used to give the sleeve monopole directionality where the size and position of the reflector can be used to control the azimuth beamwidth. Like the ground PCB and loading disk, the reflector is also made of Isola 680 PCB material where the copper is completely etched away from one side, and the copper side is grounded through the RG-405 coaxial feed cable. The angle, θ_c, and height, H_C, are used primarily for elevation pattern control, and four sheets of Eccosorb MCS RF absorber [144] are placed along the feed cable behind the reflector. The material parameters for the absorber are modeled as ϵ_r=38, tanδ_e=0.01, μ_r=4, and tanδ_m=0.75 for simulations below 3 GHz.

The support structures to hold parts in place are 3D printed ABS from a Fusion 3 FDM 3D printer. The material is characterized from 1.5-6 GHz using an in-house coaxial shorted transmission line test fixture, and the dielectric material properties are extracted. The extracted ϵ_r is between ~2.48-2.5, and the extracted tanδ is between ~0.004-0.008. For simulation purposes, this dissertation assumes the support material to have ϵ_r=2.5 and a loss tangent of tanδ=0.007. L-shaped mounting brackets and the

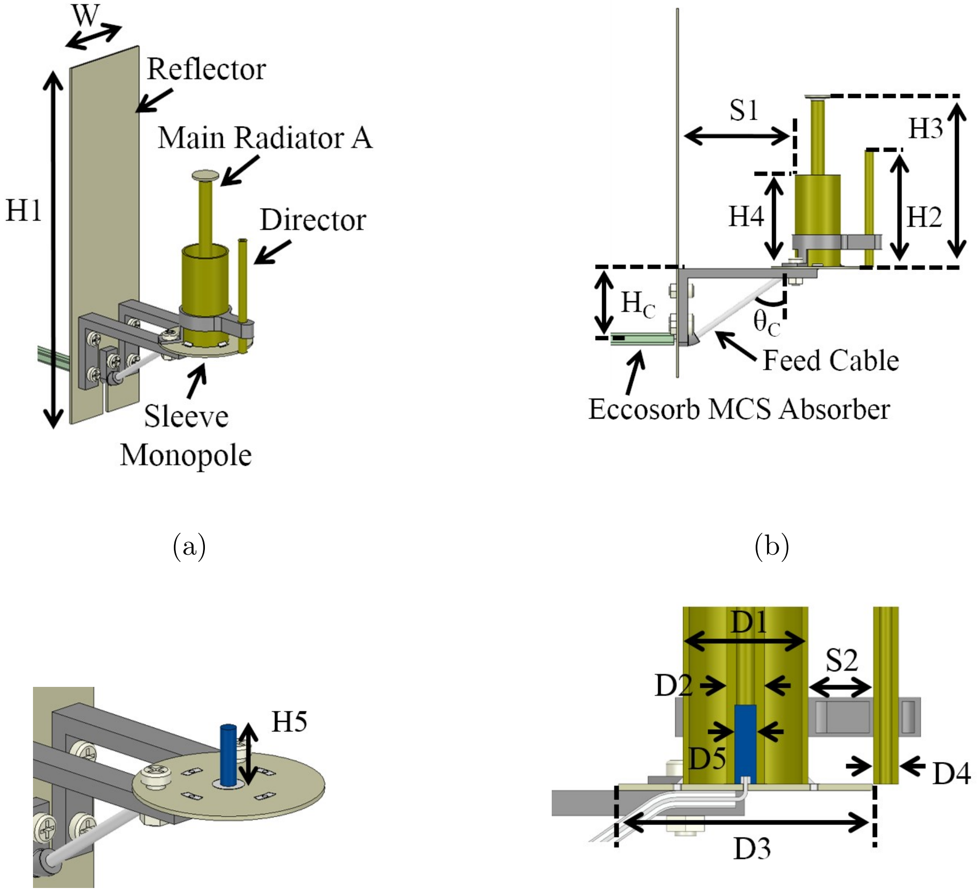

(a) (b)

(c) (d)

Figure 5.1: Antenna configuration A isometric view (a), side view (b), threaded rod placement (c), and split view (d).

support holding the director in place are 3D printed with wall thicknesses between ∼0.5-0.8mm and a 5% infill so that these structures are essentially hollow. This minimizes the impact of the dielectric properties on the antenna performance. The nuts and bolts used to secure the support structures are plastic with modeled dielectric properties of ϵ_r=2.8 and tanδ=0.018 based on dielectric material measurements using the coaxial shorted test fixture mentioned above.

5.2.1.1 Benefit of the Parasitic Director

To illustrate the benefit of the director, antenna A is compared to a wide-beam antenna without a director in Fig. 5.2. Note that the wide-beam antenna without the director is also designed to provide a peak az-HPBW of ∼180° with an acceptable impedance match where return loss is better than 10 dB from ∼1.68-2.76 GHz. In some cases, base station antennas are mechanically tilted to avoid interference with neighboring sites or improve service for users in a particular coverage area. Therefore, it is desirable to minimize antenna pattern variation over frequency. Without the director, the ϕ=0° -10-dB crossover (the point where the elevation pattern is reduced to 10 dB below its peak value) varies from an elevation angle of $\theta \simeq$33° at 1.7 GHz to an elevation angle of $\theta \simeq$58° at 2.7 GHz. This amount of variation may be unacceptable for situations where the antenna is mechanically tilted. On the other hand, the presence of the director is found to improve the -10-dB crossover variation from an elevation angle of $\theta \simeq$35° at 1.7 GHz to and elevation angle of $\theta \simeq$44° at 2.7 GHz.

The director is also found to reduce the variation in azimuth beamwidth for the antenna. The az-HPBW for the antenna without the director varies from ∼124° to ∼180°, and the az-HPBW for the antenna with the director varies from ∼144° to ∼180°. Note that the presence of the director requires some dimensional variation in the antenna design, but this also provides the benefit of an additional tuning feature for the antenna.

5.2.1.2 Input Match Parametric Study

The nominal dimensions for antenna configuration A are listed in Table 5.1. The sleeve height and main radiator height are used to fine tune the antenna match at the upper and lower ends of the operating band. A parametric study on the impacts of the sleeve height and main radiator height are presented in Fig. 5.3 where it is apparent that the main radiator height can be used primarily for adjustment at the lower part of the operating band, and the sleeve height can be used primarily for adjustment at the upper part of the operating band. Notice that both parameters also impact the match over the central part of the operating band. For this anlaysis,

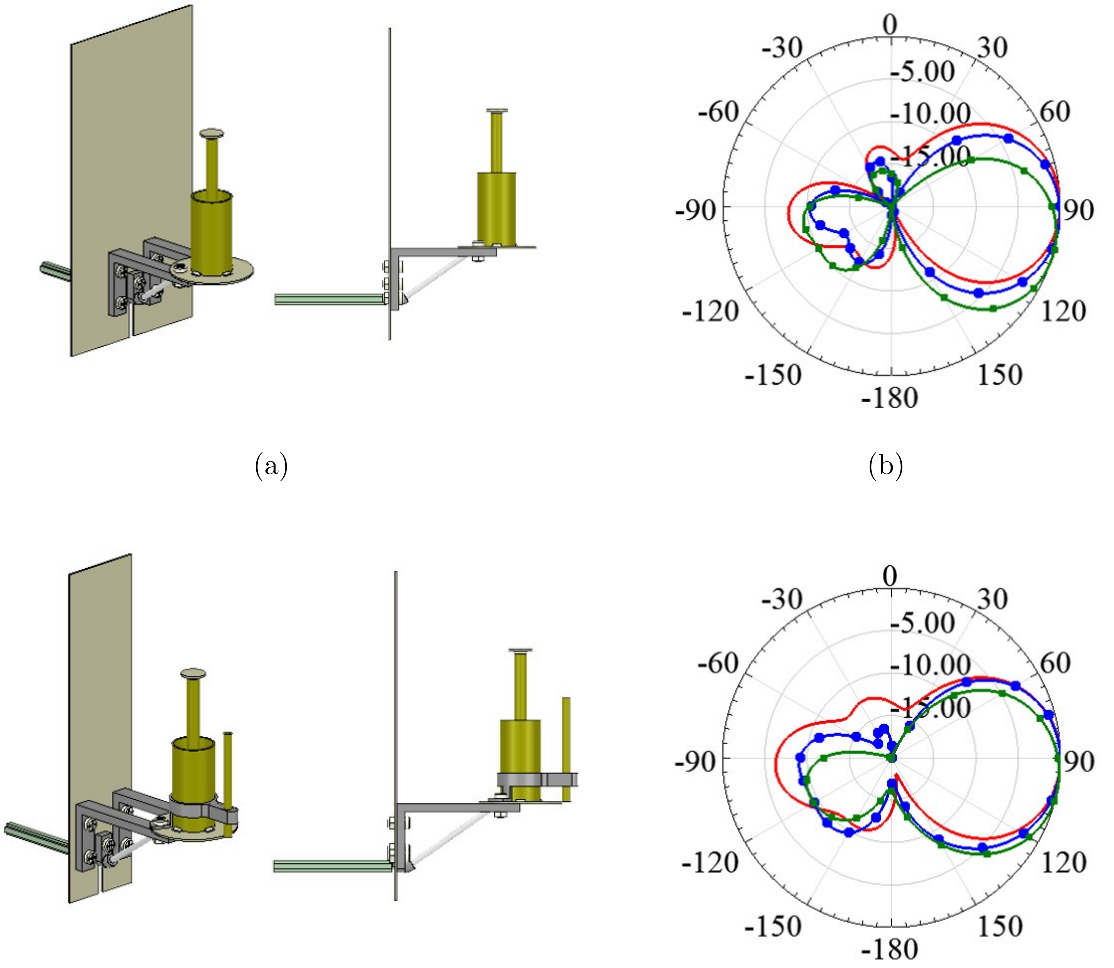

(a) (b)

(c) (d)

Figure 5.2: Antenna with no director (a) and its elevation patterns at ϕ=90° (b) vs. antenna with director (c) and its elevation patterns at ϕ=90° (d).

the antenna is set to the nominal design variables listed in Table 5.1 aside from the variable under investigation.

5.2.2 Narrow Band Antenna with Modified Main Radiator - Configuration B

The previous section presents a modular main radiator where a threaded rod is used as a means to change the main radiator and reconfigure the antenna performance. This feature can be used to tune the antenna for specific frequency bands. For instance, the antenna could be used as a neutral host where different wireless carriers

Table 5.1: Nominal design values for antenna configuration A

Variable	**mm**	**Variable**	**mm**	**Variable**	**mm/deg**
W	31.75	H5	10	D3	31.75
H1	127	S1	40.1	D4	3.175
H2	40	S2	8.3	D5	2.75
H3	58.2	D1	15.875	θ_C [deg]	55
H4	31.7	D2	4.7625	H_C	23.2

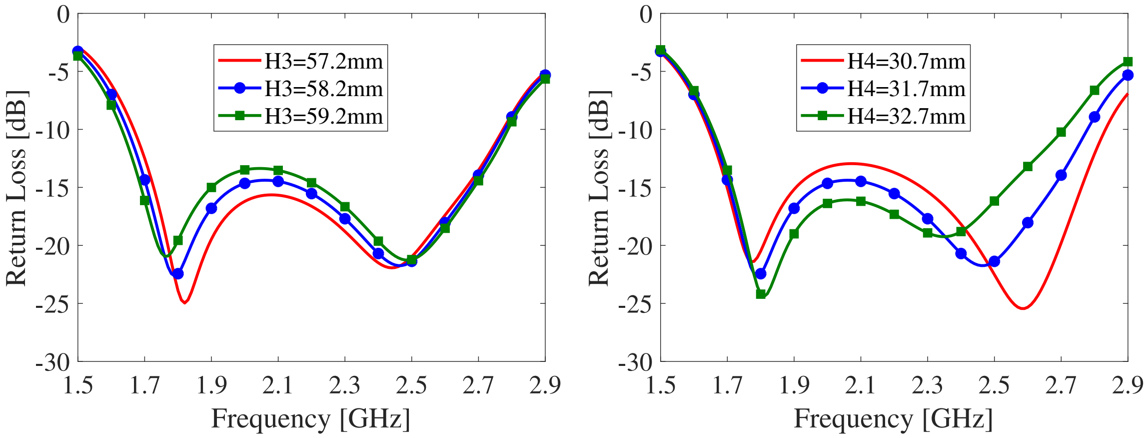

(a) (b)

Figure 5.3: Effects of main radiator height, H3, (a) and sleeve height, H4, (b) on the impedance match for antenna configuration A.

that have different operating bands use the same antenna. In this case, the antenna may need to cover the full spectrum from 1.7-2.7 GHz. However, in some cases, the antenna might only serve a single carrier requiring limited bandwidth. In this case, it is desirable that the antenna is optimized for the required bandwidth with disregard for other bands that are not used.

Here, a main radiator is designed to provide excellent return loss (better than 22 dB) from 1.9-2.4 GHz while sacrificing performance from 1.7-1.9 GHz and 2.4-2.7 GHz. This way, reflections are minimized in the desired operating band and the overall antenna system can be optimized for a single wireless carrier. This configuration is referred to as antenna configuration B. The main radiator is shortened, and a

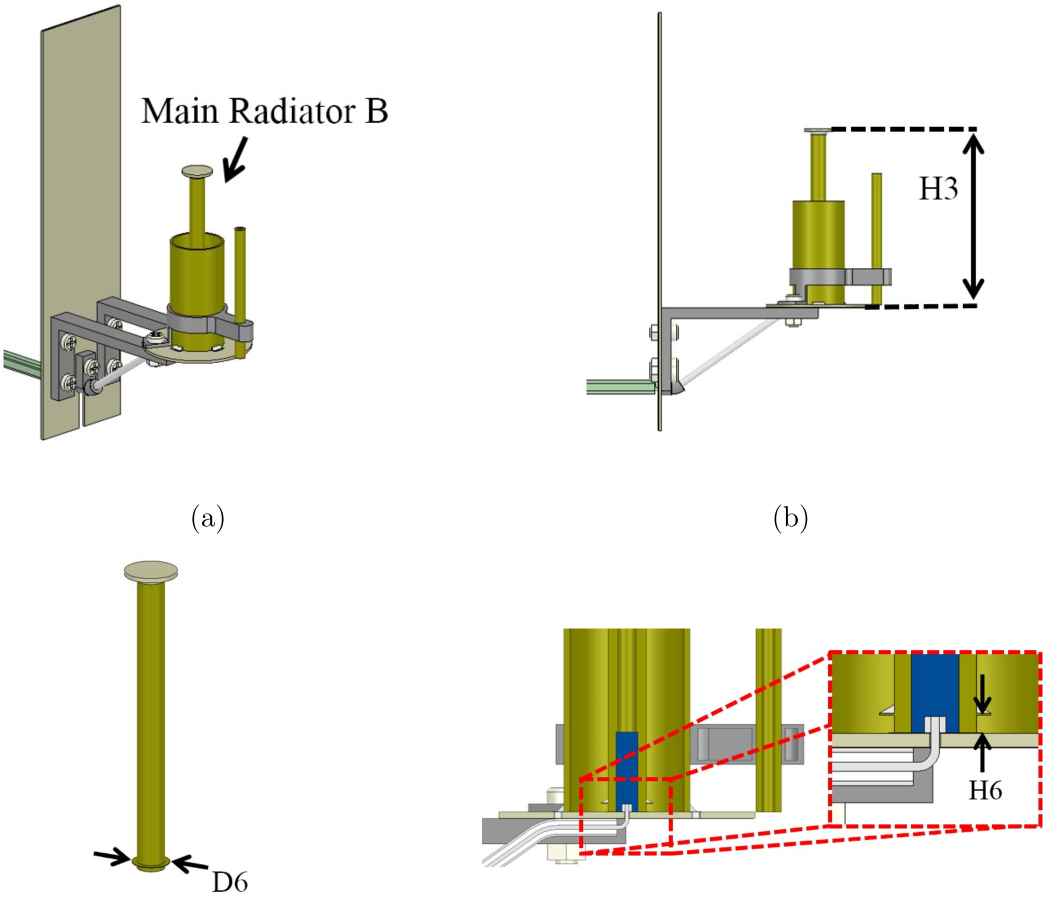

(a) (b)

(c) (d)

Figure 5.4: Antenna configuration B isometric view (a), side view (b), main radiator (c), and split view (d).

capacitive disk is added to the main radiator as shown in Fig. 5.4 with dimensions listed in Table 5.2. This disk is punched from a sheet of 0.127-mm brass foil and soldered to the main radiator, but the entire structure could be machined from a solid piece of brass. Other than the dimensions listed in Table 5.2, the antenna dimensions match those listed in Table 5.1 for antenn A. Note that the antenna can be tuned to cover various portions of the operating band with modification of the main radiator and/or dielectric loading in the sleeve.

5.2.2.1 Input Match Parametric Study

With the sleeve height fixed and the main radiator height reduced to 52.9 mm, the effects of the capacitive disk on the input match are investigated here. The nominal design values are listed in Table 5.2. Figure 5.5 indicates that the size and offset of the capacitive disk can be used to adjust the upper end of the operating band. Without the capacitive disk, the return loss exhibits a deep null near 1.9 GHz, but the return loss is degraded near 2.4 GHz. This is implied by Fig. 5.5 where reducing the diameter D6 or increasing the height H6 degrades the match near 2.4 GHz. Alternatively, increasing the diameter D6 or reducing the height H6 increases the capacitance near the base of the main radiator. This provides a better match near 2.4 GHz and provides slightly more bandwidth, but it also degrades the match in the center of the band.

Table 5.2: Nominal design values for antenna configuration B.

Variable	**mm**	**Variable**	**mm**	**Variable**	**mm**
H3	52.9	D6	6.4975	H6	1

Note that other techniques such as dielectric loading, metallic loading, or machining the main radiator can be used to tune the antenna over various sub bands. These techniques may also be used to provide sharper roll-off in the return loss for filtering effects.

5.2.3 Integrated Bandstop Filter for Harmonic Rejection - Configuration C

As mentioned previously, the wireless industry has seen the introduction of new operating bands in recent years, and there will continue to be the addition of services within these and other bands that make interference problematic. This antenna, as with most other antennas, suffers from higher order harmonics where the antenna can radiate effectively at frequncies higher than the intended operating frequency.

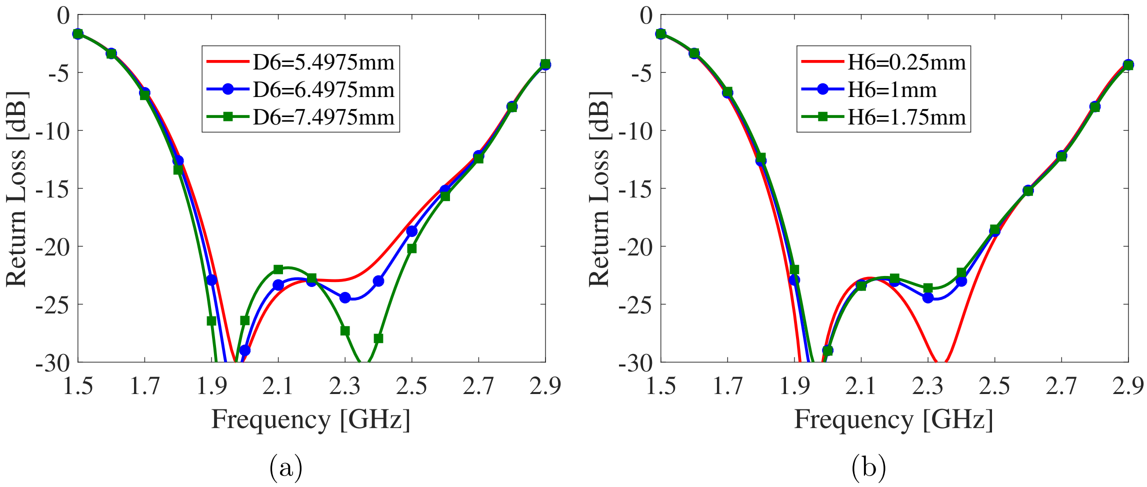

Figure 5.5: Effects of capacitive disk radius, D6, (a) and height, H6, (b) on impedance match for antenna configuration B

Unfortunately, the second and third harmonics fall within the 3-6 GHz range which could cause interference with newly deployed base station systems, and there is a need for filtering. The sleeve monopole with an integrated broadband stop filter for an FiA approach is presented in [145]. That work is extended here with a discussion of the equivalent circuit model and an investigation of bandwidth enhancement with parallel resonators. The approach in this paper also configures the filter so that the only modifications to the unfiltered antenna involves modification of the center conductor requiring no additional volume over the unfiltered antenna. In configuring the antenna this way, the main radiator can be configured as a module, and filtering can be added by simply swapping out the main radiator module. Practical realization of a filter support structure and impedance matching in the presence of the filter are also considered.

The filtered wide-beam antenna (antenna configuration C) is pictured in Fig. 5.6 where the dimensions of the antenna aside from the main radiator match those listed in previous sections. For clarity, the main radiator is shown in Fig. 5.6c, and the main radiator with the filter elements and the filter support/matching structure are shown in Fig. 5.6d. The associated dimensions for antenna C are listed in Table

5.3. The support structure in this case is 3D printed using the same ABS material used to print the antenna supports. However, the filter support structure is printed with 100% fill so that the structure is essentially a solid material with the dielectric properties discussed in Section 5.2. The particular shape and configuration of the filter elements and the support structure are described in the following sections.

Table 5.3: Nominal design values for antenna configuration C.

Variable	**mm**	**Variable**	**mm**	**Variable**	**mm**
H3	57.5	H8	17	D7	3.175
H7	19	H9	12.64	D8	9.1625

5.2.3.1 Stop Band Enhancement with Parallel Resonators

The filter element used in this paper is based on the capacitively loaded strip (CLS) structure which is relatively common in metamaterial applications [50]. One advantage of the CLS, and the reason it is used in this paper, is the fact that it can achieve relatively broad bandwidths. For the initial analysis, the CLS filter structure is modeled in a coaxial fixture as pictured in Fig. 5.7 with the dimensions matching those of the bottom section of the sleeve monopole antenna. The filter element pictured in Fig. 5.7c is composed of two capacitive strips connected by an inductive trace. The element is realized on 0.762-mm thick Isola IS680 which is the same board material as the other PCB components of this antenna. Note that the capacitive strips are realized using the top and bottom of the PCB where plated through holes connect identical traces on the top and bottom of the board. This is done to increase capacitance between the filter element and the sleeve/main radiator. This reduces the height of the filter element and provides more space for the impedance matching section discussed in the next section.

We find that a series capacitor-inductor-capacitor model shown in Fig. 5.8 provides a reasonable approximation to the performance of the filter structure. Note that a

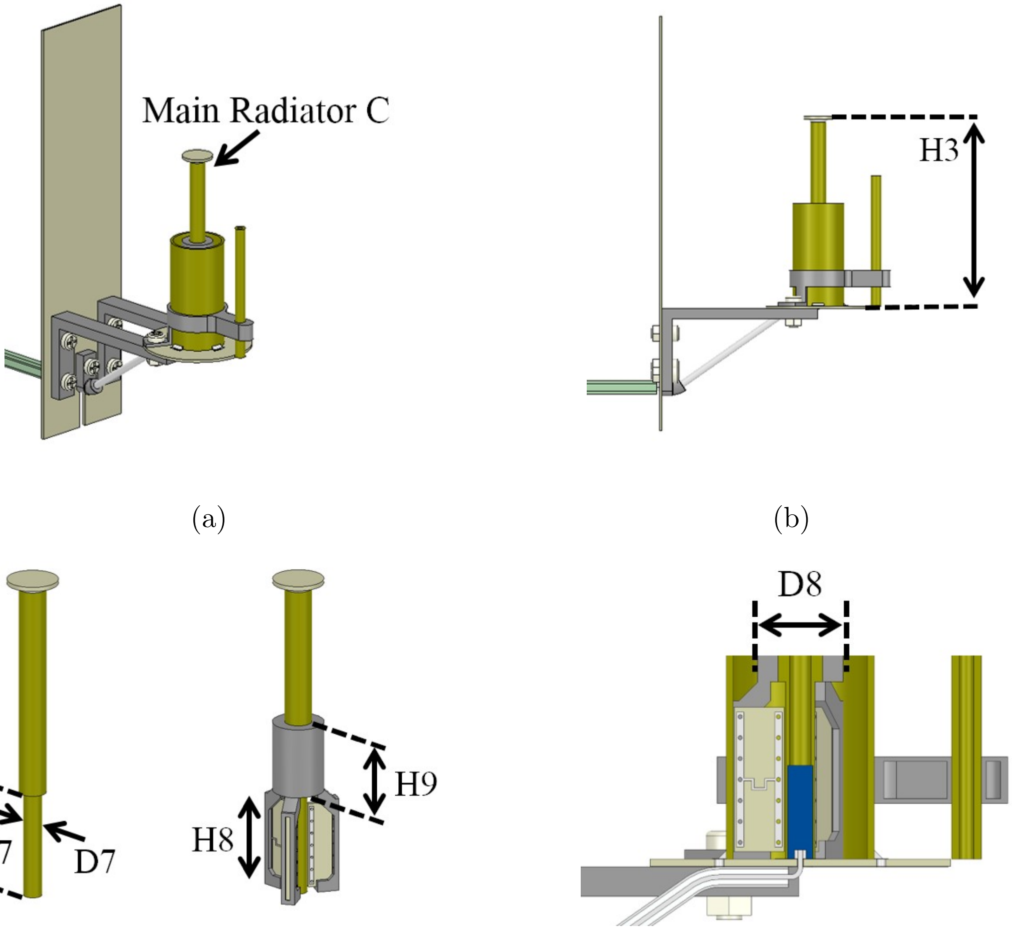

(a) (b)

(c) (d) (e)

Figure 5.6: Antenna configuration C isometric view (a), side view (b), main radiator (c), main radiator with filter elements and filter support (d), and split view (e).

filter support structure is included in the coaxial fixture analysis to capture the effects of this structure on the filter performance, and the dimensions shown in Fig. 5.7 are listed in Table 5.4.

Using the circuit model in Fig. 5.8, the admittance for the filter structure is calculated as

$$Y = N\frac{j\omega C_p}{1-\omega^2 L_p C_p} \tag{5.1}$$

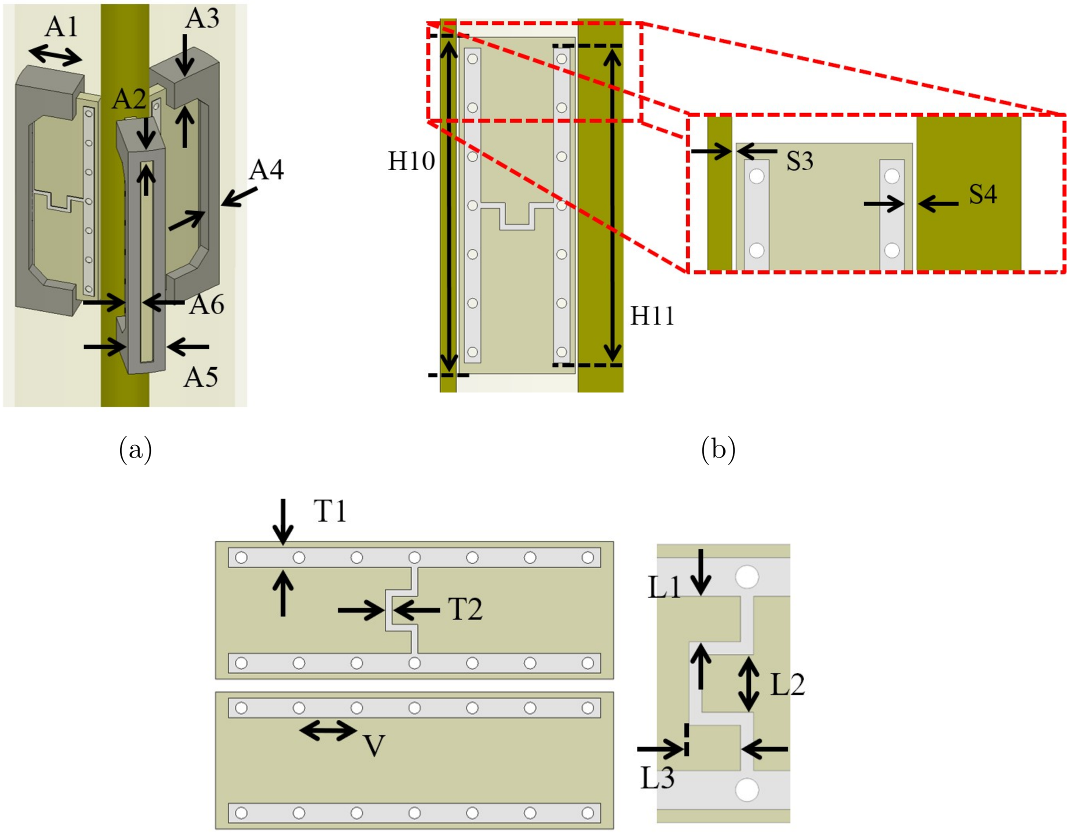

(a)

(b)

(c)

Figure 5.7: Antenna configuration C filter design approach showing coaxial fixture for analysis (a) and filter element spacing relative to walls (b). A detailed view of filter element is also shown in (c) representing the top side (top left), bottom side (bottom left), and the inductive strip (right).

where

$$C_p = \frac{C_{1p}C_{2p}}{C_{1p}+C_{2p}}. \tag{5.2}$$

and the value of N corresponds to the number of filter elements. If N, L_p, and C_p are known, the S-parameters for the structure can be calculated as [53]

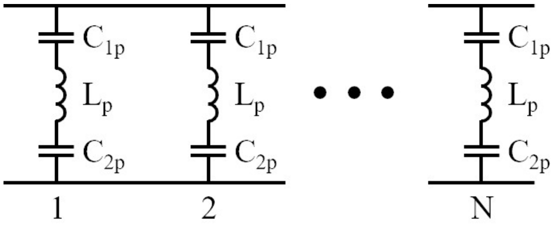

Figure 5.8: Equivalent circuit model to describe CLS filter performance vs. frequency.

$$S_{11} = \frac{-j\omega N C_p Z_0}{2 - 2\omega^2 L_p C_p + j\omega N C_p Z_0} \tag{5.3}$$

$$S_{21} = \frac{2 - 2\omega^2 L_p C_p}{2 - 2\omega^2 L_p C_p + j\omega N C_p Z_0} \tag{5.4}$$

To obtain the equivalent circuit L and C values, the structure of Fig. 5.7 is simulated in HFSS and the S-parameters are exported for processing. From here, a genetic algorithm (GA) is used to iteratively find the L_p and C_p that fit the simulated data [146, 147]. Table 5.5 lists the extracted circuit L_p and C_p for N=1, 2, 3, and 4 fitler elements, and Fig. 5.9 plots the calculated vs. simulated S-parameters for N=1 and 4 filter elements where the calculated S-parameters are obtained using Eqns. 5.3 and 5.4 and the extracted L_P and C_p values of Table 5.5.

The bandwidth is increased by increasing the number of filter elements, but there is also a corresponding frequency shift in the resonance. This is due to the modification of equivalent L_p and C_p values with increasing N as indicated in Table 5.5. The reduction in C_p is physically the result of coupling between the filter structures where a perfect-**H** boundary is generated between each filter element. There is a stronger overall interaction between the filter(s) and the incident fields with increasing N leading to the bandwidth enhancement, but there is a weaker individual interaction between each filter element and the incident fields indicated in Fig. 5.10. Thus, the

Table 5.4: Design values for configuration C filter elements and support structure used for filter analysis. Note that the outer section of the fitler support structure is designed to conform to the inner contour of the sleeve causing A4 to vary from ∼0.9-1 mm.

Variable	**mm**	**Variable**	**mm**	**Variable**	**mm**
A1	4	H10	15.5	V	2.25
A2	0.8	H11	14.5	L1	0.875
A3	2	S3	0.125	L2	1.11
A4	0.9-1	S4	0.375	L3	1
A5	2.482	T1	0.75		
A6	0.8	T2	0.25		

individual capacitance values are effectively decreased. On the other hand, there is a point where the equivalent L_p values begin to increase slightly. This is because the magnetic fields are perpendicular to the perfect-**H** boundary, and the proximity of neighboring filter elements causes the fields to interact in a way that enhances the filter response to the incident magnetic field.

Table 5.5: Extracted capacitance and inductance for CLS filter with N=1, 2, 3, and 4 filter elements.

N	**Capacitance (pF)**	**Inductance (nH)**
1	0.308	7.57
2	0.292	7.13
3	0.276	6.99
4	0.256	7.08

5.2.3.2 Impedance Matching with Filter

The primary challenge with the filtered antenna is matching the antenna in the presence of the filter. It is well known that resonant metamaterials exhibit a region where the effective relative permittivity, ϵ_{e_r}, or effective relative permeability, μ_{e_r}, is >1 prior to resonance. The CLS filter structure proposed herein exhibits this response

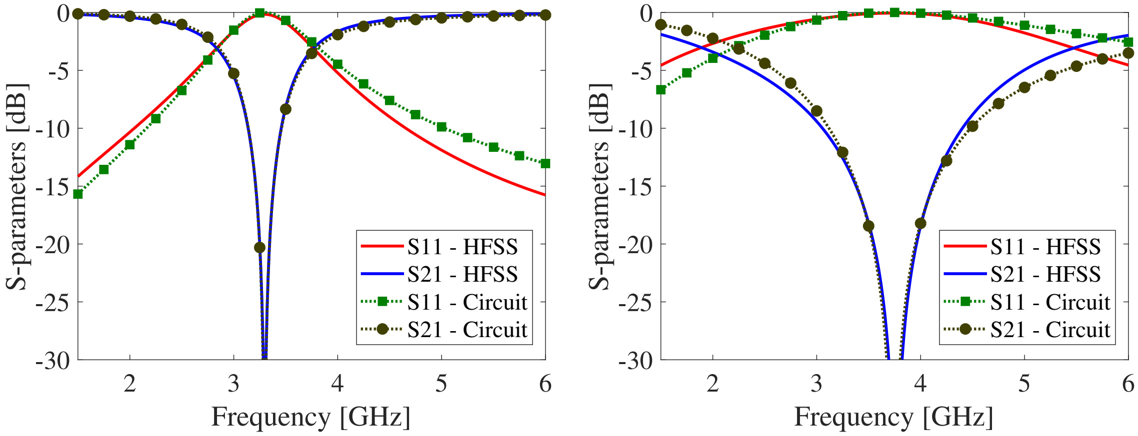

(a) (b)

Figure 5.9: S-parameters for HFSS simulated test fixture shown in Fig. 5.7 along with S-parameters calculated from equivalent circuit L and C values in Table 5.5 for N=1 filter element (a) and N=4 filter elements (b). The coaxial fixture has characteristic impedance $Z_0 \simeq 91\Omega$ for this analysis.

below resonance requiring compensation to maintain a desirable impedance match to the antenna. Part of this compensation is a reduced diameter on the main radiator in the vicinity of the filter elements as shown in Fig. 5.6c, but this does not provide a good impedance match to the antenna without additional compensation.

The additional compensation is realized as an impedance matching section at the top of the filter support where the diameter, D8, is used to load the antenna and provide impedance matching in the presence of the filter. Parametric analysis of the filter matching structure is shown in Fig. 5.11 where the matching structure directly impacts the central and upper frequency portions of the operating band. A reduction in the height, H9, or diameter, D8, degrades the match over the central part of the operating band while improving the match at the higher end of the operating band. On the other hand, an increase in the height, H9, or diameter, D8, improves the match over the central part of the operating band while degrading the match at the upper end of the operating band. Note that the more filter elements used, the higher the effective permittivity in the desired operating band. Therefore, there is a balance in the filter bandwidth/rejection and the impedance match. For this paper, three filter

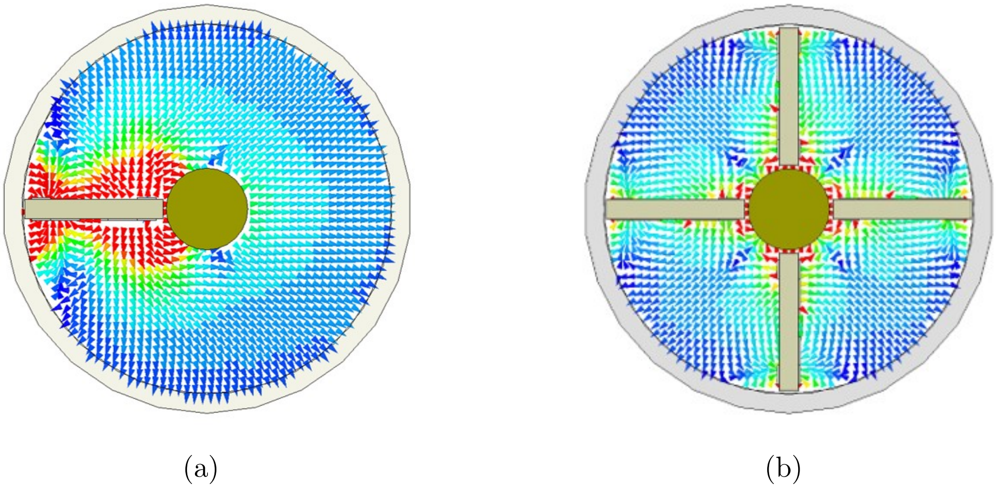

Figure 5.10: Electric field structure in coaxial fixture of Fig. 5.7 for N=1 filter element (a) and N=4 filter elements (b). Both plots have a scale of 0-4 kV/m for the **E**-field data.

elements are found to provide sufficient filtering while allowing the desired impedance match.

5.3 Pattern Parametric Study

A parametric study of the radiation patterns is presented here. The effects studied in this analysis apply to all three configurations presented above, but the analysis is conducted using configuration A since it is the most general configuration. The reflector width and separation can be used to control azimuth beamwidth, and their impacts are shown in Fig. 5.12.

The simulated azimuth beamwidths at 2.2 GHz are compared for reflector widths of 21.75mm, 31.75mm, and 41.75mm mm in Fig. 5.12a where it is shown that variations of up to 20 mm in the reflector width do not have signficant impacts on the azimuth patterns. The az-HPBW only varies from ∼184° with W=21.75mm to ∼172° with W=41.75mm. The reflector spacing has a more significant impact on the azimuth beamwidths as indicated in Fig. 5.12b where the simulated azimuth beamwidths at 2.2 GHz are compared for reflector spacings of 35.1mm, 40.1mm, and 45.1mm. The az-HPBW varies from ∼162° with S1=35.1mm to ∼194° with S1=45.1mm. Increasing

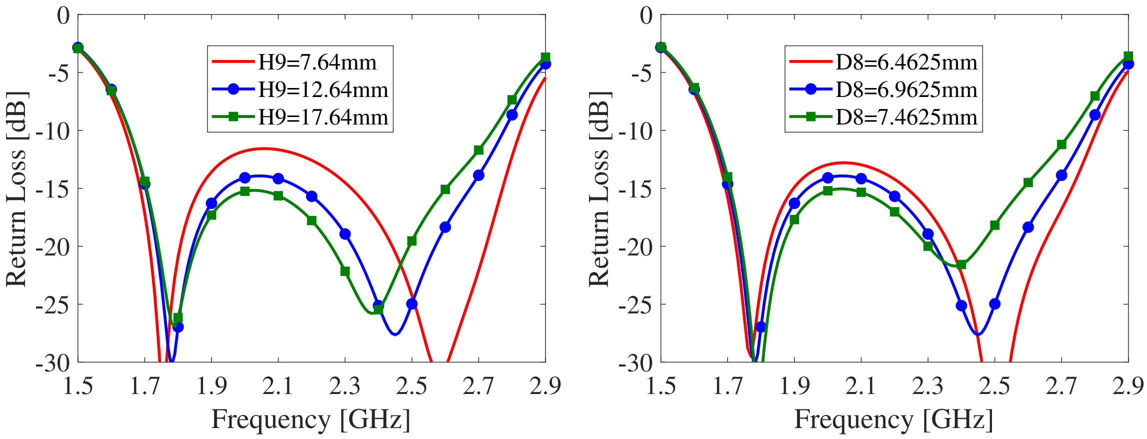

(a) (b)

Figure 5.11: Parametric study for return loss variation with changes in filter support matching section height, H9, (a) and diameter, D8, (b) for antenna configuration C.

the reflector height can provide a deeper null at the lower part of the operating band and improve the spread on the 10-dB crossover angle, but this comes at the expense of increased antenna height. For this paper, the reflector height is chosen to be 127 mm. Note that the azimuth patterns shown in Figs. 5.12a and 5.12b are plotted through the peak of the main beam. For W=21.75 mm, W=31.75 mm, and W=41.75 mm, the azimuth patterns are plotted at θ=91°, θ=93°, and θ=94°, respectively. For S1=35.1 mm, S1=40.1 mm, and S1=45.1 mm, the azimuth patterns are plotted at θ=91°, θ=93°, and θ=95°, respectively.

The impacts of the director and feed cable on the elevation pattern are investigated in Figs. 5.13-5.15. The antenna presented in this paper is designed primarily for wide azimuth beamwidth, but elevation pattern control is not trivial. Where the azimuth patterns are determined largely by the reflector configuration, the elevation pattern performance is determined by the parasitic director, feed cable, and the overall geometry of the sleeve monopole. Figure 5.13 shows the impact of the director length, H2. By design, the director length has little impact on the patterns at 1.7 GHz, but it can have a significant impact on the elevation patterns at 2.7 GHz as shown in Fig. 5.13b. A director length of 45 mm significantly reduces squint in elevation, but it

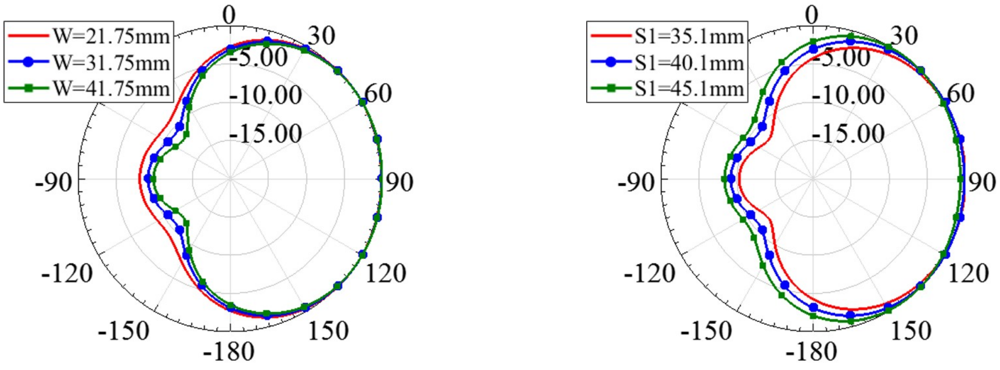

(a) (b)

Figure 5.12: Effects of reflector width, W, (a) and separation, S1, (b) on azimuth patterns at 2.2 GHz.

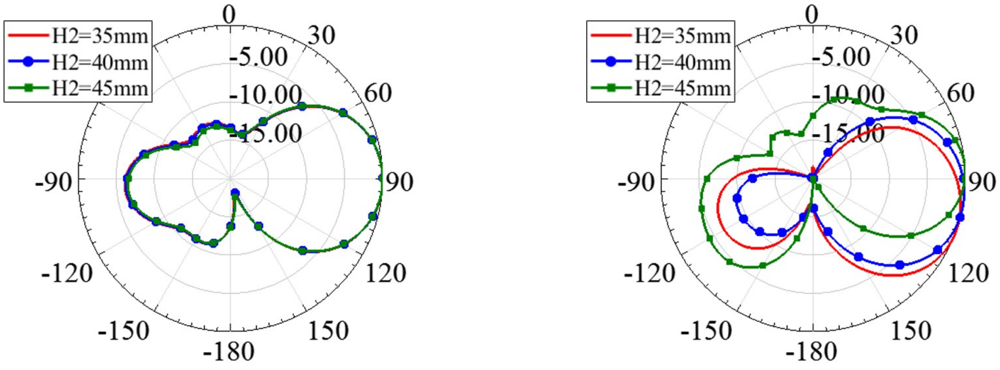

(a) (b)

Figure 5.13: Effects of director length (H2) on elevation patterns (ϕ=0°) at 1.7 GHz (a) and 2.7 GHz (b).

also creates additional unwanted radiation above the main beam. On the other hand, a director length of 35 mm does not provide the desired improvement in elevation pattern performance where the 10-dB crossover is $\sim$51° at ϕ=0°.

The impacts of the director spacing are shown in Fig. 5.14. Similar to the director length, the director spacing has little impact on the patterns at 1.7 GHz, but this spacing can have a dramatic impact on the patterns at 2.7 GHz. Placing the director too close can significantly degrade the elevation pattern shape as indicated in Fig. 5.14b where a large amount of radiation is pushed upward above the main beam.

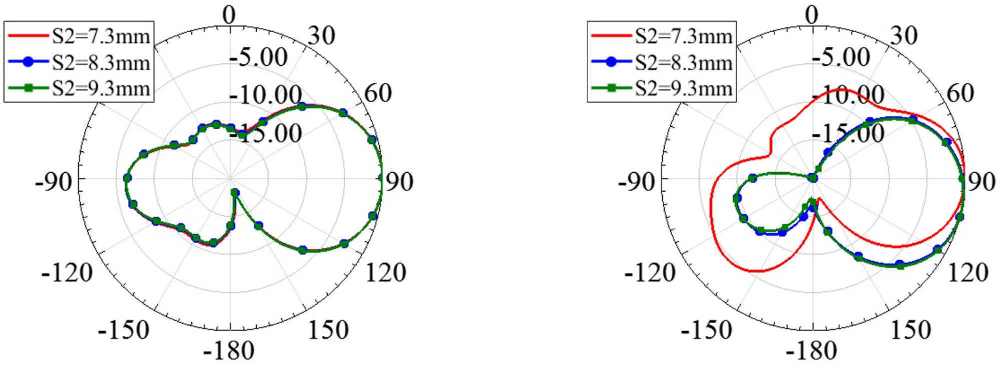

(a) (b)

Figure 5.14: Effects of director separation (S2) on elevation patterns (ϕ=0°) at 1.7 GHz (a) and 2.7 GHz (b).

However, moving the director in the other direction away from the sleeve does not have a tremendous impact on the elevation patterns. The biggest issue here is that the director loses its impact as it is moved further and further from the sleeve.

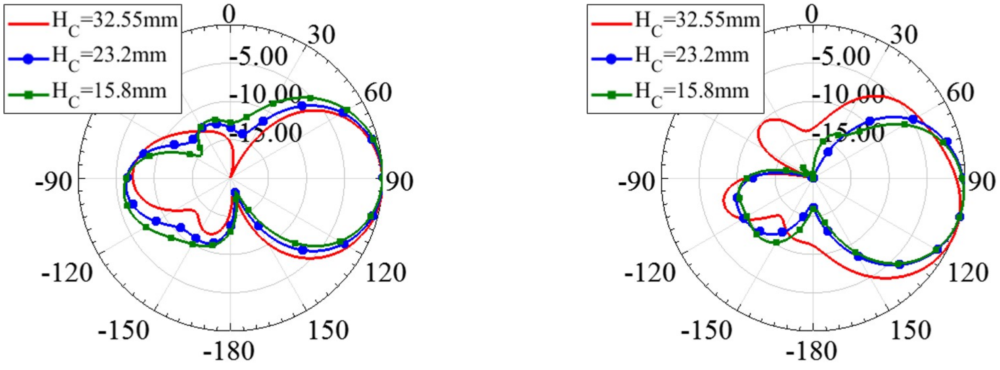

(a) (b)

Figure 5.15: Effects of cable angle, H_C, on elevation patterns (ϕ=0°) at 1.7 GHz (a) and 2.7 GHz (b). Note that $\theta_C = 45°$ for $H_C = 32.55$ mm, $\theta_C = 55°$ for $H_C = 23.2$ mm, and $\theta_C = 65°$ for $H_C = 15.8$ mm.

The impacts of the cable angle, θ_C, and height, H_C, are shown in Fig. 5.15 where it is demonstrated that these parameters impact the elevation pattern performance over the entire operating band. This is due to currents that flow along the outer jacket of the feed cable where these currents are used to help control elevation patterns for this antenna. Notice that a cable angle and height of 45° and 32.55 mm provides a very deep null in the elevation pattern at 1.7 GHz, but gives significant pattern distortion at 2.7 GHz. A cable angle and height of 65° and 15.8 mm has less impact on the overall patterns, but it increases the variation between the 10-dB crossover points which is not desirable. Note that the variations investigated for the pattern parametric study also have impacts on the peak gain and impedance match to the antenna. These impacts are not shown as part of this parametric study, but they should be considered in the antenna design. It is important to note that $\mathrm{H_C}$ is more critical than θ_C and has a much larger impact on the overall pattern performance.

5.4 Results and Discussion

5.4.1 Simulated and Measured Results - Configuration A

A prototype configuration A antenna is fabricated and pictured in Fig. 5.16. Simulated and measured return loss for the wide-beam antenna is pictured in Fig. 5.16e where good agreement is shown between simulation and measurement. Measurements are taken with an Agilent E5071B network analyzer.

Measurements indicate a 10-dB return loss from ∼1.64-2.76 GHz covering 3G/4G/LTE frequencies. The simulated and measured gain and azimuth beamwidth are pictured in Fig. 5.17 where good agreement is observed between measured and simulated data. The radiation patterns are measured in an MVG SG 64 near-field range. The antenna exhibits measured peak gain between ∼4.38-5.87 dBi, and the measured az-HPBW is between ∼142°-182°. Note that the az-HPBW is measured through the peak of the main beam.

The simulated and measured normalized radiation patterns are pictured in Fig. 5.18. Very good agreement is obtained between simulated and measured patterns where wide azimuth beamwidth is demonstrated. Also note that the antenna provides very good cross-polarization. The variations between simulation and measurement are likely due to manufacturing and assembly tolerances as well as range setup for

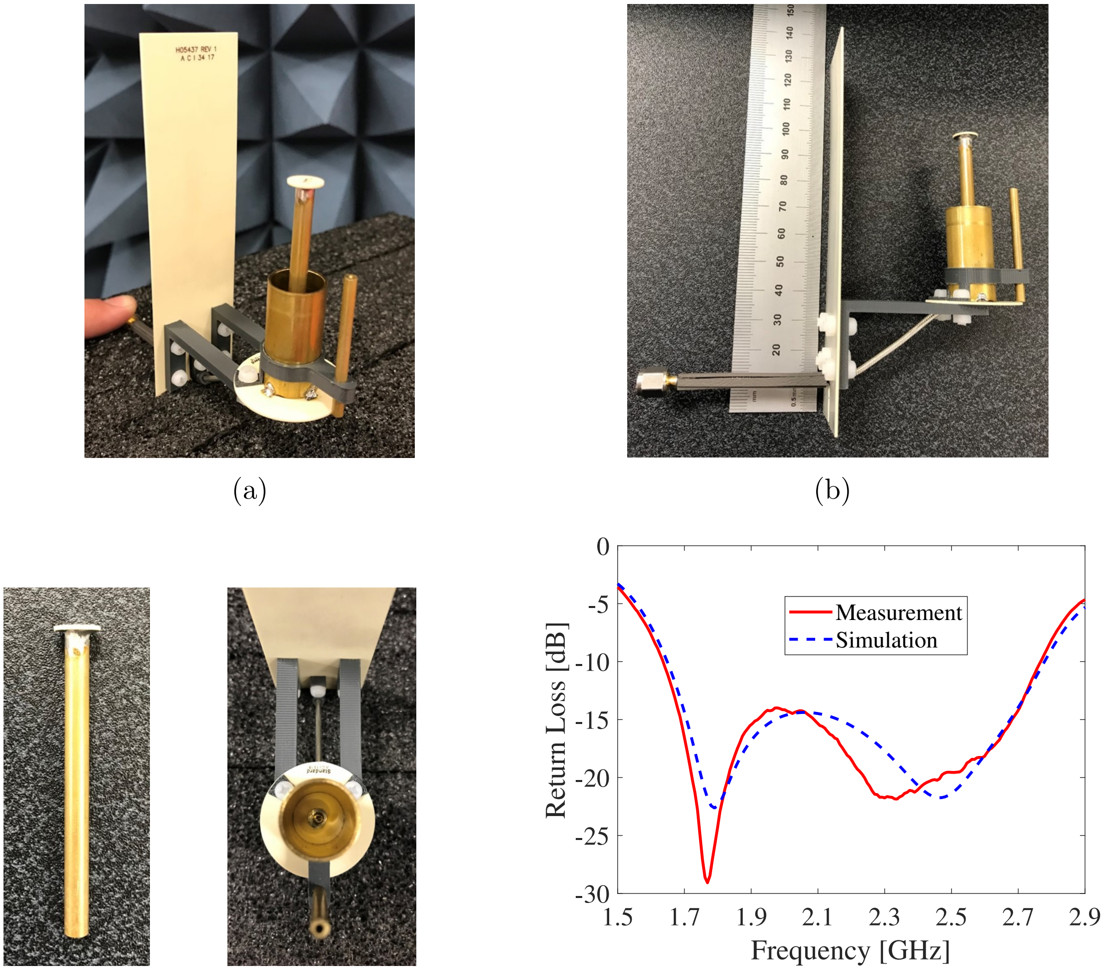

(a) (b)

(c) (d) (e)

Figure 5.16: Fabricated antenna configuration A isometric view (a), side view (b), main radiator (c), threaded rod (d), and simulated and measured return loss (e).

the pattern measurements. The range cable is wrapped with absorber to minimize ther impact to the radiation patterns, but it can still have a small impact. Some of the asymmetry observed in the cross-pol is likely due to the range cable. In all cases studied, the elevation patterns are plotted at ϕ=0°, and the azimuth patterns are plotted at θ corresponding to the measured main beam peak. For measured patterns, the main beam peak occurs at elevation angles of θ=85° (1.7 GHz), θ=97° (2.2 GHz), and θ=97° (2.7 GHz). For simulated patterns, the main beam peak occurs at elevation angles of θ=91° (1.7 GHz), θ=93° (2.2 GHz), and θ=101° (2.7 GHz).

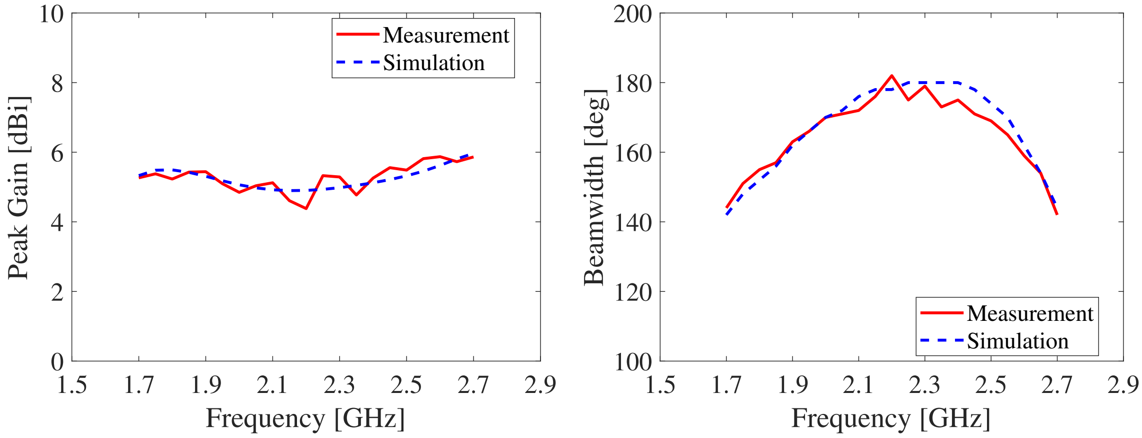

(a) (b)

Figure 5.17: Configuration A simulated peak realized gain and measured peak gain (a) along with simulated and measured az-HPBW (b) vs. frequency.

5.4.2 Simulated and Measured Results - Configuration B

A fabricated configuration B antenna is pictured in Fig. 5.19, and the simulated and measured return loss is shown in Fig. 5.19d. Note that aside from the main radiator, this is the same antenna as pictured in Fig. 5.16. Good agreement is obtained between simulation and measurement where the measured return loss is better than 19 dB from 1.9-2.4 GHz. The variations in return loss are likely due to fabrication and assembly tolerances in soldering the loading disk to the monopole at the desired height.

The measured gain and azimuth beamwidth for antenna B are shown in Fig. 5.20 where the peak gain measures from ∼4.38-5.5 dBi, and the beamwidth measures from ∼161°-179°. The maximum beamwidth for antenna B is a bit more narrow than that for antenna A. This is due to the fact that there is slightly less squint for antenna B compared to antenna A due to the shorter main radiator. As a result, more of the azimuth pattern is squeezed by the reflector creating a slightly more narrow azimuth pattern. The normalized simulated and measured radiation patterns are shown in Fig. 5.21 where very good agreement is obtained between measurement and

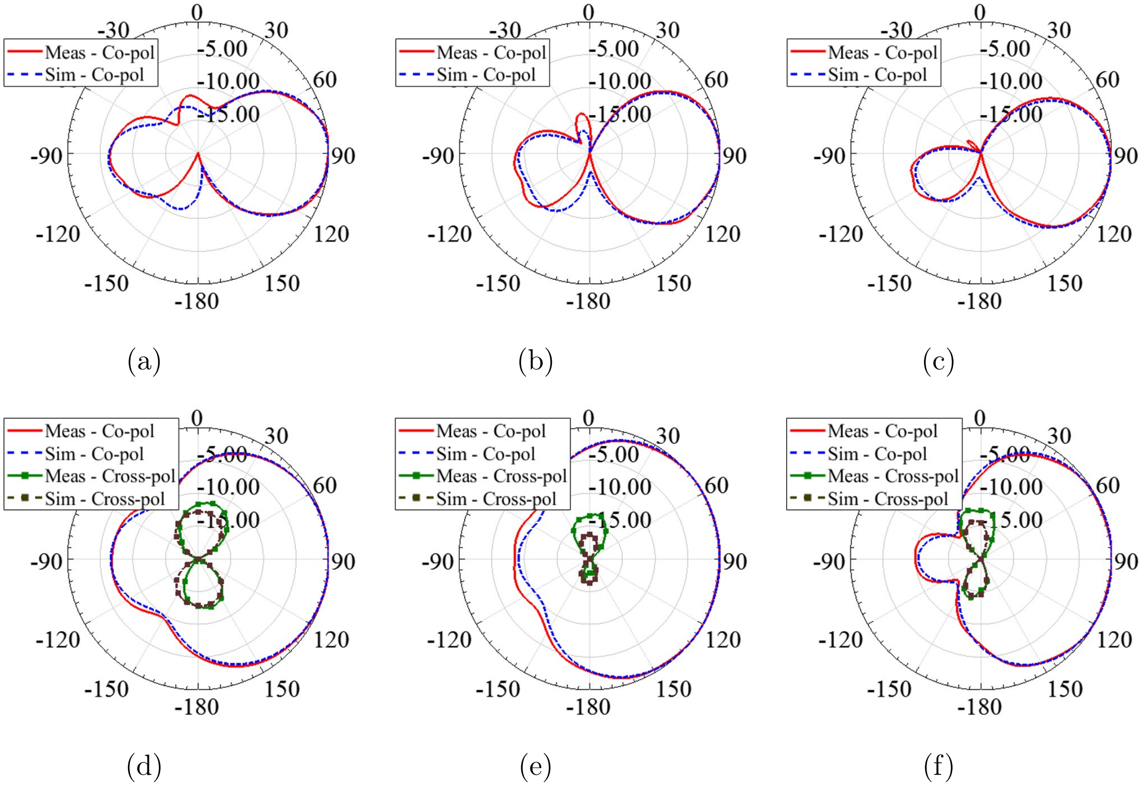

(a) (b) (c)

(d) (e) (f)

Figure 5.18: Simulated and measured radiation patterns for antenna configuration A. Elevation patterns are shown at 1.7 GHz (a), 2.2 GHz (c), and 2.7 GHz (e), and azimuth patterns are shown at 1.7 GHz (b), 2.2 GHz (d), and 2.7 GHz (f).

simulation. There are some small variations similar to those measured for antenna A. For measured patterns, the main beam peak occurs at θ=90° (1.9 GHz) and θ=96° (2.4 GHz). For simulated patterns, the main beam peak occurs at elevation angles of θ=92° (1.9 GHz) and θ=94° (2.4 GHz).

5.4.3 Simulated and Measured Results - Configuration C

A fabricated configuration C antenna is pictured in Fig. 5.22. The main radiator is machined from a piece of brass tube, and the filter support is 3D printed ABS.

The simulated and measured return loss is plotted in Fig. 5.22e where very good agreement is achieved between simulation and measurement. The 10-dB return loss bandwidth measures from ∼1.65-2.76 GHz. Note that three small pieces of General Plastics RF-2203 (ϵ_r=1.06, tanδ=0.001) low dielectric foam are situated between the

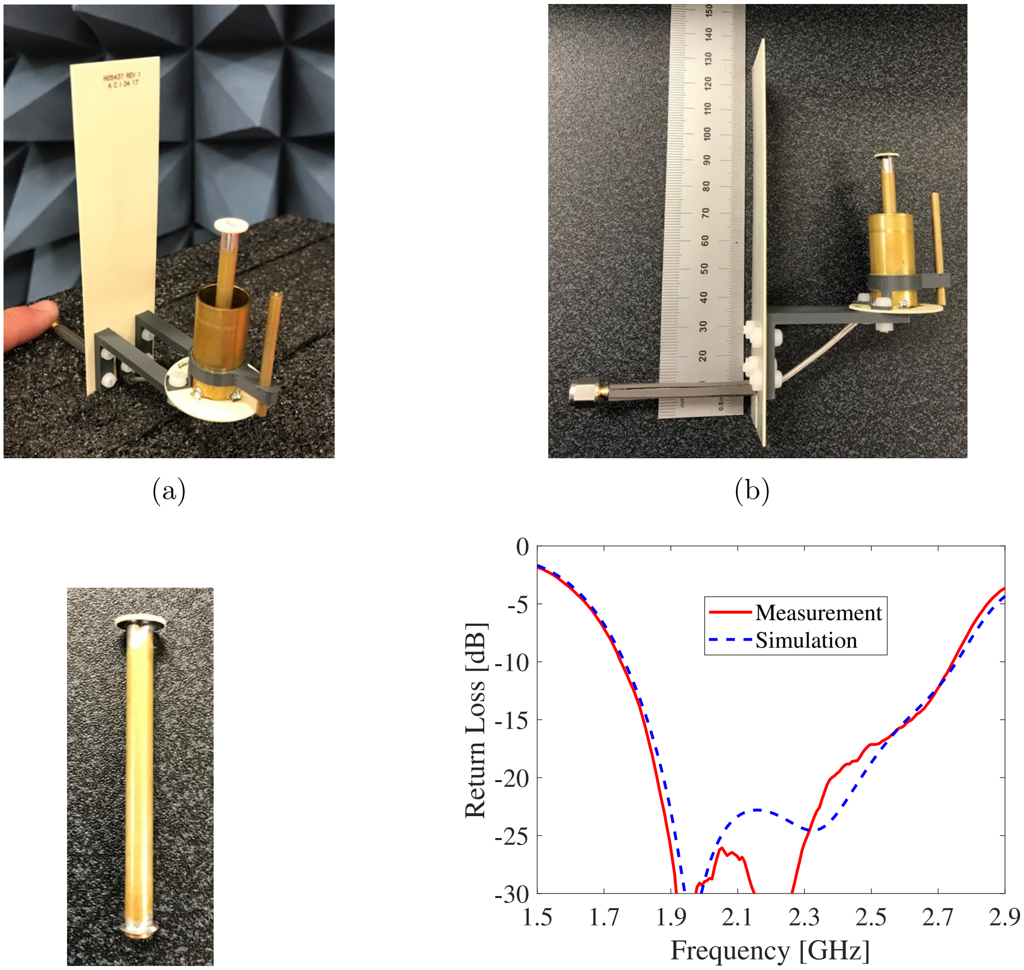

(a) (b)

(c) (d)

Figure 5.19: Fabricated antenna configuration B isometric view (a), side view (b), main radiator (c), and simulated and measured return loss (d).

sleeve and the filter support structure during testing. These pieces of foam provide mechanical support and maintain proper alignment for the filter elements without electrically loading the antenna.

Figure 5.23 shows the simulated and measured gain and beamwidth for antenna C. The measured gain for the antenna is ∼4.3-5.78 dBi, and the az-HPBW is ∼140°-180°. Similar to antenna B, antenna C exhibits a slightly reduced azimuth beamwidth compared to antenna A. This is also due to a slight reduction the beam squint due to the shorter main radiator. The simulated and measured radiation patterns for antenna C are pictured in Fig. 5.24 where very good agreement is obtained between

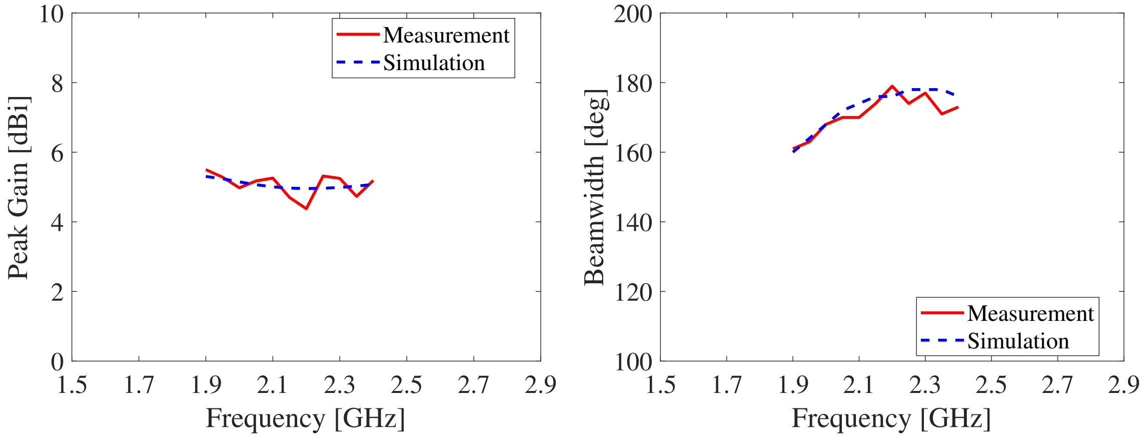

(a)

(b)

Figure 5.20: Configuration B simulated peak realized gain and measured peak gain (a) along with simulated and measured az-HPBW (b) vs. frequency.

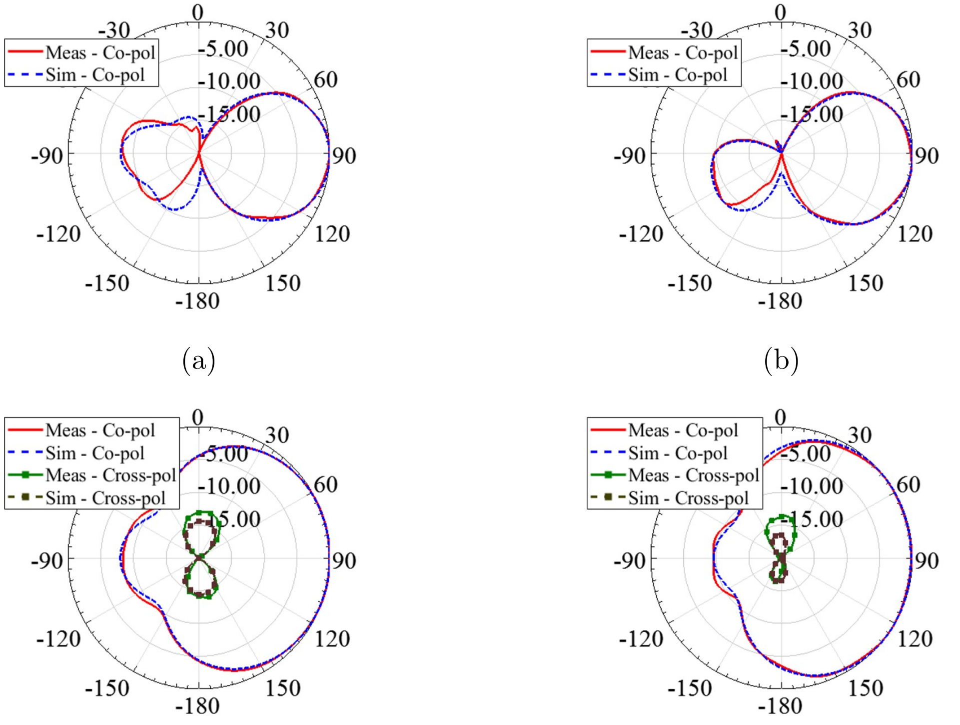

(a)

(b)

(c)

(d)

Figure 5.21: Simulated and measured radiation patterns for antenna configuration B. Elevation patterns are shown at 1.9 GHz (a) and 2.4 GHz (c), and azimuth patterns are shown at 1.9 GHz (b) and 2.4 GHz (d).

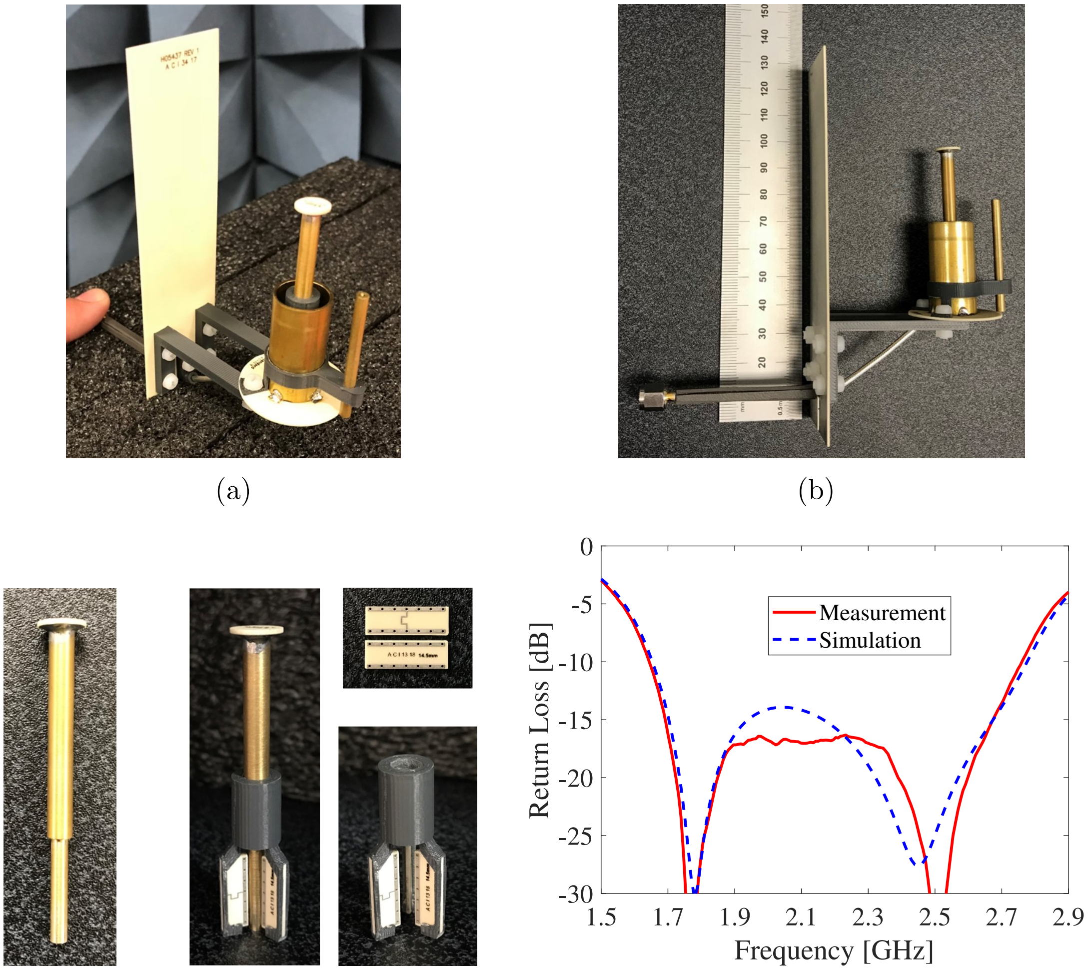

(a) (b)

(c) (d) (e)

Figure 5.22: Fabricated antenna configuration C isometric view (a), side view (b), main radiator (c), filter and filter support (d), and simulated and measured return loss (e).

measurement and simulation. The variations in simulation and measurement are due to manufacturing and assembly tolerances as well as some impact from the feed cable for pattern testing. For measured patterns, the main beam peak occurs at elevation angles of θ=85° (1.7 GHz), θ=96° (2.2 GHz), and θ=95° (2.7 GHz). For simulated patterns, the main beam peak occurs at elevation angles of θ=91° (1.7 GHz), θ=93° (2.2 GHz), and θ=98° (2.7 GHz).

The filter performance is demonstrated in Fig. 5.25 where the return loss and peak gain for antenna C is compared to that for antenna A. The filter is primarily designed

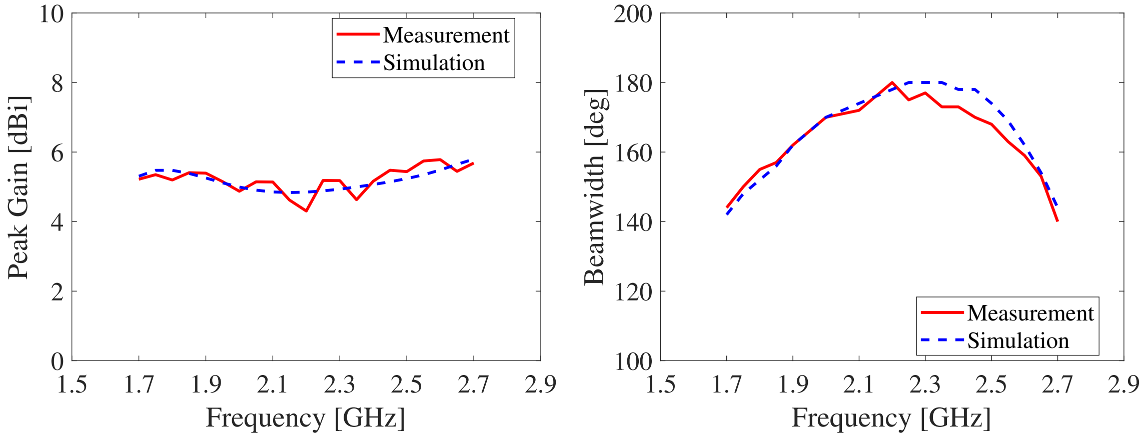

(a) (b)

Figure 5.23: Configuration C simulated peak realized gain and measured peak gain (a) along with simulated and measured az-HPBW (b) vs. frequency.

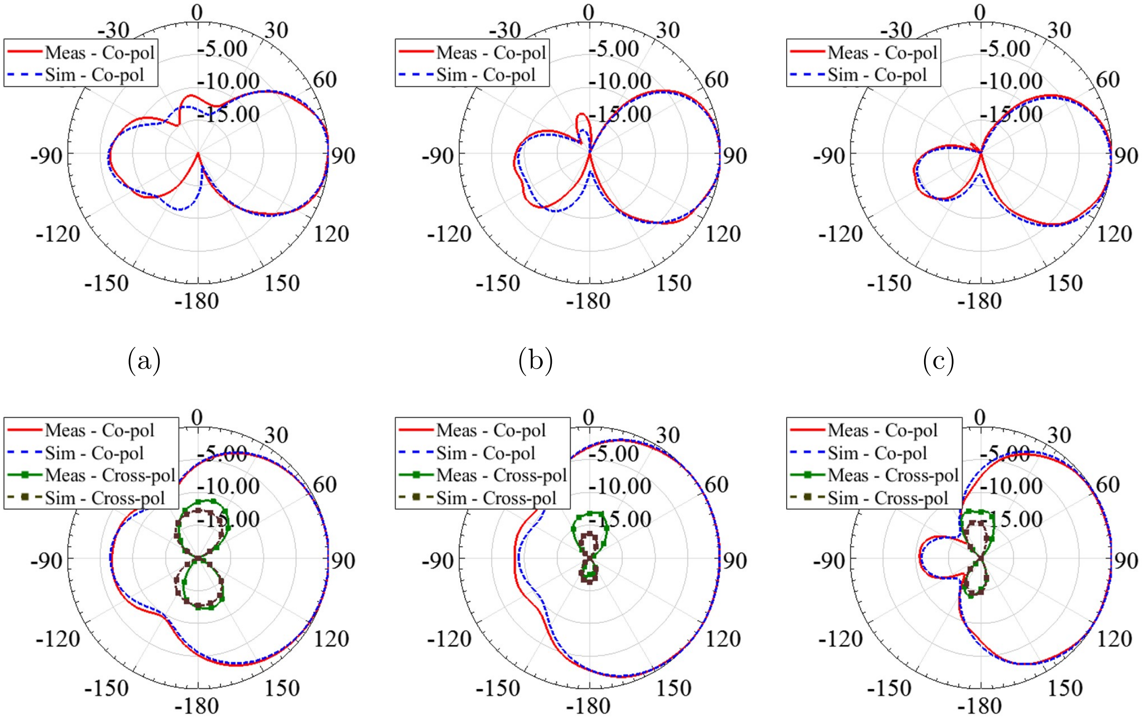

(a) (b) (c)

(d) (e) (f)

Figure 5.24: Simulated and measured radiation patterns for antenna configuration C. Elevation patterns are shown at 1.7 GHz (a), 2.2 GHz (c), and 2.7 GHz (e), and azimuth patterns are shown at 1.7 GHz (b), 2.2 GHz (d), and 2.7 GHz (f).

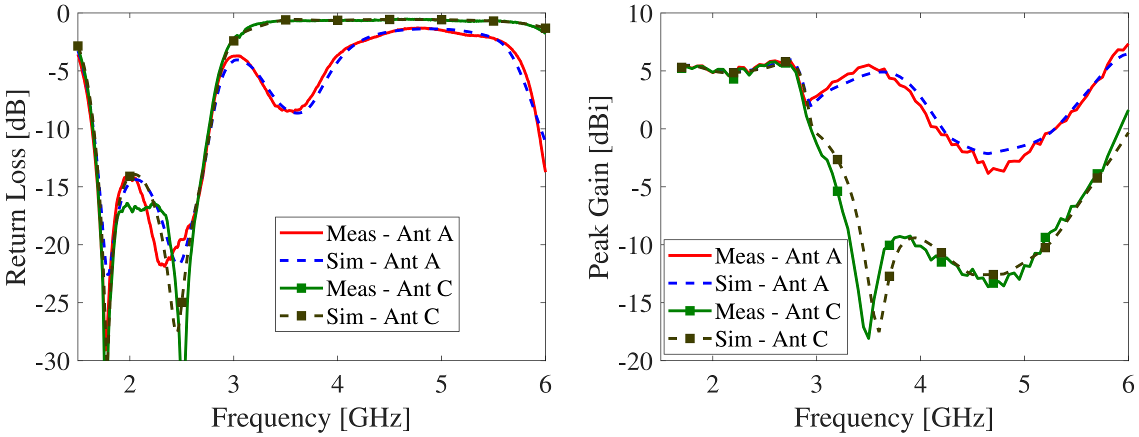

(a) (b)

Figure 5.25: Antenna configuration C filter performance compared to antenna configuration A for return loss (a) and peak gain (b) vs. frequency.

to operate from 3.3-5.925 GHz covering recently introduced LTE bands as well as those for Wi-Fi and WiMAX. The measured S_{11} from 3.3-5.925 GHz is better than ∼1.36 dB, and antenna C provides a gain reduction compared to antenna A between ∼6.1-23.6 dBi from 3.3-5.95 GHz. Note that the RF absorber lining the feed cable is modeled with ϵ_r=38, tanδ_e=0.01, μ_r=2, and tanδ_m=1.2 for simulations from 3-6 GHz.

5.5 Conclusion

This chapter presents a wide-beam antenna with modular main radiator for base station applications. Three antenna variations are shown which are made possible with the modular main radiator. Antenna A is considered the baseline antenna where a 10-dB return loss bandwidth from 1.64-2.76 GHz is achieved with an azimuth beamwidth between ∼142°-182° is demonstrated. The benefit of a parasitic director coupled to the antenna is presented where the director improves the 10-dB crossover point compared to the antenna without a director. A second antenna, antenna B, is presented where the antenna is tuned for optimal performance from 1.9-2.4 GHz where the measured impedance match is better than 19 dB. Pattern performance demonstrates wide-beam performance as well. Finally, antenna C is introduced where a metamaterial-based harmonic suppression filter is included in the antenna requiring no additional volume compared to antenna A. The filter provides rejection in S_{11} of better than ∼1.36 dB from 3.3-5.925 GHz, and the antenna provides gain reduction from ∼6.1-23.6 dBi from 3.3-5.95 GHz. This versatile antenna is ideal for small cell base station and DAS applications requiring wide azimuth beamwidth, but the antenna could be useful in any application where in-situ antenna adjustment may be desirable.

I would like to acknowledge the support of Amphenol Antenna Solutions in this work. I would like to thank Carl Gersch, Steve Zema, and Eric Berry of Amphenol Antenna Solutions for support in 3D printed and machined parts. I would also like to thank Michael Hoyak of Amephnol RF for providing the coaxial material test fixture. This work is patent-pending under U.S provisional patent application no. 62/696,538.

CHAPTER 6: DUAL BAND 4G/5G ANTENNA FOR NEXT GENERATION BASE STATIONS

6.1 Introduction

Future fifth generation (5G) wireless systems promise to provide unprecedented performance compared to today's wireless networks. The success of 5G partially depends on the use of frequencies up to and including millimeter wave (mmW) where a significant amount of spectrum is available for use [3, 7, 8]. One of the challenges in using higher frequencies is the resulting path loss leading to a dense network of antennas to support desired coverage levels. Furthermore, 5G will not immediately replace technology dedicated to previous generations, and it is unlikely that mmW will ever completely replace the lower carrier frequencies for voice calls and low speed data transmissions. Additionally, zoning restrictions create a need to consolidate antennas as much as possible. Broadband and multi-band antenna systems covering frequencies from 600 MHz to possibly 70 GHz will be required to integrate 5G into the market. Fortunately, the spectrum will be segmented enabling unique opportunities for multi-band antenna solutions.

This chapter presents a dual band antenna covering 1.7-2.7 GHz for 2G/3G/4G/LTE as well as 27.5-28.35 GHz for 5G (patent pending). The low band (LB) antenna is a three-sided triangular sleeve monopole antenna. The high band (HB) antenna consists of six series-fed patch arrays configured for single linear polarization where two arrays are configured on each face of the triangular sleeve. The HB arrays are integrated into the LB monopole where the LB sleeve also serves as the ground plane for the HB arrays. Integration of the HB arrays in this way enables 5G functionality to be added to the monopole without increasing the overall antenna volume. The LB antenna is omnidirectional in the H-plane, and the high band antenna is configured for tri-sector coverage where the three arrays are fed individually for capacity enhancement. The HB antenna also provides 2x-MIMO coverage in each sector where two spatially separated antennas provide decorrelated MIMO operation [1, 2]. Both the LB and HB antennas exhibit a 10-dB return loss or better over the stated operating bands. To minimize the chance for interference between LB and HB, a defected center coaxial band stop filter designed to block signals in the 27.5-28.35 GHz band is integrated into the feed portion of the LB antenna.

6.2 Antenna Design

6.2.1 Low Band Antenna

The low band antenna is a triangular sleeve monopole antenna as shown in Fig. 6.1 and operates from approximately 1.7-2.7 GHz. The antenna consists of a main radiator, a sleeve, and a ground plane where all components are made of 0.508-mm Rogers RO4003 PCB material ($\epsilon_r \simeq 3.55$ and $\tan\delta \simeq 0.0027$). The antenna is fed with an RG-402 coaxial cable that feeds into strip-centered coax for reasons that will be explained in section 6.2.3. The main radiator is fed directly from the strip-centered coaxial line as shown in Fig. 6.1d. The feed cable is also wrapped with 1-mm thick absorber to reduce the impacts of the feed cable on the radiation patterns. The material parameters used for LB simulations are ϵ_r=38, $\tan\delta_e$=0.01, μ_r=4, and $\tan\delta_m$=0.75 which correspond to the data reported by [144] and illustrate one of a number of possibilities for absorbing material. The ground plane of the LB antenna contains cutouts for tabs on the sleeve walls to pass through as well as holes for the HB cables and LB feed. The LB radiator is also modeled with a LB radiator support made of a plastic bolt with plastic nuts (ϵ_r=2.8 and $\tan\delta$=0.018) placed on either side of the LB radiator. This support is used to maintain the alignment of the LB radaitor, and it also maintains the spacing between the LB radiator and the sleeve. The bolt is found to have little impact on the performance of the antenna. The antenna is also modeled with ABS (ϵ_r=2.5 and tanδ=0.007) sleeve supports which would be used to align and provide mechanical support to the sleeve walls in antenna assembly.

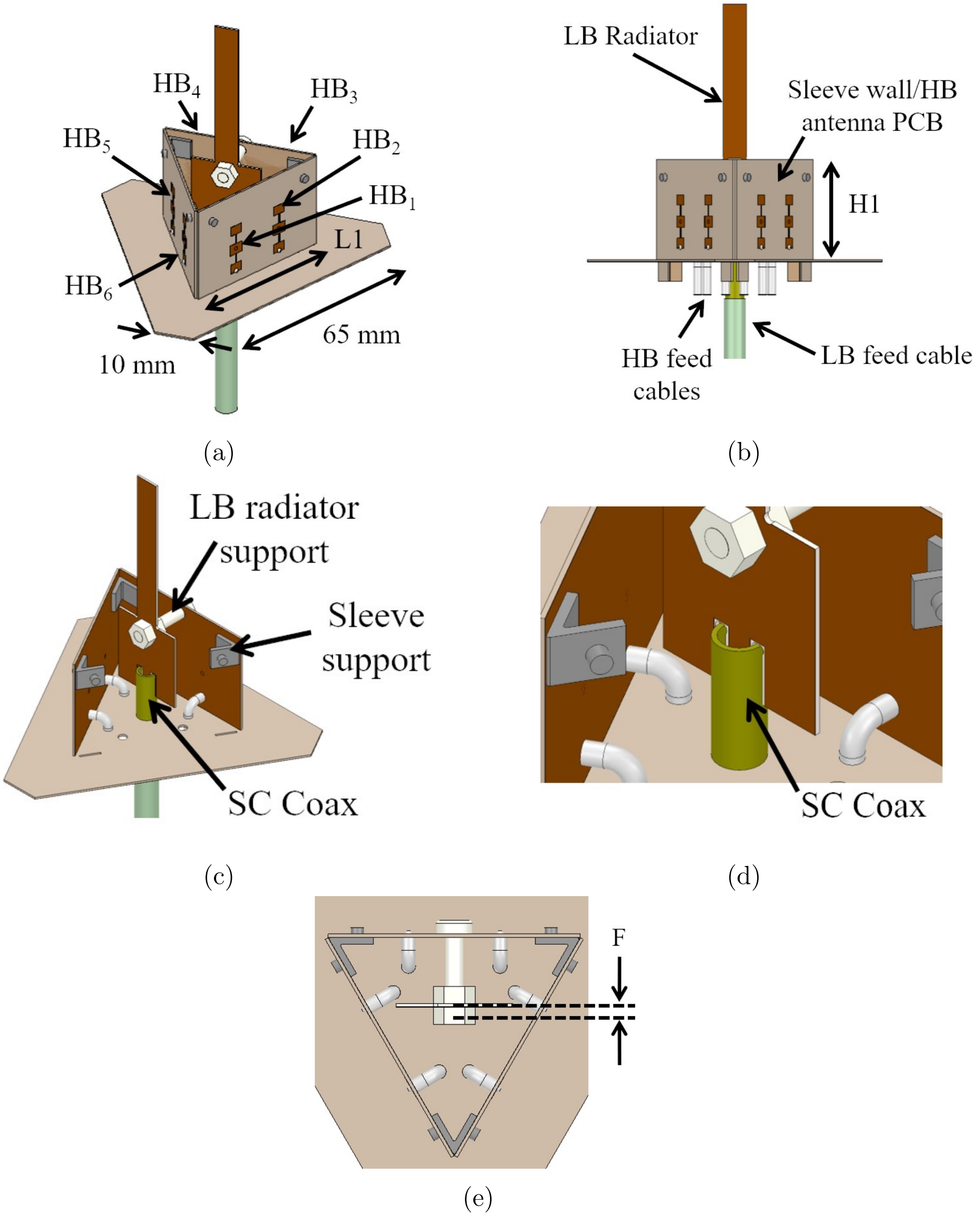

(a) (b)

(c) (d)

(e)

Figure 6.1: Dual band antenna isometric view (a), front view (b), isometric view with sleeve wall/HB antenna removed (c), close-up of the LB feed section (d), and LB feed offset.

Detailed views of the LB radiator are pictured in Fig. 6.2 where essentially every

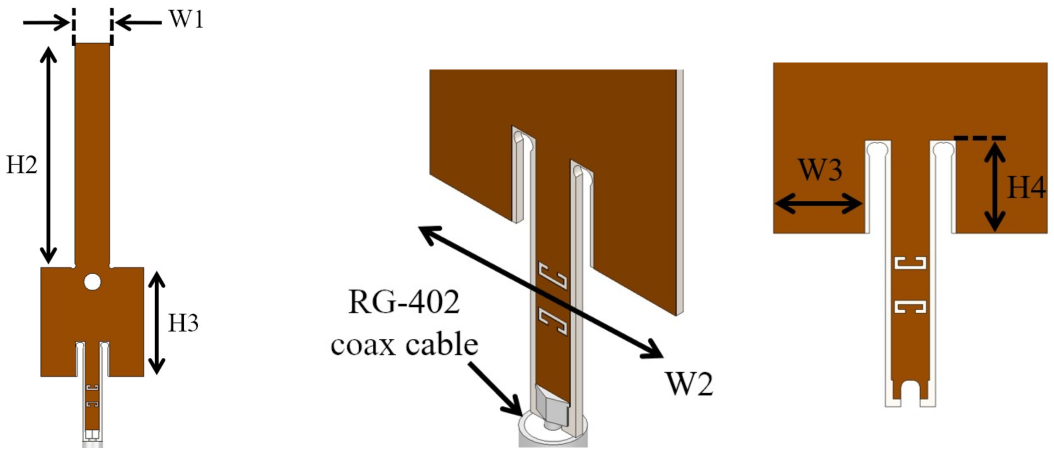

(a) (b) (c)

Figure 6.2: LB main radiator front view (a), isometric view showing coaxial cable connection (b), and close-up front view (c).

piece of the LB radiator provides some degree of tuning. The impacts of W1, W2, H2, H3, and H4 are investigated in Figs 6.3 and 6.4. The width of the main radiator, W1, does not have a significant impact on the return loss of the antenna, but it is shown that wider W1 can provide more bandwidth at the expense of in-band performance. The width, W2, on the other hand, has considerable impact on the input match to the LB antenna. Larger W2 can improve the match at the low end of the operating band, and a smaller W2 can be used to improve the match at the upper end of the operating band.

Figure 6.4 illustrates the impacts of H2, H3, and H4 on the LB antenna performance. Figure 6.4a shows the impacts of the height of the main radiator, H2. It is shown that a shorter H2 can tune the match to lower frequencies at the expense of matching near the upper end of the operating band. A longer H2 can provide significantly improved match at the upper end of the operating range as well as in the middle part of the band. Unfortunately, this comes at the expense of matching at the low end of the operating band. The height H3 can be used to tailor the response to the upper or lower end of the operating band where a shorter H3 improves the match at the upper end of the operating band, and a taller H3 improves the match at the

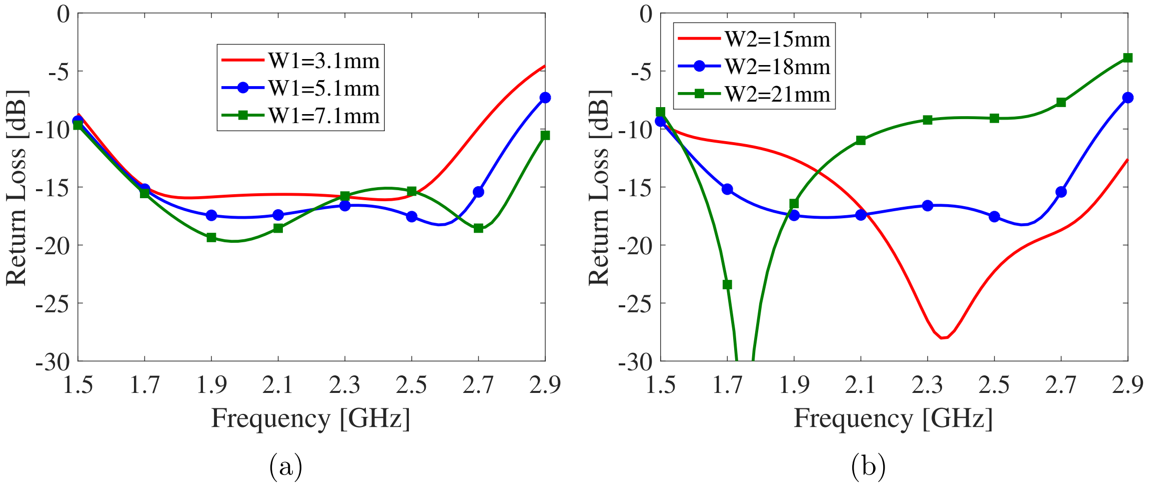

Figure 6.3: Low band parametric study for W1 (a) and W2 (b).

lower end of the operating band. The tab at the bottom of the main radiator detailed in Fig. 6.2c can be used to fine-tune the response where increasing or decreasing the height can improve the match at the upper or lower end of the band, respectively.

6.2.2 High Band Antenna

The high band antenna is composed of six series fed linear arrays of patch antennas as shown in Fig. 6.1a where each array, pictured in Fig. 6.5, is designed to operate from 27.5-28.35 GHz [39, 148–151]. Typically, the first element of the series fed patch array is fed with microstrip transmission line. In this case, the first element of each series fed array is probe fed with RG-405 coaxial cable to reduce cost and volume. Since a microstrip feed is not required for this antenna, the feed cables can be run into the LB sleeve and the HB arrays can be fed from within the LB sleeve. Therefore, a microstrip trace is not required to run below the ground plane and then make some transition to coax, and the cables can be routed along with the LB feed cable outside of a radome for the smallest possible package size. Furthermore, cable feeding the antennas eliminates the need for a high frequency coax-to-pcb connector. RF and millimeter wave connectors and adapters can be costly for high quality components, and their installation is generally not trivial. Cable feeding the antenna only requires

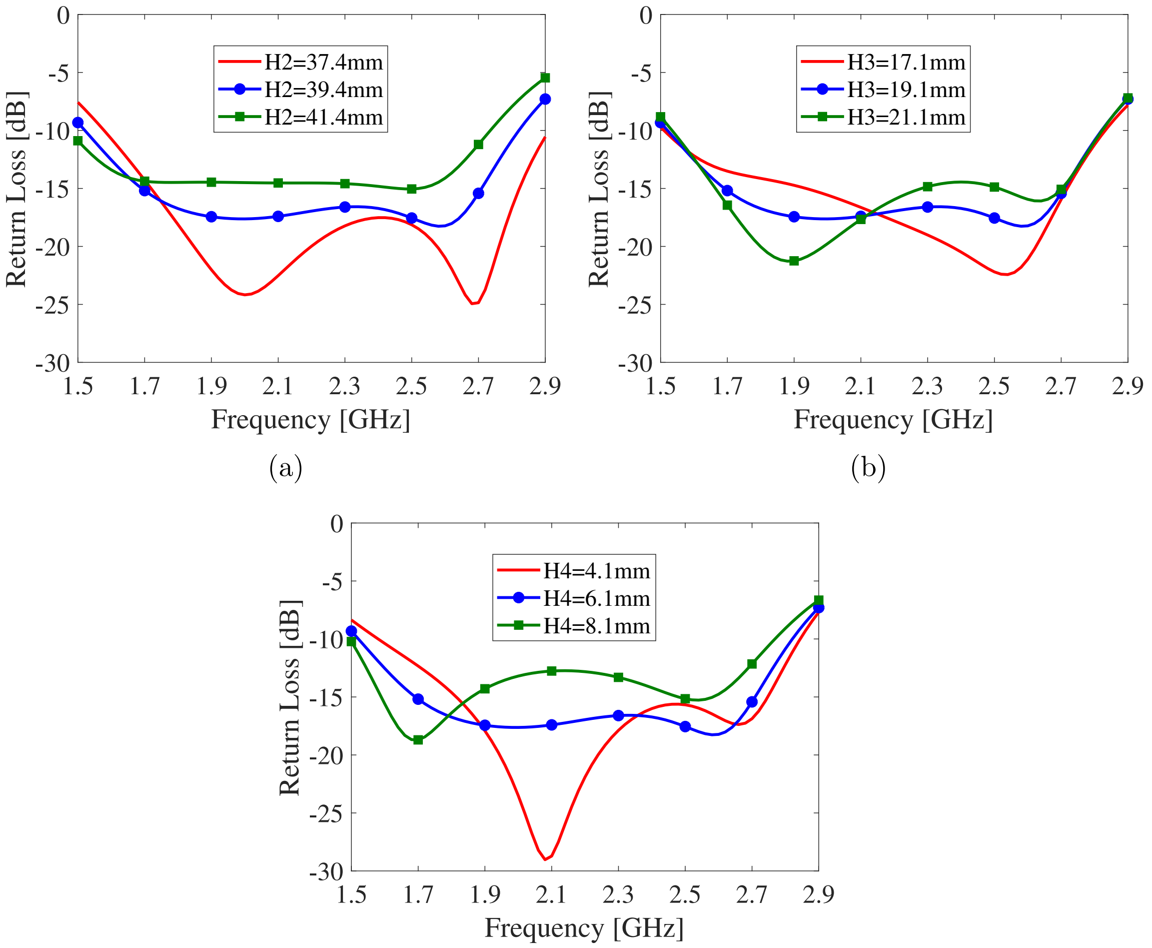

(a)

(b)

(c)

Figure 6.4: Low band parametric study for H2 (a), H3 (b), and H4 (c).

cable prepping and two solder joints to make the connection from coax to the antenna.

The central element for each array is slightly larger than the two outer elements for bandwidth enhancement [149–151]. Also notice that there is a via placed in the middle of the central element on each array. It is observed that the series fed array exhibits resonances lower in frequency than the lowest order operating mode of the patch. These resonances are believed to be due to the length of the array and do not provide desired radiation patterns. Therefore, it is desirable to push these modes as far from the operating mode of the patch array as possible, and the via helps to do that. Note that a short section of the coaxial feed cable is also included in the

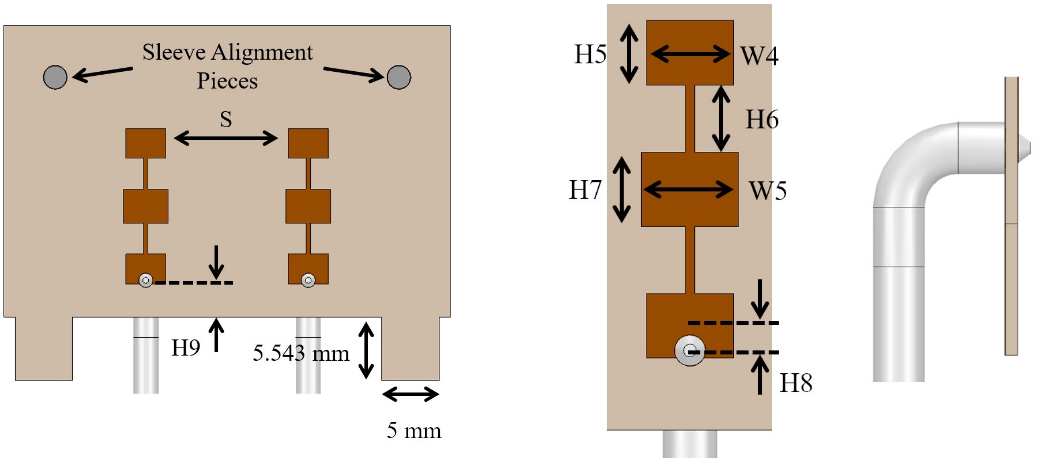

(a) (b)

Figure 6.5: Detailed view of LB sleeve/HB antenna PCB (a) along with a close-up and side view of the HB array (b).

simulation domain for HB analysis. This cable is modeled as being wrapped in 1-mm thick absorber with material properties of ϵ_r=38, tanδ_e=0.01, μ_r=1, and tanδ_m=1. These values are assumed based on the high frequency data provided in [144].

To enable MIMO capability, two series fed arrays are integrated onto each face of the sleeve for tri-sector MIMO coverage. In this case, MIMO is achieved through spatial diversity since the antennas are small enough to separate and achieve the desired isolation between ports. An investigation of the coupling between arrays vs. separation distance is illustrated in Fig. 6.6 where the port-to-port isolation and the envelope correlation coefficient (ECC or ρ) are plotted for various spacing between the arrays. The ECC is a metric that is used to determine the MIMO capability of two antennas where the lower the ECC, the better suited the antennas are for MIMO operation. In the most accurate sense, the ECC is calculated from the radiation patterns, but it has been demonstrated that the ECC can be accurately computed from S-parameters when the antenna efficiency is better than ~80% [152]. Radiation patterns simulated at 27.5 GHz, 27.9 GHz, and 28.35 GHz indicate radiation efficiency better than ~93% for the HB antenna in this chapter. The ECC (ρ) for two antennas operating in a MIMO configuration is computed from S-parameters by [152, 153]

$$\rho = \frac{|S_{11}^{*}S_{12} + S_{21}^{*}S_{22}|^2}{(1-|S_{11}|^2-|S_{21}|^2)(1-|S_{22}|^2-|S_{12}|^2)}. \tag{6.1}$$

Figure 6.6 demonstrates that closer spacing between the arrays degrades port-to-port isolation and ρ which in-turn degrades MIMO performance. A spacing of 10.28 mm is found to provide an isolation better than 30 dB with an ECC better than 0.4x10^{-4} between MIMO antenna ports for the present antenna. It is generally desired to minimize the ECC for MIMO applications, but the authors of [154] specify a required ECC of 0.5 or better at the terminal and 0.7 or better at the base station for MIMO operation.

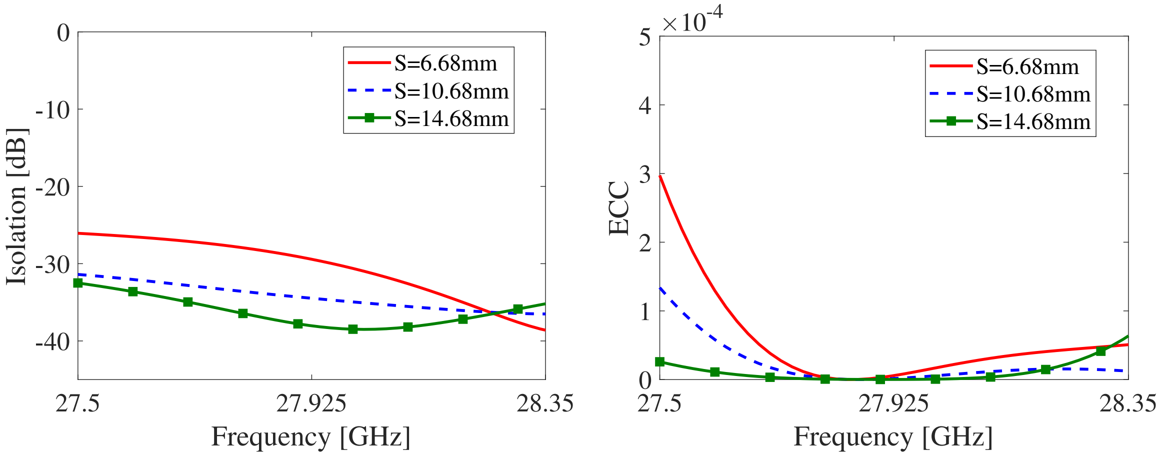

(a) (b)

Figure 6.6: High band antenna port-to-port isolation (a) and ECC (b) for ports 1 and 2.

The spacing between the HB arrays and the LB ground is also investigated, and it is found that this distance has an impact on the elevation patterns as shown in Fig. 6.7. The main beam is largely unaffected, but there is an impact in the sidelobe performance. Reducing H9 can minimize sidelobe levels toward zenith, but this creates an increase in the first sidelobe level. Increasing H9 lowers the first sidelobe level, but this leads to increase in the sidelobe levels near zenith.

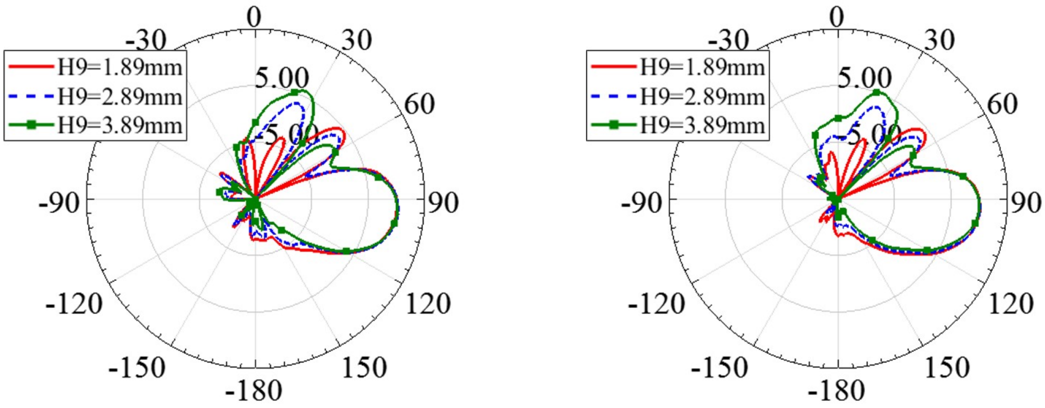

(a)

(b)

Figure 6.7: High band antenna elevation patterns at 27.9 GHz for port 1 (a) and port 3 (b) with changes in H9.

6.2.3 Interference Mitigation Filter

It is shown in Section 6.2.1 that the LB antenna is fed with strip-centered coaxial transmission line. This is done primarily to incorporate HB filtering into the LB element. It is found that the LB element can effectively radiate in the HB frequency range if measures are not taken to prevent it. Therefore, a HB band stop filter is integrated into the LB feed. The filter in this chapter is an FiF approach, but since the feed is extended into the sleeve of the LB antenna, this approach could be considered FiA as well.

The analysis begins with a study of strip-centered coax (SCC) transmission line characteristic impedance, Z_0. Equations for the strip centered coaxial line filled with a homogeneous dielectric material are given in [155]. For $Z_0 < 30\pi/\sqrt{\epsilon_r}$ (Ω), Z_0 for uniformly filled SCC is given as

$$Z_0 = \frac{15\pi^2}{\sqrt{\epsilon_r}} \frac{1}{ln\left(\frac{2(D_d+w_t)}{D_d-w_t}\right)} \tag{6.2}$$

where ϵ_r is the dielectric constant of the material filling the space between the strip and the outer conductor, D_d is the inside diameter of the outer conductor, and w_t is the width of the trace. Note that this also assumes that the trace is very thin.

Unfortunately, the partially filled coaxial line is not addressed in [155]. The SCC line presented in this paper is realized using a PCB material for the center strip, and a partially filled line is the result. To calculate Z_0 for the partially filled line, we find that the dielectric constant in Equation 6.2 can be replaced with an effective dielectric constant given by [156]

$$\epsilon_{scc} = \alpha\epsilon_{r_1} + (1-\alpha)\epsilon_{r_2} \tag{6.3}$$

where α is a fill factor determined by taking the ratio of dielectric 1 to dielectric 2 in an angular sub-region of the transmission line as indicated in Fig. 6.8a. It is found that θ_α=105° gives very accurate results for characteristic impedance as indicated in Fig. 6.8b. The reason a sub-region is considered for this analysis is because the fields in strip-centered coaxial line are concentrated mostly between the edges of the strip and the walls of the outer conductor.

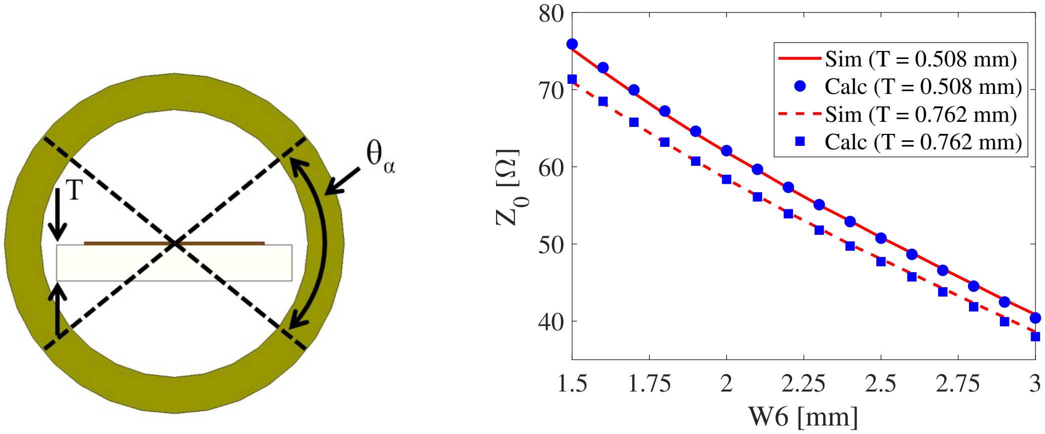

(a) (b)

Figure 6.8: SCC transmission line cross-sectional view (a) along with simulated vs. predicted Z_0 for various trace widths (b).

A HB band stop filter is integrated into the SCC line by the defected split ring resonators etched into the strip as shown in Fig. 6.9. The SRR and U-shaped resonator have been successfully used for band stop filtering on a number of occasions [157–159]. The SRR is used here due to easy fabrication and the ability to match the SRR response to an equivalent parallel LC circuit. This equivalence can be used to effectively design a defected center coaxial (DCC) filter using SCC transmission line.

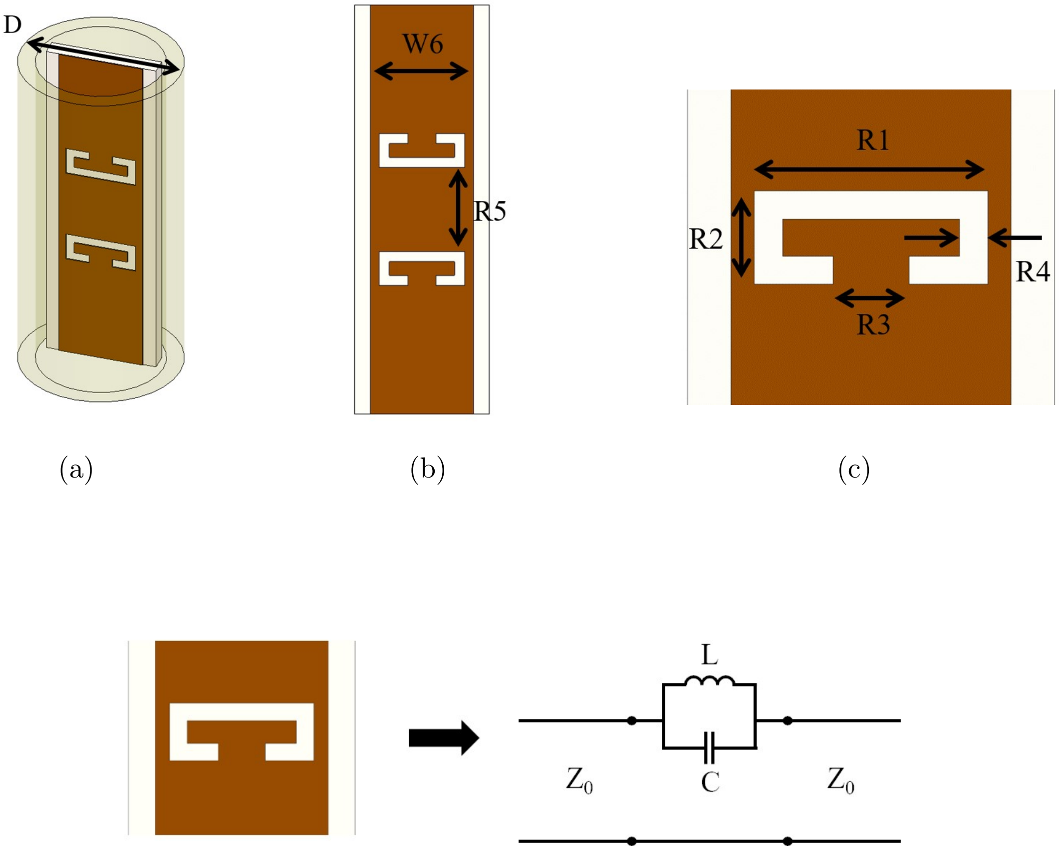

(a) (b) (c)

(d)

Figure 6.9: Various views of the DCC band stop filter (a)-(c) along with the equivalent circuit model (d).

Here, a 2nd order Butterworth band stop filter is design according to [53, 54] where the inductor and capacitor values are determined as

$$L = \frac{\omega g Z_0}{\omega_0} \simeq 0.088 \quad nH \tag{6.4}$$

$$C = \frac{1}{\omega \omega_0 g Z_0} \simeq 0.37 \quad pF \tag{6.5}$$

$$\omega_0 = \sqrt{\omega_1 \omega_2} = 1.74 * 10^{11} \quad \frac{rad}{sec} \tag{6.6}$$

$$\omega = \frac{\omega_2 - \omega_1}{\omega_0} = 0.216 \tag{6.7}$$

where g=1.4142, Z_0=50Ω, ω_1=$2\pi f_1$, f_1=24.92 GHz, ω_2=$2\pi f_2$, and $f_2 = 30.925$ GHz. This leads to the equivalent circuit in Fig. 6.10 where the transmission line connecting the two filter elements has characteristic impedance Z_0 with a length of $\sim \lambda/4$.

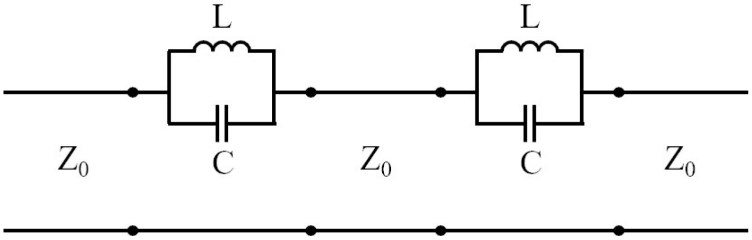

Figure 6.10: 2nd Order Butterworth filter circuit representing the DCC filter.

To realize the filter, circuit simulations are performed to determine the ideal frequency response for the 2nd order filter. This response is then used to design the single DCC filter element where the design dimensions are chosen to match the single element ideal filter response as shown in Fig. 6.11a. Those design dimensions are then applied to the 2nd order filter where the spacing between the filter elements is chosen to match the circuit response of the ideal Butterworth filter. The filter dimensions are listed in Table 6.1. Note that the SCC structure used in this section will support higher order mode propagation in the HB frequency range, but the coaxial cable used to feed the antenna exhibits a cutoff frequency beyond ~33 GHz. Therefore, the lowest order propagating mode is considered for the SCC structure and filter design in this study, and the data plotted in Fig. 6.11 reflects the filter performance for the lowest order propagating mode. It is important to check antenna gain when using this filter at high frequency to make sure energy is not coupled to another mode and radiated from the antenna.

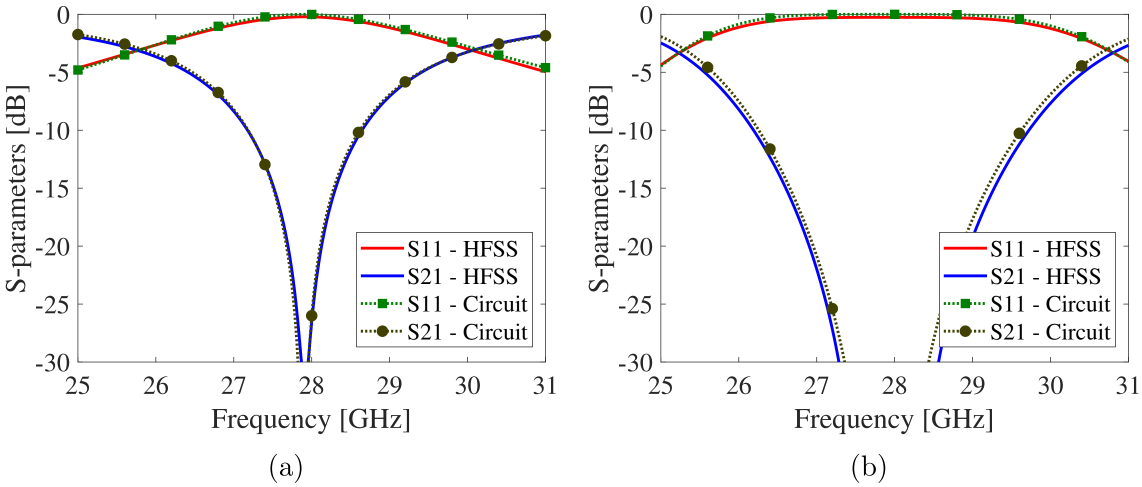

Figure 6.11: DCC filter S-parameter comparison of HFSS simulations and equivalent circuit model for the 1st order (a) and 2nd order (b) filters.

Table 6.1: Design dimensions for the DCC Butterworth filter in Fig. 6.9.

Variable	**mm**	**Variable**	**mm**	**Variable**	**mm**
D	4.7625	R3	0.721	W6	2.54
R1	2.12	R4	0.254		
R2	0.84	R5	1.95		

6.3 Results and Discussion

6.3.1 Low Band Antenna

The design dimensions for the LB portion of the antenna are listed in Table 6.2, and the simulated return loss is plotted in Fig. 6.12. HFSS simulations indicate a return loss better than 15 dB from ∼1.7-2.7 GHz covering 2G/3G/4G/LTE frequency bands.

Table 6.2: Design dimensions for LB portion of dual band antenna.

Variable	**mm**	**Variable**	**mm**	**Variable**	**mm**
H1	25.4	H4	6.1	W3	6
H2	39.4	W1	5.1	L1	39
H3	19.1	W2	18	F	0.5

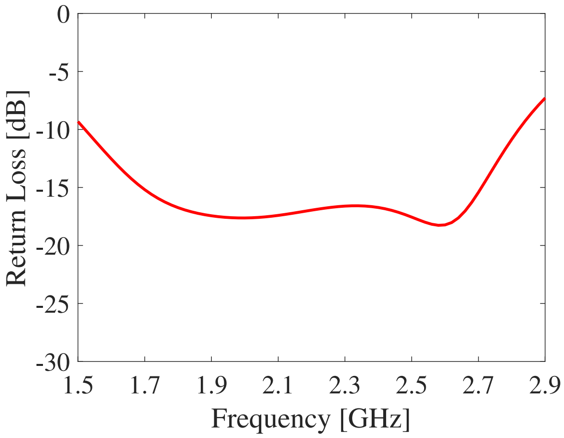

Figure 6.12: Low band return loss vs. frequency.

The radiation patterns for the LB antenna are pictured in Fig. 6.13 where it is shown that the antenna exhibits omnidirectional radiation patterns in azimuth. The elevation patterns are shown in Fig. 6.13a for a feed offset, F, of 0.5 mm. Note that the feed offset is chosen to balance the elevation patterns. With too much or too little feed offset, the LB patterns become asymmetric. The squint that is observed over frequency is common to the sleeve monopole antenna and is the result of radiation from the sleeve portion of the antenna.

6.3.2 High Band Antenna

The design dimensions for the HB antenna are listed in Table 6.3, and HFSS simulated S-parameters are plotted in Fig. 6.14. The return loss for HB ports 1 and 2, isolation between ports 1 and 2, and the isolation between ports 2 and 3 are shown in Fig. 6.14. The return loss from 27.5-28.35 GHz is better than 10 dB, and the port-to-port isolation is better than 30 dB. The isolation between arrays on neighboring

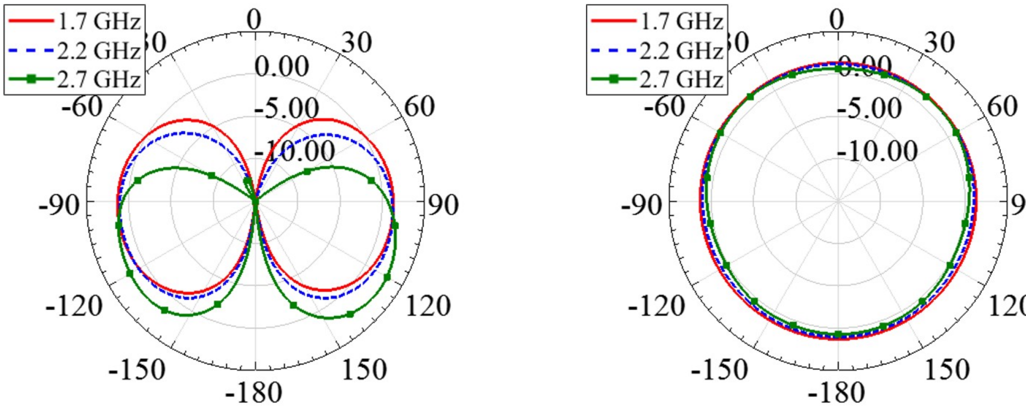

(a)

(b)

Figure 6.13: Low band antenna patterns in elevation at ϕ=0° (a) and azimuth at θ=90° (b).

faces is better than 40 dB in the desired operating band.

Table 6.3: Design dimensions for HB portion of dual band antenna.

Variable	**mm**	**Variable**	**mm**	**Variable**	**mm**
S	10.68	H7	2.975	W4	3.5
H5	2.575	H8	0.9875	W5	3.9
H6	2.7	H9	2.89		

The HB elevation patterns are shown in Fig. 6.15, and the HB azimuth patterns are shown in Fig. 6.16. The elevation patterns show downtilt of approximately 4°-6°, but this only leads to a few tenths dB variation in the gain at the beam peak vs. θ=90°. The azimuth sectorization is shown in Fig. 6.16 where Fig. 6.16a shows the azimuth patterns at θ=90° for odd numbered HB ports, and Fig. 6.16b shows the azimuth patterns at θ=90° for even numbered HB ports. Notice that the beam crossover points occur at ϕ ~0°, 120°, and 240° for both odd numbered ports and even numbered ports for the desired HB sectorization.

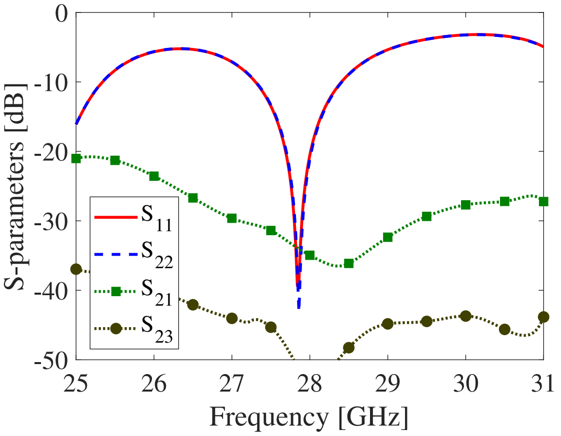

Figure 6.14: High band return loss and isolation vs. frequency.

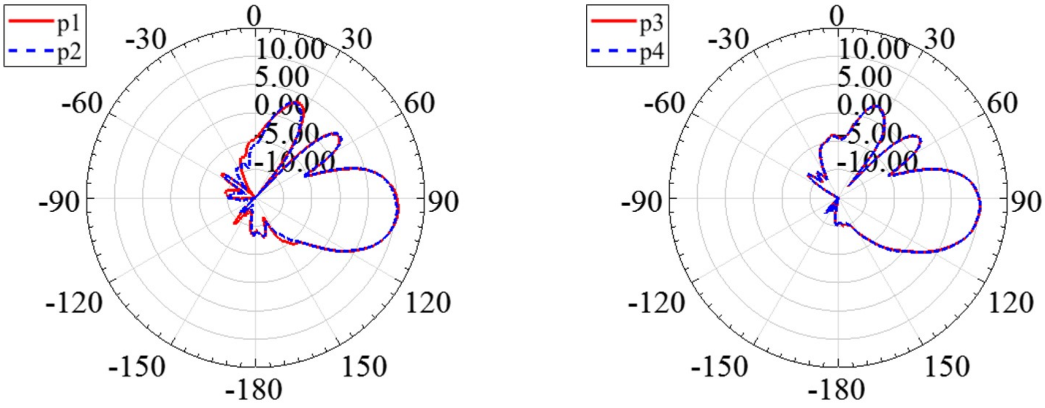

(a)

(b)

Figure 6.15: High band elevation patterns for p1 and p2 (a) as well as p3 and p4 (b).

6.3.3 Interference Mitigation Filter

The impacts of the interference mitigation filter are demonstrated in Fig. 6.17. The return loss and isolation between LB and HB port 4 are shown in Fig. 6.17a. The return loss in the HB frequency range is as low as approximately 10 dB for the LB antenna without the filter. With the filter, the simulated return loss is approximately 0.35 dB or higher. Furthermore, the isolation between LB and HB port 4 is improved from approximately 36 dB to better than 70 dB minimizing the possibility for port-to-port coupling between LB and HB ports in the HB frequency range.

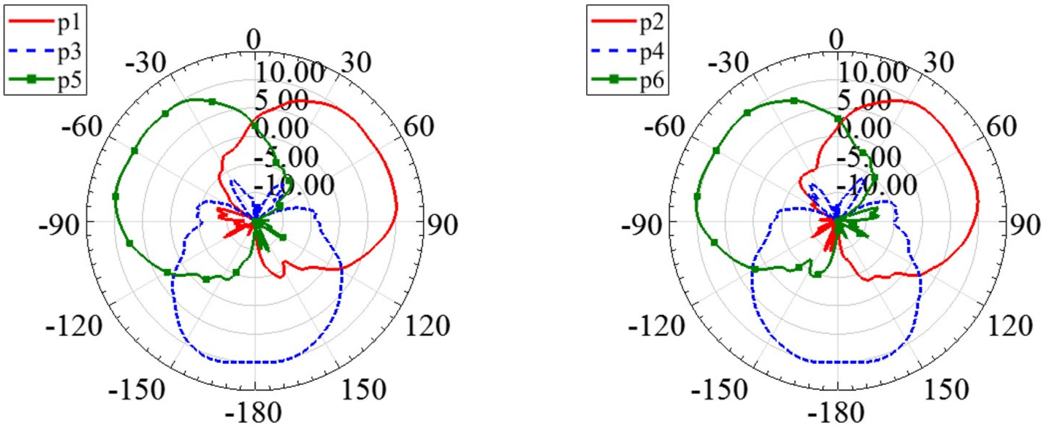

(a) (b)

Figure 6.16: High band azimuth patterns for odd ports (a) and even ports (b).

The radiation performance of the LB antenna in the HB frequency range is investigated in Fig. 6.17b. With the filter, HFSS simulations indicate more than 40 dB reduction in peak realized gain over the HB operating band compared to the antenna without the filter.

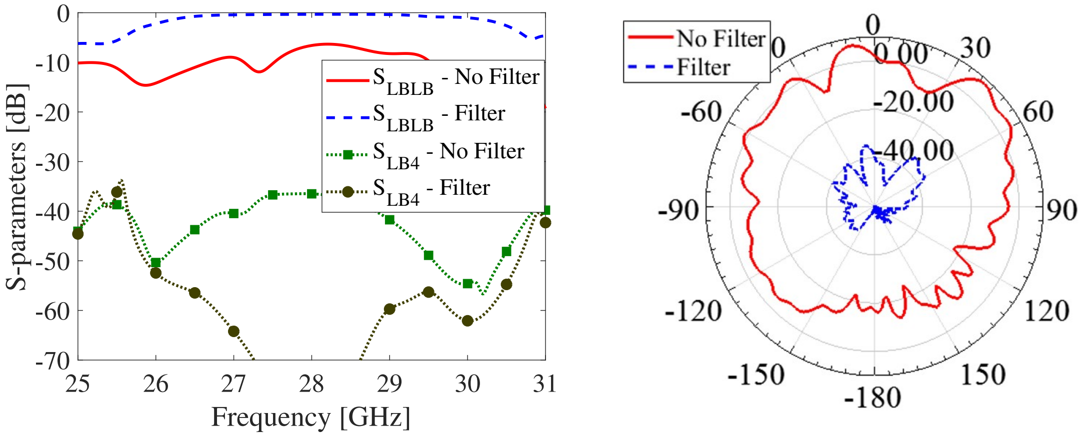

(a) (b)

Figure 6.17: Impact of interference mitigation filter on return loss and isolation (a) and radiation patterns at 27.9 GHz (b).

6.4 Conclusion

This chapter presents a dual band antenna covering 1.7-2.7 GHz as well as 27.5-28.35 GHz for next generation base station applications. The LB antenna (1.7-2.7

GHz) is a sleeve monopole with a triangular shaped sleeve for omnidirectional coverage. The HB antenna (27.5-28.35 GHz) consists of six series-fed patch antenna arrays for single linear polarization. Two arrays are configured on each face of the LB sleeve and used for 2x-MIMO performance. Furthermore, the HB antenna is configured to provide three sectors for enhanced capacity in the HB frequency range. The antenna design is ideal to bridge the gap between older base station technology and 5G where high frequency capability is added without increasing the overall volume of the LB antenna.

I would like to acknowledge the support of Amphenol Antenna Solutions in this work. The work presented in this chapter is patent pending under U.S. provisional patent application no. 67/743,882.

CHAPTER 7: CONCLUSION AND FUTURE WORK

7.1 Conclusion

The mobile wireless industry is continuously evolving, but current trends in the wireless industry are unprecedented. Advanced 4G and 5G wireless systems aim to provide wireless services that were unimaginable only a few years ago. Multi gigabit-per-second data rates, nearly ubiquitous coverage for a variety of devices, and low latency will enable a variety of advanced services for consumers as well as public safety. Two of the keys to next generation base station technology from the antenna standpoint are densification and the introduction of new frequency bands. Densification aims to increase the number of antennas thereby increasing the number of cell sites distributed throughout a given area. This reduces the amount of data each radio is required to handle effectively increasing the amount of data the network can process. The introduction of new spectrum increases the number of available channels on which data can be transmitted. Industry and academia are investigating frequencies from 3 GHz to 70 GHz for next generation wireless services.

Both densification and the introduction of new spectrum create challenges for antenna design. Fifth generation technology will not immediately replace older generation technology operating at lower frequencies so antenna systems may be requried to support frequencies from 600 MHz to 70 GHz, and in some cases, it might be desirable to have all of the antennas colocated or even integrated into the same package. In these situations, filtering will be required to minimize the effects of coupling between antennas operating in different bands. Some filtering is commonly performed at the radio, but in some cases, it may be necessary to filter closer to the antenna or in the antenna.

Even in situations where antennas covering multiple frequency bands are not colocated or integrated into the same package, the push for densification can create situations where antennas are close enough to produce interference degrading network performance. Additionally, through the deployment of DAS and small cell systems, base station antennas are being placed in closer proximity to each other as well as antenna systems for other wireless services. These additional wireless services may be licensed or unlicensed, and it can be difficult to know that interferers are present until a system is deployed. Therefore, filtering in the antenna is highly desirable to mitigate interference that may be received by the base station or to mitigate interference that the base station may cause to neighboring base stations or antenna systems for other wireless services.

To address these challenges, three antenna design approaches were presented. The first approach applied the Lagrangian formulation for metamaterials to realize a horn antenna with a reconfigurable notch filter integrated into the feed section. It was shown that by manipulation of the spacing between two SRRs, the operating freqeuncy could be changed considerably for broad-side coupled rings. On the other hand, the resonant frequency for two gap-coupled rings remained largely unchanged even with significant modification of the spacing between the rings. The Lagrangian was shown to accurately predict the location of the resonant frequency without the need to perform full-wave electromagnetic simulations implying its use as a rapid design tool for coupled resonator notch filters. The horn antenna was designed to operate from 3.95-5.8 GHz corresponding to the recommended single-mode operating range of WR-187 waveguide which covers frequency bands recently introduced for advanced 4G and 5G systems. The filter was shown to operate from ∼4-5.6 GHz depending on the spacing between the rings. This filter can be used to selectively eliminate interfering signals radiated by neighboring base stations or other wireless services. In the field these filters could be implemented as fixed or tunable modules that could be removed from the antenna to adjust the filter notch band, or the antenna could be outfitted with a motorized system to dynamically tune the filter. The specific contributions of this chapter include: a guided wave notch filter design technique using the Lagrangian formulation for metamaterials, an investigation of split ring resonator tunability with different orientations, and a horn antenna with a reconfigurable notch filter integrated into the antenna feed.

The second antenna presented in this dissertation is an extremely versatile antenna that provides the ability to reconfigure the antenna for specified bandwidths or to integrate filtering. The antenna is a directional sleeve monopole antenna designed for wide-beam azimuth coverage that is ideal for an antenna mounted to side of a building in an urban environment. The antenna is also useful in situations where the terrain or landscape creates a situation where users are only located on one side of the antenna mounting location such as the side of a mountain or along a coastline. The baseline antenna operates from 1.7-2.7 GHz where a grounded reflector and a parasitic director provide an azimuth beamwidth ranging from $\sim$140°-180°. The parasitic director also improves the elevation angle spread in -10-dB crossover which improves the uniformity in coverage area over the operating band and provides benefits if the antenna is to be mechanically tilted. To provide the ability to reconfigure the antenna, a threaded rod is soldered to the base PCB where the main radiator can be removed and reconfigured for a more narrow operating band, or the addition of filtering. Any reduction in mismatch within a radio system improves the overall system efficiency, and it is shown that a tuned main radiator can be incorporated into the antenna to provide a return loss better than 19 dB over a sub-band where this may be tailored to a particular wireless operator. The antenna also incorporates a main radiator that is modified to incorporate a broadband band reject filter for an FiA filtering approach. The filter provides a return loss better than $\sim$1.36 dB from 3.3-5.925 GHz, and shows significant gain reduction in this band. This band is chosen as it corresponds to current bands in use for 4G LTE as well as bands of interest for 5G, and the filter shows an excellent ability to minimize any possible interference from or to this band. The specific contributions of this chapter include: design of a wide-beam antenna for wireless communications, an approach to reconfigure the sleeve monopole antenna for specific operating bands, design of a broadband band stop filter based on the CLS structure, and integration of this filter into the sleeve monopole antenna with considerations for impedance matching.

The third antenna presented in this dissertation provides a unique solution that integrates millimeter wave 5G antennas into an antenna covering frequency bands in use for older generations. The low band (LB) antenna is a three-sided omnidirectional sleeve monopole operating from 1.7-2.7 GHz. The high band (HB) antennas are designed for 27.5-28.35 GHz and realized as two series-fed patch arrays arranged on each face of the three-sided sleeve of the LB antenna. With two antennas on each face, the HB forms a tri-sector MIMO system for enhanced data rates. The HB antenna operates on the same principles as traditional macro-cell antennas where each cell is broken up into segments so that more data traffic can be passed through the network; however, the antennas could be combined to form a pseudo-omnidirectional antenna if it is too costly or undesirable to deploy three millimeter wave radios at each site. Since this is a dual band system, the interaction between bands is considered where it is found that the port-to-port isolation is reasonable even without filtering in the system. Unfortunately, the LB antenna does have the ability to radiate and exhibits a decent impedance match in the HB frequency range. As a result, the antenna can radiate spurious signals that may interfere with the 5G millimeter wave system. To mitigate this, the LB antenna is configured with a defected-center coaxial filter that provides a stop band in the HB frequency range. The LB antenna is fed with strip-centered coaxial line enabling the integration of the fitler directly into the feedline of the LB antenna where the filter occupies no additional space compared to the

LB antenna without a filter so the approach could be considered FiF or FiA. The design approach for partially filled strip-centered coax is presented along with the design approach for a band reject filter exhibiting ~20% bandwidth at ~28 GHz. The specific contributions of this chapter include: an antenna integration technique to realize dual band antennas, a dual band antenna specifically designed for next generation mobile wireless systems, a defected center coaxial transmission line filter where this filter approach could be far-reaching for future base station antennas.

The antennas and design techniques presented in this dissertation advance the field of filtering antennas that will be critical for next generation mobile wireless systems. Note that the design approaches are tailored to base station systems but not limited to these systems. Any wireless system that requires filtering at or near the antenna could benefit from the design approaches in this dissertation.

7.2 Future Work

7.2.1 Lagrangian Method for Filter Design

There are several paths forward for the work presented in Chapter 4. One of the challenges faced with the implementation of the Lagrangian technique is appropriate discretization of the solution domain. The accuracy of the method is dependent upon appropriate data extraction, and it is found that inaccuracy can result if the solution domain is not properly discretized especially for close resonator spacings. This is similar to the inaccuracy that results with poor meshing in computational electromagnetics solutions. The grid dimensions found to provide accurate solutions are stated in Chapter 4. Investigation into the accuracy of the Lagrangian technique with various discretization techniques could provide valuable insight into the Lagrangian formalism for filter design.

In more practical terms, a natural extension of this work is the addition of mechanical mechanisms for dynamic tuning. Mechanical systems are common in base station antennas for tilt control where electric motors move phase shifting devices to steer the main beam. Therefore, it is feasible that a similar system could be put in place to dynamically adjust filter components to improve system performance.

It would also be worthwhile to increase the operating frequency of the waveguide and filter components to millimeter wave bands that are of interest for 5G applications. Air-filled waveguide would be best transmission line approach in terms of loss leading to maximum system efficiencies. There are commercially available waveguide components for these bands, but the filtering would be a challenge. This is especially true if dynamic tuning is added where the filter frequency is controlled mechanically.

This work can also be extended to include multiple sets of resonators for wideband and multiband filters. The ability to filter over multiple and wider bandwidths would be desirable for many wireless applications. Straightforward extensions of the design procedures presented in this chapter could be used for the design of more advanced wideband and multiband filters.

7.2.2 Wide-beam Antenna with Modular Radiator

The antenna presented in Chapter 5 is a versatile antenna for selected applications. By manipulation of the reflector and/or director, different beamwidths and even pattern shapes are possible. The antenna could also be implemented as a linear antenna array to realize narrow elevation beamwidths while maintaining wide azimuth coverage, and a beamforming network could be integrated for adaptive beam steering. This antenna would be useful to cover levels of a parking deck, the floors of open office buildings, or even sections of stadiums.

The technique presented to provide narrow band coverage could also be extended to investigate antenna configurations that provide optimized return loss in various subbands within the overall operating band. In a related investigation, various filtering methods could also be considered for narrow band notch filtering or even selective band pass filtering. Additionally, the filtering approach could be used to realize coaxial filters as the analysis in this chapter implies.

In a more general extension of this work, the method of reconfiguring the antenna could be applied to various other antenna types. This could provide the ability to reconfigure antennas or add filtering capability.

7.2.3 Dual Band 4G/5G Antenna for Next Generation Base Stations

The antenna presented in Chapter 6 is a sample of antenna systems that will be required as wireless providers migrate to high frequency 5G. One significant area of interest for 5G millimeter wave communications is the implementation of massive MIMO where large antenna arrays are used to provide narrow beams that only cover a single user or a small group of users. Theoretically this enables very high data rates, and trials have confirmed the feasability of the approach. It would be of great interest to take the antenna presented in Chapter 6, and integrate an active millimeter wave antenna array into the walls of the sleeve. There would be considerable challenges, particularly in the integration of active beamforming circuitry that maintains a low profile so that it does not interfere with the LB operation. However, the concept would draw a lot of attention within the academic community as well as the wireless industry as a whole.

Focusing on the filter design, a natural extension of this work is the integration of defected-center coaxial filters into cable-fed antenna arrays that are common in the base station industry. It is standard practice for macro-cell antenna arrays to use coaxial cable to feed between power dividers or phase shifters and the antenna elements or sub-arrays. Defected center coaxial filters could be integrated into these coaxial feed systems taking up a similar volume as the existing coaxial feed lines and potentially reduce weight over the dielectric-filled coax lines. Defected center coaxial filters could be integrated for band-stop filtering using the approach presented in Chapter 6, but other filters (band pass, low pass, or high pass) may also be possible.

7.2.4 List of Publications

The following is a list of publications and patent applications included in this dissertation where I am lead author, co-author, or inventor.

Journal publications

1. "A waveguide horn antenna with coupled resonator notch filter designed by the Lagrangian formulation for metamaterials" - Progress in Electromagnetics Research B, vol. 69, 2016
2. "A wide-beam antenna with modular main radiator" - manuscript in preparation
3. "A wide-beam ntenna with modular main radiator and integrated bandstop filter" - manuscript in preparation

Conference Publications

1. "Broadband, wide beam sleeve monopole antenna with reflector and director for pattern control" - IEEE APS/URSI 2018
2. "Sleeve monopole antenna with integrated filter for base station applications" - IEEE APS/URSI 2017
3. "X-band horn antenna with integrated tunable notch filter" - IEEE APS/URSI 2015
4. "Metamaterial measurement in a cylindrical coaxial fixture with consideration for inter-element coupling" - IEEE Radio Science Meeting 2014

Patent Applications

1. Sleeve Monopole Antenna with Spatially Variable Dielectric Loading - 15/350,984, 15/395,170, 15/981,556

2. Wide-Beam Antenna with Modular Main Radiator - 62/684,838, 62/696,538
3. Dual Band Antenna for 4G/5G Wireless Applications and a Defected Center Coaxial Filter - 67/743,882

The following is a list of selected publications not specifically included in this dissertation where I am lead or co-author.

Conference Publications

1. "Dual band, dual polarized rail mount MIMO stadium antenna" - IEEE APS/URSI 2017
2. "Electrically thin magnetodielectric metamaterial fresnel lens Antenna" - IEEE APS/URSI 2016
3. "A coaxial test fixture for transmission/reflection measurements of metamaterials" - IEEE APS/URSI 2013
4. "Permeability and permittivity extraction issues for non-Foster and active metamaterials" - IEEE APS/URSI 2013
5. "Capacitance and bandwidth trade-offs in a cross-coupled CMOS negative capacitor" - IEEE SoutheastCon 2013

REFERENCES

[1] Z. N. Chen and K.-M. Luk, *Antennas for base stations in wireless communications.* McGraw Hill Professional, 2009.

[2] 4G Americas, "Mimo and smart antennas for mobile broadband systems." White Paper, 2012.

[3] T. S. Rappaport, S. Sun, R. Mayzus, H. Zhao, Y. Azar, K. Wang, G. N. Wong, J. K. Schulz, M. Samimi, and F. Gutierrez, "Millimeter wave mobile communications for 5g cellular: It will work!," *IEEE Access*, vol. 1, pp. 335–349, 2013.

[4] T. Mshvidobadze, "Evolution mobile wireless communication and lte networks," in *2012 6th International Conference on Application of Information and Communication Technologies (AICT)*, pp. 1–7, Oct 2012.

[5] J. R. Hampton, *Introduction to MIMO communications.* Cambridge university press, 2014.

[6] T. Nakamura, S. Nagata, A. Benjebbour, Y. Kishiyama, T. Hai, S. Xiaodong, Y. Ning, and L. Nan, "Trends in small cell enhancements in lte advanced," *IEEE Communications Magazine*, vol. 51, pp. 98–105, February 2013.

[7] Rysavy Research, "Lte and 5g innovation: Igniting mobile broadband." White Paper, 2015.

[8] 4G Americas, "5g technology evolution recommendations." White Paper, 2015.

[9] R. Butler, I. Timofeev, and M. Zimmerman, "Broadband multiband phased array antennas for cellular communications," in *2016 International Symposium on Antennas and Propagation (ISAP)*, pp. 160–161, Oct 2016.

[10] V. Golikov, S. Hienonen, and P. Vainikainen, "Effect of impedance loading at higher harmonics on passive intermodulation in antennas," in *IEEE Antennas and Propagation Society International Symposium. Digest. Held in conjunction with: USNC/CNC/URSI North American Radio Sci. Meeting (Cat. No.03CH37450)*, vol. 4, pp. 378–381 vol.4, June 2003.

[11] A. Christianson, J. Henrie, and W. Chappell, "Matching network design for passive intermodulation distortion reduction," in *2013 IEEE Antennas and Propagation Society International Symposium (APSURSI)*, pp. 2247–2248, July 2013.

[12] Z. Shi-quan, W. Qin-dong, L. Jin-tao, and G. De-biao, "Analysis of passive intermodulation interference in gsm mobile communication antennas," in *2007 International Symposium on Microwave, Antenna, Propagation and EMC Technologies for Wireless Communications*, pp. 1251–1254, Aug 2007.

[13] BASTA, "Recommendation on base station antenna standards." White Paper - BASTA, 2013.

[14] R. C. Hansen, *Phased array antennas*, vol. 213. John Wiley & Sons, 2009.

[15] D. L. Runyon, J. E. Thompson Jr, and J. C. Carson, "Dual polarized array antenna," May 23 2000. US Patent 6,067,053.

[16] J. R. Ippolito, H. Villegas, and J. S. Wilson, "Base station antenna for dual polarization," June 6 2000. US Patent 6,072,439.

[17] J. S. Wilson, H. W. Davis, P. J. Bisiules, C. A. Bibblecom, L. S. Racana, and D. J. Ulery, "Dual polarized based station antenna," Mar. 7 2000. US Patent 6,034,649.

[18] J. C. Carson and S. Phillips, "Method and system for producing dual polarization states with controlled rf beamwidths," Oct. 8 2002. US Patent 6,462,710.

[19] K. Raoof, M. B. Zid, N. Prayongpun, and A. Bouallegue, *Advanced MIMO techniques: Polarization diversity and antenna selection*. InTech, 2011.

[20] L. Zheng and D. N. C. Tse, "Diversity and multiplexing: a fundamental tradeoff in multiple-antenna channels," *IEEE Transactions on Information Theory*, vol. 49, pp. 1073–1096, May 2003.

[21] F. Rusek, D. Persson, B. K. Lau, E. G. Larsson, T. L. Marzetta, O. Edfors, and F. Tufvesson, "Scaling up mimo: Opportunities and challenges with very large arrays," *IEEE Signal Processing Magazine*, vol. 30, pp. 40–60, Jan 2013.

[22] A. J. PAULRAJ, D. A. GORE, R. U. NABAR, and H. BOLCSKEI, "An overview of mimo communications - a key to gigabit wireless," *Proceedings of the IEEE*, vol. 92, pp. 198–218, Feb 2004.

[23] H. Huang, Y. Liu, and S. Gong, "A novel dual-broadband and dual-polarized antenna for 2g/3g/lte base stations," *IEEE Transactions on Antennas and Propagation*, vol. 64, no. 9, pp. 4113–4118, 2016.

[24] M. Göttl, R. Gabriel, and G. Klinger, "Dual polarized multi-range antenna," Dec. 25 2001. US Patent 6,333,720.

[25] R. Li, T. Wu, B. Pan, K. Lim, J. Laskar, and M. M. Tentzeris, "Equivalent-circuit analysis of a broadband printed dipole with adjusted integrated balun and an array for base station applications," *IEEE Transactions on Antennas and Propagation*, vol. 57, no. 7, pp. 2180–2184, 2009.

[26] X. Quan and R. Li, "A broadband dual-polarized omnidirectional antenna for base stations," *IEEE Transactions on Antennas and Propagation*, vol. 61, no. 2, pp. 943–947, 2013.

[27] A. D. Khaleel, M. F. bin Mansor, N. Misran, and M. T. Islam, "Omnidirectional dielectric resonator antenna for lte femtocell base stations," in *2015 International Conference on Space Science and Communication (IconSpace)*, pp. 509–512, Aug 2015.

[28] P. Kumsalee, P. Kamphikul, P. Krachodnok, and R. Wongsan, "Omnidirectional high-gain wide slot antenna array for mobile phone base station," in *2014 11th International Conference on Electrical Engineering/Electronics, Computer, Telecommunications and Information Technology (ECTI-CON)*, pp. 1–4, May 2014.

[29] Y. Xiaole, N. Daning, and W. Wutu, "An omnidirectional high-gain antenna element for td-scdma base station," in *2006 7th International Symposium on Antennas, Propagation EM Theory*, pp. 1–4, Oct 2006.

[30] B. Wang, F.-S. Zhang, L. Jiang, Q. Li, and J. Ren, "A broadband omnidirectional antenna array for base station," *Progress In Electromagnetics Research C*, vol. 54, pp. 95–101, 2014.

[31] Y. Li, X.-D. Yang, C.-Y. Liu, and T. Jiang, "A sleeve monopole antenna with wide impedance bandwidth for indoor base station applications," *Progress In Electromagnetics Research C*, vol. 16, pp. 223–232, 2010.

[32] Y. Li, Z.-Y. Zhang, Q.-Q. Liu, Y.-X. Zhang, and G. Fu, "A novel wideband sleeve antenna with capacitive annulus for wireless communication applications," *Progress In Electromagnetics Research C*, vol. 52, pp. 1–6, 2014.

[33] P. Huang, Q. Guo, Z.-Y. Zhang, Y. Li, and G. Fu, "Design of a wideband sleeve antenna with symmetrical ridges," *Progress In Electromagnetics Research Letters*, vol. 55, pp. 137–143, 2015.

[34] Y. Yu, H. Zhang, and Z. Chen, "A broadband dual-polarized omnidirectional mimo antenna for 4g lte applications," *Progress In Electromagnetics Research Letters*, vol. 57, pp. 91–96, 2015.

[35] Rysavy Research, "Mobile broadband transformation lte to 5g." White Paper, 2016.

[36] P. Schulz, M. Matthe, H. Klessig, M. Simsek, G. Fettweis, J. Ansari, S. A. Ashraf, B. Almeroth, J. Voigt, I. Riedel, A. Puschmann, A. Mitschele-Thiel, M. Muller, T. Elste, and M. Windisch, "Latency critical iot applications in 5g: Perspective on the design of radio interface and network architecture," *IEEE Communications Magazine*, vol. 55, pp. 70–78, February 2017.

[37] B. Lathi and Z. Ding, *Modern Digital and Analog Communication Systems*. Oxford university press, 2009.

[38] 4G Americas, "5g spectrum recommendations." White Paper, 2015.

[39] C. A. Balanis, "Antenna theory: Analysis and design; 2005; 1136 pages; ; isbn 047166782x."

[40] F. E. Idachaba, "5g networks: Open network architecture and densification strategies for beyond 1000x network capacity increase," in *2016 Future Technologies Conference (FTC)*, pp. 1265–1269, Dec 2016.

[41] B. Romanous, N. Bitar, A. Imran, and H. Refai, "Network densification: Challenges and opportunities in enabling 5g," in *2015 IEEE 20th International Workshop on Computer Aided Modelling and Design of Communication Links and Networks (CAMAD)*, pp. 129–134, Sept 2015.

[42] N. Bhushan, J. Li, D. Malladi, R. Gilmore, D. Brenner, A. Damnjanovic, R. T. Sukhavasi, C. Patel, and S. Geirhofer, "Network densification: the dominant theme for wireless evolution into 5g," *IEEE Communications Magazine*, vol. 52, pp. 82–89, February 2014.

[43] W. Zhou and T. Arslan, "A bidirectional planar monopole antenna array for wifi/bluetooth and lte mobile applications," in *2013 Loughborough Antennas Propagation Conference (LAPC)*, pp. 190–193, Nov 2013.

[44] B. Rohani, K. Takahashi, H. Arai, Y. Kimura, and T. Ihara, "Improving channel capacity in indoor 4×4 mimo base station utilizing small bidirectional antenna," *IEEE Transactions on Antennas and Propagation*, vol. 66, pp. 393–400, Jan 2018.

[45] Y. Zhao, K. Wei, Z. Zhang, and Z. Feng, "A waveguide antenna with bidirectional circular polarizations of the same sense," *IEEE Antennas and Wireless Propagation Letters*, vol. 12, pp. 559–562, 2013.

[46] L. Liu, Z. Zhang, Z. Tian, and Z. Feng, "A bidirectional endfire array with compact antenna elements for coal mine/tunnel communication," *IEEE Antennas and Wireless Propagation Letters*, vol. 11, pp. 342–345, 2012.

[47] J. B. Pendry, A. J. Holden, D. Robbins, and W. Stewart, "Magnetism from conductors and enhanced nonlinear phenomena," *IEEE transactions on microwave theory and techniques*, vol. 47, no. 11, pp. 2075–2084, 1999.

[48] A. Alù, N. Engheta, A. Erentok, and R. W. Ziolkowski, "Single-negative, double-negative, and low-index metamaterials and their electromagnetic applications," *IEEE Antennas and Propagation Magazine*, vol. 49, no. 1, pp. 23–36, 2007.

[49] R. A. Shelby, D. R. Smith, and S. Schultz, "Experimental verification of a negative index of refraction," *science*, vol. 292, no. 5514, pp. 77–79, 2001.

[50] R. W. Ziolkowski, "Design, fabrication, and testing of double negative metamaterials," *IEEE Transactions on antennas and Propagation*, vol. 51, no. 7, pp. 1516–1529, 2003.

[51] N. Engheta and R. W. Ziolkowski, *Metamaterials: physics and engineering explorations*. John Wiley & Sons, 2006.

[52] L. Solymar and E. Shamonina, *Waves in metamaterials.* Oxford University Press, 2009.

[53] D. Pozar, *Microwave Engineering.* Wiley, 2004.

[54] G. Matthaei, L. Young, and E. Jones, "Microwave filters, impedance-matching networks, and coupling structures (artech microwave library)," *Artech House, February*, 1980.

[55] C. A. Balanis, "Advanced engineering electromagnetics. 1989," *ed: John Wiley & Sons.*

[56] L. D. Landau and E. Lifshitz, *Course of Theoretical Physics. Vol. 8: Electrodynamics of Continuous Media.* Oxford, 1960.

[57] V. G. Veselago, "The electrodynamics of substances with simultaneously negative values of and μ," *Soviet physics uspekhi*, vol. 10, no. 4, p. 509, 1968.

[58] D. Schurig, J. Mock, and D. Smith, "Electric-field-coupled resonators for negative permittivity metamaterials," *Applied Physics Letters*, vol. 88, no. 4, p. 041109, 2006.

[59] T. P. Weldon, K. Miehle, R. S. Adams, and K. Daneshvar, "A wideband microwave double-negative metamaterial with non-foster loading," in *2012 Proceedings of IEEE Southeastcon*, pp. 1–5, March 2012.

[60] T. P. Weldon, R. S. Adams, and R. K. Mulagada, "A novel unit cell and analysis for epsilon negative metamaterial," in *Southeastcon, 2011 Proceedings of IEEE*, pp. 211–214, IEEE, 2011.

[61] M. Palandoken, *Metamaterial-Based Compact Filter Design.* INTECH Open Access Publisher, 2012.

[62] L. Solymar and E. Shamonina, *Waves in metamaterials.* Oxford University Press, 2009.

[63] S. Fallahzadeh, H. Bahrami, and M. Tayarani, "A novel dual-band bandstop waveguide filter using split ring resonators," *Progress In Electromagnetics Research Letters*, vol. 12, pp. 133–139, 2009.

[64] S. H. Gangaraj and M. Tayarani, "A novel bandstop resonator in waveguide and its application for suppressing the spurious responses with new advantages to typical resonators," in *PIERS Proceedings*, pp. 533–537.

[65] M. Barbuto, F. Trotta, F. Bilotti, and A. Toscano, "Horn antennas with integrated notch filters," *IEEE Transactions on Antennas and Propagation*, vol. 63, no. 2, pp. 781–785, 2015.

[66] M. Barbuto, F. Trotta, F. Bilotti, and A. Toscano, "Varying the operation bandwidth of metamaterial-inspired filtering modules for horn antennas," *Progress In Electromagnetics Research C*, vol. 58, pp. 61–68, 2015.

[67] V. V. Yem, P. V. Chi, and B. Journet, "Novel mimo antenna using complementary split ring resonator(csrr) for lte applications," in *The 2012 International Conference on Advanced Technologies for Communications*, pp. 222–226, Oct 2012.

[68] C.-C. Lin, P. Jin, and R. W. Ziolkowski, "Single, dual and tri-band-notched ultrawideband (uwb) antennas using capacitively loaded loop (cll) resonators," *IEEE Transactions on Antennas and Propagation*, vol. 60, no. 1, pp. 102–109, 2012.

[69] S. Biswas, D. Guha, and C. Kumar, "Control of higher harmonics and their radiations in microstrip antennas using compact defected ground structures," *IEEE Transactions on Antennas and Propagation*, vol. 61, pp. 3349–3353, June 2013.

[70] A. A. Ibrahim, M. A. Abdalla, and A. B. Abdel-Rahman, "Wireless bandpass filters build on metamaterials," 2018.

[71] A. Loureiro, D. Gallegos, and G. Caldwell, "Interference analysis on umts-2100 co-existence with gsm-1900," in *2011 IEEE Vehicular Technology Conference (VTC Fall)*, pp. 1–4, Sept 2011.

[72] L.-M. Si and X. Lv, "Cpw-fed multi-band omni-directional planar microstrip antenna using composite metamaterial resonators for wireless communications," *Progress In Electromagnetics Research*, vol. 83, pp. 133–146, 2008.

[73] M. Yazdi and N. Komjani, "Design of a band-notched uwb monopole antenna by means of an ebg structure," *IEEE Antennas and Wireless Propagation Letters*, vol. 10, pp. 170–173, 2011.

[74] H. Huang, Y. Liu, and S. Gong, "A broadband dual-polarized base station antenna with anti-interference capability," *IEEE Antennas and Wireless Propagation Letters*, vol. 16, pp. 613–616, 2017.

[75] C. Mao, S. Gao, Y. Wang, and Z. Cheng, "Filtering antenna with two-octave harmonic suppression," *IEEE Antennas and Wireless Propagation Letters*, vol. 16, pp. 1361–1364, 2017.

[76] C. Lee, J. Wu, C. G. Hsu, H. Chan, and H. Chen, "Balanced band-notched uwb filtering circular patch antenna with common-mode suppression," *IEEE Antennas and Wireless Propagation Letters*, vol. 16, pp. 2812–2815, 2017.

[77] L. Inclan-Sanchez, J. Vazquez-Roy, and E. Rajo-Iglesias, "Proximity coupled microstrip patch antenna with reduced harmonic radiation," *IEEE Transactions on Antennas and Propagation*, vol. 57, pp. 27–32, Jan 2009.

[78] M. S. Ghaffarian and G. Moradi, “A novel harmonic suppressed coplanar waveguide (cpw)-fed slot antenna,” *IEEE Antennas and Wireless Propagation Letters*, vol. 10, pp. 788–791, 2011.

[79] C. Mao, S. Gao, Y. Wang, Z. Wang, F. Qin, B. Sanz-Izquierdo, and Q. Chu, “An integrated filtering antenna array with high selectivity and harmonics suppression,” *IEEE Transactions on Microwave Theory and Techniques*, vol. 64, pp. 1798–1805, June 2016.

[80] C. X. Mao, S. Gao, Y. Wang, B. Sanz-Izquierdo, Z. Wang, F. Qin, Q. X. Chu, J. Li, G. Wei, and J. Xu, “Dual-band patch antenna with filtering performance and harmonic suppression,” *IEEE Transactions on Antennas and Propagation*, vol. 64, pp. 4074–4077, Sept 2016.

[81] J. Zhang, L. Zhu, Q. Wu, N. Liu, and W. Wu, “A compact microstrip-fed patch antenna with enhanced bandwidth and harmonic suppression,” *IEEE Transactions on Antennas and Propagation*, vol. 64, pp. 5030–5037, Dec 2016.

[82] R. Li and P. Gao, “Design of a uwb filtering antenna with defected ground structure,” *Progress in Electromagnetics Research Letters*, vol. 63, pp. 65–70, 2016.

[83] M. A. Abdalla and A. Fouad, “Integrated filtering antenna based on d-crlh transmission lines for ultra-compact wireless applications,” *Progress in Electromagnetics Research C*, vol. 66, pp. 29–38, 2016.

[84] M. Troubat, S. Bila, M. Thevenot, D. Baillargeat, T. Monediere, S. Verdeyme, and B. Jecko, “Mutual synthesis of combined microwave circuits applied to the design of a filter-antenna subsystem,” *IEEE Transactions on Microwave Theory and Techniques*, vol. 55, pp. 1182–1189, June 2007.

[85] O. A. Nova, J. C. Bohorquez, N. M. Pena, G. E. Bridges, L. Shafai, and C. Shafai, “Filter-antenna module using substrate integrated waveguide cavities,” *IEEE Antennas and Wireless Propagation Letters*, vol. 10, pp. 59–62, 2011.

[86] Y. Yusuf, H. Cheng, and X. Gong, “A seamless integration of 3-d vertical filters with highly efficient slot antennas,” *IEEE Transactions on Antennas and Propagation*, vol. 59, pp. 4016–4022, Nov 2011.

[87] W. Wu, Y. Yin, S. Zuo, Z. Zhang, and J. Xie, “A new compact filter-antenna for modern wireless communication systems,” *IEEE Antennas and Wireless Propagation Letters*, vol. 10, pp. 1131–1134, 2011.

[88] Y. Lee, J. Tarng, and S. Chung, “A filtering diplexing antenna for dual-band operation with similar radiation patterns and low cross-polarization levels,” *IEEE Antennas and Wireless Propagation Letters*, vol. 16, pp. 58–61, 2017.

[89] H. Hu, F. Chen, and Q. Chu, “Novel broadband filtering slotline antennas excited by multimode resonators,” *IEEE Antennas and Wireless Propagation Letters*, vol. 16, pp. 489–492, 2017.

[90] C. Lee, H. Chen, W. Shih, and C. G. Hsu, “Balanced wideband filtering planar inverted-f antenna design,” *IEEE Antennas and Wireless Propagation Letters*, vol. 16, pp. 716–719, 2017.

[91] F. Chen, H. Hu, R. Li, Q. Chu, and M. J. Lancaster, “Design of filtering microstrip antenna array with reduced sidelobe level,” *IEEE Transactions on Antennas and Propagation*, vol. 65, pp. 903–908, Feb 2017.

[92] C. Mao, S. Gao, Y. Wang, Q. Luo, and Q. Chu, “A shared-aperture dual-band dual-polarized filtering-antenna-array with improved frequency response,” *IEEE Transactions on Antennas and Propagation*, vol. 65, pp. 1836–1844, April 2017.

[93] B. J. Xiang, S. Y. Zheng, Y. M. Pan, and Y. X. Li, “Wideband circularly polarized dielectric resonator antenna with bandpass filtering and wide harmonics suppression response,” *IEEE Transactions on Antennas and Propagation*, vol. 65, pp. 2096–2101, April 2017.

[94] R. H. Mahmud and M. J. Lancaster, “High-gain and wide-bandwidth filtering planar antenna array-based solely on resonators,” *IEEE Transactions on Antennas and Propagation*, vol. 65, pp. 2367–2375, May 2017.

[95] X. Lin, Z. Xie, P. Zhang, and Y. Zhang, “A broadband filtering duplex patch antenna with high isolation,” *IEEE Antennas and Wireless Propagation Letters*, vol. 16, pp. 1937–1940, 2017.

[96] F. Chen, J. Chen, Q. Chu, and M. J. Lancaster, “X-band waveguide filtering antenna array with nonuniform feed structure,” *IEEE Transactions on Microwave Theory and Techniques*, vol. 65, pp. 4843–4850, Dec 2017.

[97] H. Hu, F. Chen, J. Qian, and Q. Chu, “A differential filtering microstrip antenna array with intrinsic common-mode rejection,” *IEEE Transactions on Antennas and Propagation*, vol. 65, pp. 7361–7365, Dec 2017.

[98] J. Deng, S. Hou, L. Zhao, and L. Guo, “A reconfigurable filtering antenna with integrated bandpass filters for uwb/wlan applications,” *IEEE Transactions on Antennas and Propagation*, vol. 66, pp. 401–404, Jan 2018.

[99] J. Deng, S. Hou, L. Zhao, and L. Guo, “Wideband-to-narrowband tunable monopole antenna with integrated bandpass filters for uwb/wlan applications,” *IEEE Antennas and Wireless Propagation Letters*, vol. 16, pp. 2734–2737, 2017.

[100] A. H. Ramadan, J. Costantine, M. Al-Husseini, K. Y. Kabalan, Y. Tawk, and C. G. Christodoulou, “Tunable filter-antennas for cognitive radio applications,” *Progress in Electromagnetics Research B*, vol. 66, pp. 29–38, 2016.

[101] S. Barbarino and F. Consoli, “Uwb circular slot antenna provided with an inverted-l notch filter for the 5 ghz wlan band,” *Progress in Electromagnetics Research*, vol. 104, pp. 1–13, 2010.

[102] J. Tao and Q. Feng, “Compact uwb band-notch mimo antenna with embedded antenna element for improved band notch filtering,” *Progress in Electromagnetics Research C*, vol. 67, pp. 117–125, 2016.

[103] A. Alhegazi, Z. Zakaria, N. A. Shairi, I. M. Ibrahim, and S. Ahmed, “A novel reconfigurable uwb filtering-antenna with dual sharp band notches using double split ring resonators,” *Progress In Electromagnetics Research*, vol. 79, pp. 185–198, 2017.

[104] Z. H. Hu, J. R. Kelly, P. S. Hall, and P. Gardner, “Wideband conical monopole antenna with integrated stopband filter,” *Progress In Electromagnetics Research*, vol. 27, pp. 223–238, 2012.

[105] J.-B. Jiang, Z.-H. Yan, and C. Wang, “A novel compact uwb notch-filter antenna with a dual-y-shaped slot,” *Progress In Electromagnetics Research*, vol. 14, pp. 165–170, 2010.

[106] X.-C. Yin, C.-L. Ruan, C.-Y. Ding, and J.-H. Chu, “A compact ultra-wideband microstrip antenna with multiple notches,” *Progress In Electromagnetics Research*, vol. 84, pp. 321–332, 2008.

[107] P. Tilanthe, P. C. Sharma, and T. Bandopadhyay, “A compact uwb antenna with dual band rejection,” *Progress In Electromagnetics Research*, vol. 35, pp. 389–405, 2011.

[108] S. W. Wong, T. G. Huang, C. X. Mao, Z. N. Chen, and Q. X. Chu, “Planar filtering ultra-wideband (uwb) antenna with shorting pins,” *IEEE Transactions on Antennas and Propagation*, vol. 61, pp. 948–953, Feb 2013.

[109] H. Kim, K. S. Hwang, K. Chang, and Y. J. Yoon, “Novel slot antennas for harmonic suppression,” *IEEE Microwave and Wireless Components Letters*, vol. 14, pp. 286–288, June 2004.

[110] H. Liu, Z. Li, X. Sun, and J. Mao, “Harmonic suppression with photonic bandgap and defected ground structure for a microstrip patch antenna,” *IEEE Microwave and Wireless Components Letters*, vol. 15, pp. 55–56, Feb 2005.

[111] H. Kim and Y. J. Yoon, “Microstrip-fed slot antennas with suppressed harmonics,” *IEEE Transactions on Antennas and Propagation*, vol. 53, pp. 2809–2817, Sept 2005.

[112] N. Nguyen, R. Ahmad, Y. Im, Y. Shin, and S. Park, “A t-shaped wide-slot harmonic suppression antenna,” *IEEE Antennas and Wireless Propagation Letters*, vol. 6, pp. 647–650, 2007.

[113] C. Sim, M. Chang, and B. Chen, “Microstrip-fed ring slot antenna design with wideband harmonic suppression,” *IEEE Transactions on Antennas and Propagation*, vol. 62, pp. 4828–4832, Sept 2014.

[114] L. Yang, P. Cheong, L. Han, W. Choi, K. Tam, and K. Wu, “Miniaturized parallel coupled-line filter-antenna with spurious response suppression,” *IEEE Antennas and Wireless Propagation Letters*, vol. 10, pp. 726–729, 2011.

[115] A. J. Martinez-Ros, J. L. Gomez-Tornero, and G. Goussetis, “Multifunctional angular bandpass filter siw leaky-wave antenna,” *IEEE Antennas and Wireless Propagation Letters*, vol. 16, pp. 936–939, 2017.

[116] T. L. Wu, Y. M. Pan, P. F. Hu, and S. Y. Zheng, “Design of a low profile and compact omnidirectional filtering patch antenna,” *IEEE Access*, vol. 5, pp. 1083–1089, 2017.

[117] Y. Zhang, X. Y. Zhang, and Y. Pan, “Compact single- and dual-band filtering patch antenna arrays using novel feeding scheme,” *IEEE Transactions on Antennas and Propagation*, vol. 65, pp. 4057–4066, Aug 2017.

[118] T. L. Wu, Y. M. Pan, and P. F. Hu, “Wideband omnidirectional slotted patch antenna with filtering response,” *IEEE Access*, vol. 5, pp. 26015–26021, 2017.

[119] D. Kwiatkowski, “Providing wireless service at a venue using horn antennas,” Aug. 21 2014. US Patent App. 14/465,121.

[120] J. W. Shehan and R. S. Adams, “X-band horn antenna with integrated tunable notch filter,” in *Antennas and Propagation & USNC/URSI National Radio Science Meeting, 2015 IEEE International Symposium on*, pp. 2213–2214, IEEE, 2015.

[121] J. W. Shehan and R. S. Adams, “A waveguide horn antenna with coupled resonator notch filter designed by the lagrangian formulation for metamaterials,” *Progress In Electromagnetics Research B*, vol. 69, pp. 17–29, 2016.

[122] D. A. Powell, M. Lapine, M. V. Gorkunov, I. V. Shadrivov, and Y. S. Kivshar, “Metamaterial tuning by manipulation of near-field interaction,” *Physical Review B*, vol. 82, no. 15, p. 155128, 2010.

[123] D. A. Powell, K. Hannam, I. V. Shadrivov, and Y. S. Kivshar, “Near-field interaction of twisted split-ring resonators,” *Physical Review B*, vol. 83, no. 23, p. 235420, 2011.

[124] W. Withayachumnankul, C. Fumeaux, and D. Abbott, “Near-field interactions in electric inductive–capacitive resonators for metamaterials,” *Journal of Physics D: Applied Physics*, vol. 45, no. 48, p. 485101, 2012.

[125] J. W. Shehan, R. S. Adams, and T. P. Weldon, "Metamaterial measurement in a cylindrical coaxial fixture with consideration for inter-element coupling," in *Radio Science Meeting (Joint with AP-S Symposium), 2014 USNC-URSI*, pp. 138–138, IEEE, 2014.

[126] H. A. Haus and W. Huang, "Coupled-mode theory," *Proceedings of the IEEE*, vol. 79, no. 10, pp. 1505–1518, 1991.

[127] Nasimuddin, Y. S. Anjani, and A. Alphones, "A wide-beam circularly polarized asymmetric-microstrip antenna," *IEEE Transactions on Antennas and Propagation*, vol. 63, pp. 3764–3768, Aug 2015.

[128] K. Ding, Y. Wang, and X. Xiong, "A novel wide-beam circularly polarized antenna for sdars applications," *IEEE Antennas and Wireless Propagation Letters*, vol. 11, pp. 811–813, 2012.

[129] Y. Wen, B. Wang, and X. Ding, "Wide-beam circularly polarized microstrip magnetic-electric dipole antenna for wide-angle scanning phased array," *IEEE Antennas and Wireless Propagation Letters*, vol. 16, pp. 428–431, 2017.

[130] Z. Pan, W. Lin, and Q. Chu, "Compact wide-beam circularly-polarized microstrip antenna with a parasitic ring for cnss application," *IEEE Transactions on Antennas and Propagation*, vol. 62, pp. 2847–2850, May 2014.

[131] S. X. Ta and I. Park, "Crossed dipole loaded with magneto-electric dipole for wideband and wide-beam circularly polarized radiation," *IEEE Antennas and Wireless Propagation Letters*, vol. 14, pp. 358–361, 2015.

[132] L. Sun, B.-H. Sun, H. Wu, J. Yuan, and W. Tang, "Broadband, wide beam circularly polarized antenna with a novel matching structure for satellite communications," *Progress In Electromagnetics Research*, vol. 59, pp. 159–166, 2015.

[133] G. Yang, J. Li, S. G. Zhou, and Y. Qi, "A wide-angle e-plane scanning linear array antenna with wide beam elements," *IEEE Antennas and Wireless Propagation Letters*, vol. 16, pp. 2923–2926, 2017.

[134] Y. Wen, B. Wang, and X. Ding, "Wide-beam siw-slot antenna for wide-angle scanning phased array," *IEEE Antennas and Wireless Propagation Letters*, vol. 15, pp. 1638–1641, 2016.

[135] Y. Cheng, X. Ding, W. Shao, M. Yu, and B. Wang, "2-d planar wide-angle scanning-phased array based on wide-beam elements," *IEEE Antennas and Wireless Propagation Letters*, vol. 16, pp. 876–879, 2017.

[136] J. Wang, L. Zhou, and W. Chen, "A novel wide beam uwb antenna," in *2010 International Conference on Microwave and Millimeter Wave Technology*, pp. 961–964, May 2010.

[137] Y. He, W. Wang, H. Yang, and X. Du, "Improved design of a broadband dielectric resonator antenna with wide beam," *International Journal of Antennas and Propagation*, vol. 2018, p. 7, 2018.

[138] R. Wang, B.-Z. Wang, C. Hu, C. Gong, and X. Ding, "Low-profile on-board antenna with a broad beam based on three-current model," *Progress in Electromagnetics Research*, vol. 156, pp. 13–24, 2016.

[139] Y. Xu, S. Gong, and T. Hong, "Circularly polarized slot microstrip antenna for harmonic suppression," *IEEE Antennas and Wireless Propagation Letters*, vol. 12, pp. 472–475, 2013.

[140] S. i. Kwak, J. H. Kwon, D. Sim, K. Chang, and Y. J. Yoon, "Design of the printed slot antenna using wiggly line with harmonic suppression," *IEEE Antennas and Wireless Propagation Letters*, vol. 9, pp. 741–743, 2010.

[141] Y. Liu, Y. Lu, and P. Hsu, "Harmonic suppressed slot loop antenna fed by coplanar waveguide," *IEEE Antennas and Wireless Propagation Letters*, vol. 13, pp. 1292–1295, 2014.

[142] Y. J. Sung and Y. . Kim, "An improved design of microstrip patch antennas using photonic bandgap structure," *IEEE Transactions on Antennas and Propagation*, vol. 53, pp. 1799–1804, May 2005.

[143] Y.-Y. Gao, X. Yang, C. Jiang, and J.-Y. Zhou, "A circularly polarized rectenna with low profile for wireless power transmission," *Progress in Electromagnetics Research Letters*, vol. 13, pp. 41–49, 2010.

[144] P. Dixon, "Cavity-resonance dampening," *IEEE Microwave Magazine*, vol. 6, pp. 74–84, June 2005.

[145] J. W. Shehan and R. S. Adams, "Sleeve monopole antenna with integrated filter for base station applications," in *2017 USNC-URSI Radio Science Meeting (Joint with AP-S Symposium)*, pp. 11–12, July 2017.

[146] J. Zhang, M. Y. Koledintseva, J. L. Drewniak, G. Antonini, and A. Orlandi, "Extracting r, l, g, c parameters of dispersive planar transmission lines from measured s-parameters using a genetic algorithm," in *2004 International Symposium on Electromagnetic Compatibility (IEEE Cat. No.04CH37559)*, vol. 2, pp. 572–576 vol.2, Aug 2004.

[147] M. Z. Joozdani and M. K. Amirhosseini, "Equivalent circuit model for the frequency-selective surface embedded in a layer with constant conductivity," *IEEE Transactions on Antennas and Propagation*, vol. 65, pp. 705–712, Feb 2017.

[148] M. Khalily, R. Tafazolli, T. A. Rahman, and M. R. Kamarudin, "Design of phased arrays of series-fed patch antennas with reduced number of the controllers for 28-ghz mm-wave applications," *IEEE Antennas and Wireless Propagation Letters*, vol. 15, pp. 1305–1308, 2016.

[149] H. Tsutsumi, Y. Kuwahara, and H. Kamo, "Design of the series fed microstrip patch planar array antenna by the parato genetic algorithm," in *2015 IEEE International Symposium on Antennas and Propagation USNC/URSI National Radio Science Meeting*, pp. 1854–1855, July 2015.

[150] A. Omar, S. Al-Saif, M. A. Ashraf, and S. Alshebeili, "Design and analysis of millimeter wave series fed microstrip patch array for next generation wireless communication systems," in *2016 17th International Symposium on Antenna Technology and Applied Electromagnetics (ANTEM)*, pp. 1–2, July 2016.

[151] W. Wei and X. Wang, "A 77 ghz series fed weighted antenna arrays with suppressed sidelobes in e-and h-plane," *Progress In Electromagnetics Research*, vol. 72, pp. 23–28, 2018.

[152] J. Thaysen and K. B. Jakobsen, "Envelope correlation in (n, n) mimo antenna array from scattering parameters," *Microwave and optical technology letters*, vol. 48, no. 5, pp. 832–834, 2006.

[153] I. Salonen and P. Vainikainen, "Estimation of signal correlation in antenna arrays," in *Proc. JINA*, vol. 2, pp. 383–386, 2002.

[154] H. Zhang, Z. Wang, J. Yu, and J. Huang, "A compact mimo antenna for wireless communication," *IEEE Antennas and Propagation Magazine*, vol. 50, pp. 104–107, Dec 2008.

[155] B. C. Wadell, *Transmission line design handbook.* Artech House, 1991.

[156] R. Collier, *Transmission lines: Equivalent circuits, electromagnetic theory, and photons.* Cambridge University Press, 2013.

[157] D.-J. Woo, T.-K. Lee, J.-W. Lee, C.-S. Pyo, and W.-K. Choi, "Novel u-slot and v-slot dgss for bandstop filter with improved q factor," *IEEE Transactions on Microwave Theory and Techniques*, vol. 54, pp. 2840–2847, June 2006.

[158] J. A. Tirado-Mendez, H. Jardon-Aguilar, R. Flores-Leal, E. A. Andrade-Gonzalez, and F. Iturbide-Sanchez, "Improving frequency response of microstrip filters using defected ground and defected microstrip structures," *Progress in electromagnetics research*, vol. 13, pp. 77–90, 2010.

[159] J. Wang, H. Ning, Q. Xiong, M. Li, and L.-F. Mao, "A novel miniaturized dual-band bandstop filter using dual-plane defected structures," *Progress In Electromagnetics Research*, vol. 134, pp. 397–417, 2013.

APPENDIX A: LAGRANGIAN FORMULATION FOR METAMATERIALS

The Lagrangian formulation for metamaterials is presented by Powell, et. al. in [122] as a method to predict resonant frequency shifting in the presence of coupling. The method is developed for coupling between two identical resonators, and an approach for the extension of this method to non-identical resonators is given here. The Lagrangian is written as

$$\mathcal{L} = T - V \tag{A.1}$$

where T is the kinetic energy and V is the potential energy. For resonant electromagnetic elements, the charge and current can be written as separated functions of time and space, and letting $I(t) = \dot{Q}(t)$ satisfies the continuity equation. Therefore, the Lagrangian can be written as

$$\mathcal{L} = A\dot{Q}^2 - BQ^2 \tag{A.2}$$

where the first term is basically the magnetic energy and the second term is the electric energy. The Euler-Lagrange equation of motion reveals the simple harmonic oscillator equation

$$\ddot{Q} + \frac{B}{A}Q = 0 \tag{A.3}$$

where the resonant frequency is given by $\omega_0 = \sqrt{B/A}$ so that A and B can be related to the inductance and capacitance of the resonator, respectively. Note that a $e^{j\omega t}$ time dependence is assumed.

For two resonators, the Lagrangian can be written as

$$\begin{aligned}\mathcal{L} &= A_1\dot{Q}_1{}^2 + A_2\dot{Q}_2{}^2 + 2\alpha\sqrt{A_1A_2}\dot{Q}_1\dot{Q}_2 \\ &\quad -B_1Q_1^2 - B_2Q_2^2 - 2\beta\sqrt{B_1B_2}Q_1Q_2\end{aligned} \tag{A.4}$$

leading to two driven harmonic oscillator equations given by

$$A_1\ddot{Q}_1 + B_1Q_1 = -\alpha\sqrt{A_1A_2}\ddot{Q}_2 - \beta\sqrt{B_1B_2}Q_2 \tag{A.5}$$

$$A_2\ddot{Q}_2 + B_2Q_2 = -\alpha\sqrt{A_1A_2}\ddot{Q}_1 - \beta\sqrt{B_1B_2}Q_1 \tag{A.6}$$

implying that the resonant frequency shifting is driven by the interaction with the coupled resonator as expected. Note that under the assumption the resonators are identical, these equations reduce to those presented in [122]. Rearranging these equations, and assuming that $\omega_{0_1} = \sqrt{B_1/A_1}$ and $\omega_{0_2} = \sqrt{B_2/A_2}$, the resonant frequencies for the two resonant structures in the presence of coupling are given as

$$f_1 = \sqrt{\frac{f_{0_1}^2Q_1 + \beta_{12}Df_{0_1}f_{0_2}Q_2}{Q_1 + \alpha_{12}DQ_2}} \tag{A.7}$$

$$f_2 = \sqrt{\frac{f_{0_2}^2Q_2 + \left(f_{0_1}f_{0_2}/D\right)\beta_{21}Q_1}{Q_2 + \left(1/D\right)\alpha_{21}Q_1}} \tag{A.8}$$

where we let $D = \sqrt{A_2/A_1}$. The remaining unknown terms are the coupling parameters, α and β. To find these terms, the total energy is used as shown in [122] to give

$$\begin{aligned}E_{\mathcal{L}} &= A_1I_1^2 + A_2I_2^2 + 2\alpha\sqrt{A_1A_2}I_1I_2 \\ &\quad +B_1Q_1^2 + B_2Q_2^2 + 2\beta\sqrt{B_1B_2}Q_1Q_2\end{aligned} \tag{A.9}$$

and

$$\begin{aligned} E_1 &= W_{m,11} I_1^2 + W_{m,22} I_2^2 + 2W_{m,12} I_1 I_2 \\ &+ W_{e,11} Q_1^2 + W_{e,22} Q_2^2 + 2W_{e,12} Q_1 Q_2 \end{aligned} \tag{A.10}$$

where we let $E_{\mathcal{L}} = E_1$ to give α, β, and D as

$$\alpha_{12} = \frac{W_{m,12}}{W_{m,11} W_{m,22}} \tag{A.11}$$

$$\beta_{12} = \frac{W_{e,12}}{W_{e,11} W_{e,22}} \tag{A.12}$$

$$D = \sqrt{\frac{W_{m,22}}{W_{m,11}}} \tag{A.13}$$

Notice the subscripts of α and β in Equations A.11 and A.12. These correspond to the coupling scenario for each resonator. For instance, α_{12} and β_{12} are used to determine the shifted resonant frequency for resonator 1, f_1. If the two resonators are passive and resonant at the same frequency in isolation (identical resonators for instance), then $\alpha_{12} = \alpha_{21}$ and $\beta_{12} = \beta_{21}$.